# Statistical Analysis of Ice Microphysical Properties in Tropical Mesoscale Convective Systems Derived from Cloud Radar and In-Situ Microphysical Observations

Emmanuel Fontaine[1,6,7], Alfons Schwarzenboeck[1], Delphine Leroy[1], Julien Delanoë[2], Alain Protat[3], Fabien Dezitter[4], John Walter Strapp[5], Lyle Edward Lilie[5].

[1]Laboratoire de Météorologie Physique, UCA, CNRS, Aubière, France
[2]Laboratoire Atmosphère, Milieux et Observations Spatiales, UVSQ, Guyancourt, France
[3]Center for Australian Weather and Climate Research, Melbourne, Australia
[4]Airbus Helicopters, Toulouse, France
[5]Met Analytics, Toronto, Canada
[6]Department of Atmospheric Sciences, National Taiwan University, Taipei, Taiwan
[7]Now at CNRM, Université de Toulouse, Météo-France, CNRS, Lannion, France

*Correspondence to: E. Fontaine (emmanuel.r.j.fontaine@gmail.com)*

**Abstract.** This study presents a statistical analysis of the properties of ice hydrometeors in tropical mesoscale convective systems observed during four different aircraft campaigns. Among the instruments on board the aircraft, we focus on the synergy of a 94GHz cloud radar and 2 optical array probes (OAP; measuring hydrometeor sizes from 10µm to about 1cm). For two campaigns, an accurate simultaneous measurement of the ice water content is available, while for the two others, ice water content is retrieved from the synergy of the radar reflectivity measurements and hydrometeor size and morphological retrievals from OAP probes. The statistics of ice hydrometeor properties is calculated as a function of radar reflectivity factor measurement percentiles and temperature. Hence, mesoscale convective systems (MCS) microphysical properties (ice water content, visible extinction, mass-size relationship coefficients, total concentrations and second and third moment of hydrometeors size distribution) are sorted in temperature (thus altitude) zones, and subsequently each individual campaign is analysed with respect to median microphysical properties of the merged dataset (merging all 4 campaign datasets). The study demonstrates that ice water content (IWC), visible extinction, total crystal concentration, and second and third moments of hydrometeors size distributions are similar in all 4 type of MCS for IWC larger than 0.1g m$^{-3}$. Finally, two parameterizations are developed for deep convective systems. The first one concerns the calculation of the visible extinction as a function of temperature and ice water content. The second one concerns the calculation of hydrometeor size distributions as a function of ice water content and temperature that can be used in numerical weather prediction.

## 1 Introduction

Defining clouds and how they interact with the atmosphere is a major challenge in climate sciences and meteorology. Clouds play an important role in the evolution of the weather and climate on the Earth. They affect the dynamics and the thermodynamics of the troposphere, and impact the radiative transfer of energy in thermal and visible wavelengths by heating or cooling the atmosphere. In addition, clouds represent an important part of the hydrological cycle, due to evaporation and precipitation processes. Inversely, dynamic features such as the Madden Julian oscillation (MJO, perturbation of large scale circulation leading to an eastward propagation of organized convective activity) can also affect the development of deep convective clouds (Madden and Julian, 1994, 1971). Mesoscale Convective Systems (MCS) are complex clouds and are the result of specific synoptic conditions and mesoscale instabilities which lead to the development of cumulonimbus (Houze, 2004). The complexity of MCS is also relying on the dynamical, radiative, and precipitation characteristics which depend on the location in the evolving MCS (Houze, 2004). MCS can last several hours and can affect human societies in different ways.

Indeed, MCS are often associated with hazardous weather events such as landslides, flash floods, aircraft incidents, and tornadoes, all which can cause loss of human lives.

Weather and climate models use rather simplified schemes to describe the ice hydrometeors properties. Parametrization disagreements due to larger uncertainties in the representation of ice properties in clouds (Li et al., 2007, 2005) lead to large variations in the quantification of ice cloud effects on climate evolution (Intergovernmental Panel on Climate Change Fourth Assessment Report). An accurate estimation of the spatiotemporal distribution of the Ice Water Content (IWC) is a key parameter for evaluating and improving numerical weather prediction (Stephens et al., 2002). Underlying hydrometeor growth processes in MCS vary in time (growing, maturing, decaying phase) but also in space, in other words horizontally (distance from active convective zone) and vertically (as function of temperature).

A number of studies (Gayet et al., (2012); Lawson et al., (2010) and Stith et al., (2014)), demonstrate the presence of different type of ice hydrometeors in evolving MCS. In the active convective area, super cooled droplets larger than 500µm up to 3mm, were observed near -4°C and rimed ice hydrometeors about the same size below -11°C. Also at -47°C rimed particles about 2-3mm from updraft regions coexisting with ice crystals about 100µm (pristine ice) were encountered. Near the convective zone of MCS (i.e fresh anvil) presence of pristine ice (about 100µm), aggregates of hexagonal plates (about 500µm to 1mm) and capped columns (about 500µm) have been reported (Lawson et al., 2010). In aged anvils, columns (~100µm), plates (~100µm), and small aggregates (about 200µm) are observed near -43°C while large aggregates about 2mm and larger are found at lower altitudes (-36°C). Also in the cirrus part of MCS bullet-rosettes about 500µm and smaller (more common for in situ cirrus (Lawson et al., 2010)) and chain-like aggregates from 100µm up to about 1mm are found (aggregates of small rimed droplets caused by electric fields: Gayet et al., 2012; Stith et al., 2014).

With respect to ice particle density, Heymsfield et al., (2010) reported that ice particles seem to be denser near the convective part of MCS formed during the African Monsoon. Other studies have shown a variability of the mass-size relationship with temperature and related altitude (Fontaine et al., 2014; Schmitt and Heymsfield, 2010), which appears to be essentially linked to the variability of ice hydrometeor shapes related to different growth regimes (vapour diffusion, riming, aggregation).

Due to above mentioned spatiotemporal variations of MCS the different mean tendencies (hydrometeor concentration, ice water content, coefficients of mass-size relationship) reported in former studies can be partly linked to the chosen observation strategy of the MCS (i.e flight track in MCS) which of course is related to particular objectives of respective field projects (i.e. improvement of rain rate retrieval from satellite observations, icing condition at high altitude, comparison with ground radar observations, etc…).

Therefore the goal of this study is to investigate on the one hand the vertical variation of ice crystal properties in MCS (for example as a function of temperature) and on the other hand to study horizontal trends of ice microphysics at constant temperature levels. The latter will be accomplished by a composite analyses of microphysical properties and simultaneously measured radar reflectivity factor ($Z$). This study is focused on the ice microphysic in deep convective systems, also a preliminary investigations on the impact of vertical velocity has been performed asides. However, no significant tendencies were found to allow us to present our results as function of vertical velocity.

A frequency distribution of the profiles of the radar reflectivity factor throughout the MCS as a function of temperature allows to divide the microphysical in situ measurements into eight zones. For these height reflectivity zones microphysical properties are analysed and compared between the eight zones, but also intercompared between different locations and associated measurement campaigns where MCS were observed. Direct applications of this study are for example to improve retrievals of cloud properties from passive and active remote sensing observations and also parameterization of ice properties in weather and climate models for deep convective clouds. Moreover, it can help identifying zones in MCS where numerical weather predictions fails in representing ice microphysics.

Our statistical analysis is performed on cloud radar Doppler measurement and in-situ measurement. Cloud radar measurements include more than one million of data points of radar reflectivity factors and retrieved vertical velocities spanning from 170K to 273.15K (Temperature profiles from RASTA are calculated using re-analysis of ECMWF). And in-situ measurements include 55844 data points of 5 seconds duration in the temperature range from 215K to 273.15K. The following second section describes the utilized datasets and their derived parameters used in this study. The third section presents the analysis of radar reflectivity factors (Z) which provides the ranges of Z to perform the intercomparison between the four types of MCS. Moreover, for each range of Z a statistical analysis of vertical velocity is presented to bind the vertical dynamic of MCS and ice microphysical properties. The section 4 present the methodology of intercomparison used in this study. And section 5, present the inter-comparison of the microphysical parameters as function of Z and T. The end of this section is dedicated to present shortly the results of the investigations performed about the impact of vertical velocity. The sixth section, provide the parameterization of visible extinction and the parameterization of ice hydrometeors distributions. Then, last section adds the discussion and conclusion.

## 2 Data description

This study uses a dataset where MCS were observed in four different locations in the tropics and related to two different projects:

1. Megha-Tropiques in Niamey, during July and August 2010: observation of continental MCS formed over the region of Niamey (Niger) during the West African Monsoon (Drigeard et al., 2015; Fontaine et al., 2014; Roca et al., 2015). These MCS developed over the continent. 7665 points of 5 seconds.
2. Megha-Tropiques in Maldives, during November and December 2011: observation of oceanic MCS developed over the southern part of the Maldives and related to the ITCZ (Inter Tropical Convergence Zone) in the Indian Ocean. (Fontaine et al., 2014; Martini et al., 2015; Roca et al., 2015). It includes MCS developed during the wet phase of MJO and two events with isolated convective systems developed during the dry phase of MJO. 3347 points of 5 seconds.
3. HAIC-HIWC in Darwin, from January to March 2014: observations of MCS formed over Darwin and the North-East cost of Australia during the North Australian Monsoon (Leroy et al., 2016; Protat et al., 2016; Strapp et al. 2016; Leroy et al. 2017, Fontaine et al. 2017). During this campaigns, MCS developed over the land, the ocean, and near the cost. 23265 points of 5 seconds.
4. HAIC-HIWC in Cayenne during May 2015: observations of MCS developed over the French Guyana during the peak of its raining season (Yost et al., 2018). Same as for Darwin, MCS developed over the land, the ocean, and near the cost. 21567 points of 5 seconds.

Note that observations were essentially performed in mature MCS. All four measurement campaigns were conducted with the French research aircraft Falcon-20 operated by SAFIRE (Service des Avions Francais Instrumentés pour la Recherche en Environnement). On board the Falcon 20 were mounted two optical array probes (OAP): the 2D-S (2D stereographic probe; Lawson et al., 2006) and PIP (Precipitation Imaging Probe; Baumgardner et al., 2011), the cloud radar RASTA operating at 94GHz (Protat et al., 2016; Delanoë et al., 2014). In addition, bulk IWC measurements performed with the isokinetic evaporator probe (hereafter IKP-2 probe; Strapp et al. 2016; Davison et al. 2010) were available for the HAIC-HIWC flight campaigns (Darwin and Cayenne).

Both OAP probes record black and white images of hydrometeors with a resolution of 10µm and 100µm (2D-S and PIP, respectively). They are used to derived the size of hydrometeors ($D_{max}$ [cm] in this study), their projected surface (S [cm2]), their concentrations (or particle size distributions; hereafter PSD) as a function of their size ($N(D_{max})$ [$L^{-1}$ $\mu m^{-1}$]). The sizes of hydrometeors span from 10 µm to 1.28 cm with $D_{max}$ calculated as a function of the projected surface of hydrometeors (taking the maximum of radius passing through its barycentre; see Figure 1 in Leroy et al., 2016).

During both HAIC-HIWC campaigns, the IKP-2 probe was used to measure total condensed water, composed exclusively of ice water content (IWC [g m$^{-3}$]) and water vapour, then IWC were deduced using in-situ measurement of relative humidity. However, IWCs< 0.1g m-3 are not considered in this study, due to IKP-2 uncertainties particularly important for low IWC measurements (see Strapp et al. 2016a). For both Megha-Tropiques campaigns, IWC was retrieved using simulations of the reflectivity factor Z and images of OAP, thereby using the approximation of ice oblate spheroids (Fontaine et al., 2017; Fontaine et al., 2014). Results about accuracy of IWC retrieved from this latter method with regards to IKP-2 measurement are discussed in Fontaine et al., (2017).

The 94GHz RASTA radar measures *Z* and Doppler velocity *Vd* below and above the aircraft. RASTA has 6 antennas that allow measuring three non-collinear Doppler velocities, from which the 3 wind components (including the vertical air velocity) have been reconstructed (using the Protat and Zawadzki 1999 3D wind retrieval technique modified for the aircraft geometry). Detailed description of data processing is documented in Leroy et al. (2016 and 2017), Protat et al. (2016), Strapp et al. (2016b), and Davison et al. (2016). These references give a processing description for both datasets of the HAIC-HIWC project. But, Megha-Tropiques datasets (Fontaine et al. 2014) were reprocessed in order to undergo exactly the same version of processing tools for comparison reasons in this study.

Moreover, investigations have been performed to detect supercooled water using Rosemount icing detector (Baumgardner and Rodi 1989; Claffey et al. 1995; Cober et al. 2001) and Cloud Droplet Probe measurement. Few cases of super cooled water were detected and remove from the dataset (Leroy et al., 2016). Hence, the dataset used in this study is using exclusively data collected where only ice particles were measured. Also, retrieval of IWC for the Megha-Tropiques project were not performed in mixed phase conditions (more details in Fontaine et al., 2014 and 2017).

## 3 Radar observations

### 3.1 Radar reflectivity factors

In this section distributions of radar reflectivity factors *Z* from nadir and zenith profiles are investigated for the 4 datasets. Figure 1 shows percentiles of *Z* as a function of *T* measured with RASTA during the 4 airborne campaigns. The lines are colour coded as a function of the calculated percentiles. The percentiles of Z are calculated for a merged dataset that includes 11 flights for MT over Niamey, 11 flights for MT over Maldives, 19 flights for HAIC-HIWC over Darwin and 17 flights for HAIC-HIWC over Cayenne. Percentiles are not calculated as function of the number of profiles but by temperature ranges of 5K where only data with Z larger than -30dBZ are taken into account. Figure 1 shows that distributions of Z are not totally similar for all 4 airborne campaigns. MCS can extend over hundreds or thousands square kilometres, where size and distribution of their convective and stratiform areas can vary from one MCS to another. Hence, the same sampling strategy in two different MCS can provide two different statistics of ice microphysics properties as function of T, just as two different sampling strategy in the same MCS. The idea of this study is to compare the properties of ice hydrometeors for different tropical MCS locations, thereby rendering comparable different MCS systems (as a function of temperature), through the analysis of the frequency distribution of profiles of Z, dividing all MCS into eight zones. This strategy aims to reduce the impact of the different flight patterns and objectives for sampling MCS during each airborne campaigns used in this study.

Note that Z at 94 GHz is linked to the ice water content (Fontaine et al., 2014; Protat et al., 2016), but also to the size distribution of ice hydrometeors, respective crystal sizes, and mean diameter (Delanoë et al., 2014).

Our motivation to choose the limits of Z ranges on what the statistic of ice hydrometeors properties are calculated holds in two facts. First, Figure 1 shows that the variability of Z at a given T is large and this variability of Z vary along the altitude. We can observe in Figure 1 that Z extend from about -20dBZ to 18 dBZ at 260K while it spread out from -10dBZ to 10 dBZ at 200K. These latter facts have to be considered if we want to sort our dataset as function of T and Z. So the limit of the Z range cannot be the same for each altitude, as meeting ice hydrometeors linked to 15 dBZ or linked to -20dBZ at 200K is quiet impossible. The second fact holds on result on a former study. Indeed, Cetrone and Houze, (2009) used the profiling radar of TRMM satellite (Tropical Rainfall Measuring Mission; Huffman et al., 2007) to demonstrate with frequency distributions of radar reflectivity Z as a function of height that higher Z occur more often in convective echoes of MCS (in West African Monsoon, Maritime Continent and Bay of Bengal) than in their stratiform echoes. This former study was performed with the 13GHz radar profiler on board TRMM satellite, which is more sensitive to the precipitating particles (large drops and large ice crystals). The radar used in our study is more sensitive to smaller size of hydrometeors and linked to IWC (Protat et al., 2016), then it is more adapted to sort the properties of ice crystals presented in our study. Hence, this study presents ice microphysical properties in MCS as a function of temperature layers and also as a function of zones of reflectivity Z. In order to fix the limits of a limited number of Z levels, this study takes the percentiles of all merged campaigns datasets shown by the solid lines (all data) in Figure 1. This defines Z ranges as a function of height. Hereafter, these ranges will be called MCS reflectivity zones (MCSRZ) and numbered 1 to 8:

- MCS reflectivity zone 1: $Z < Z^{1th}$
- MCS reflectivity zone 2 : $Z \in [Z(T)^{1th} ; Z(T)^{10th}[$
- MCS reflectivity zone 3 : $Z \in [Z(T)^{10th} ; Z(T)^{30th}[$
- MCS reflectivity zone 4 : $Z \in [Z(T)^{30th} ; Z(T)^{50th}[$
- MCS reflectivity zone 5 : $Z \in [Z(T)^{50th} ; Z(T)^{70th}[$
- MCS reflectivity zone 6 : $Z \in [Z(T)^{70th} ; Z(T)^{90th}[$
- MCS reflectivity zone 7 : $Z \in [Z(T)^{90th} ; Z(T)^{99th}[$
- MCS reflectivity zone 8 : $Z \geq Z(T)^{99th}$

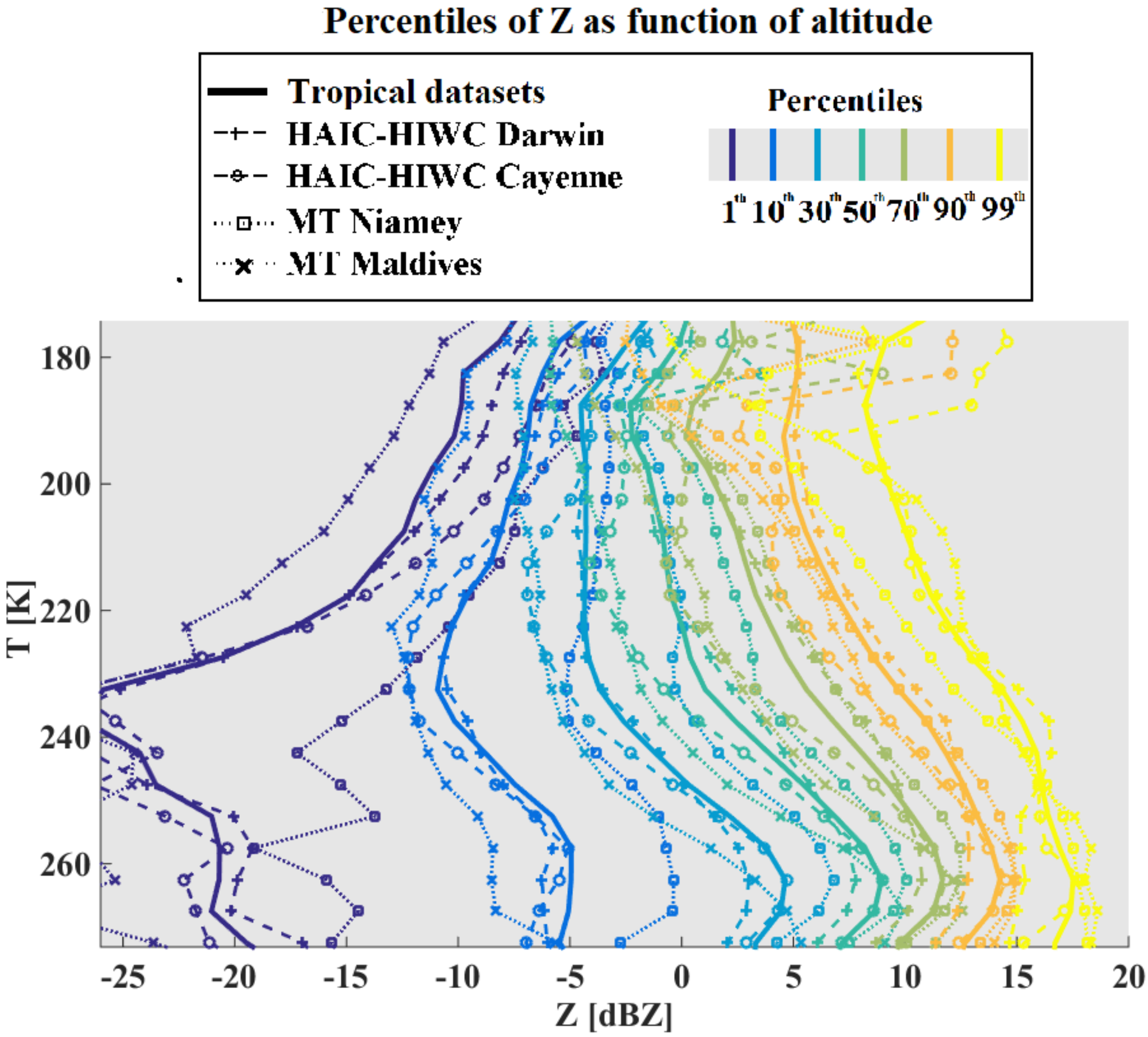

**Figure 1: Percentiles of radar reflectivity factors in dBZ on *x*-axis, as a function of temperature on *y*-axis.**

Figure 2 shows an example of the method to store data as a function of *T* and MCS reflectivity zones. In Figure 2(a), we can see original processed *Z* profiles for the flight 13 of HAIC-HIWC of the Darwin experiment. In Figure 2(b), eight colours representing the above defined MCS reflectivity zones. This method is applied for all datasets thereby using all radar reflectivity profiles (*Z* from Nadir and Zenith direction).

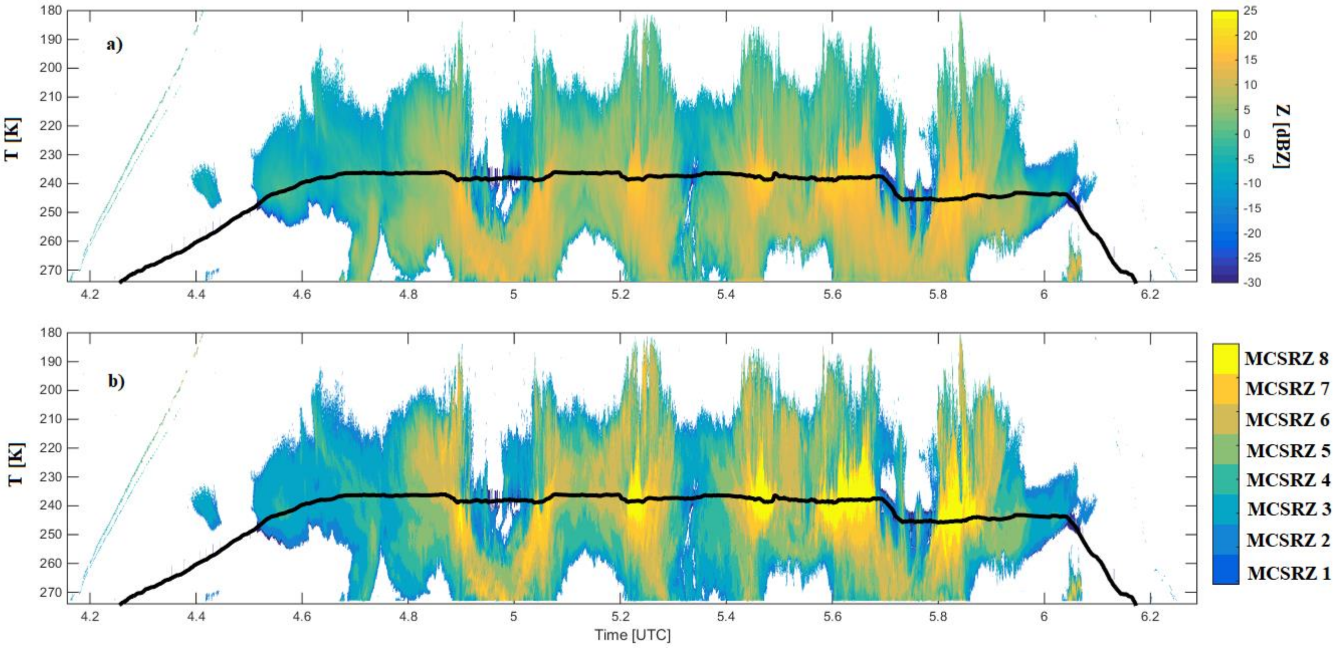

**Figure 2: a) Time series of cloud radar profiles of flight 13 of HAI-HIWC over Darwin. Z color coded in dBZ and plotted as a function of the temperature (y-axis). b) Similar to a) with Z classified according to altitude dependent Z percentile ranges.**

### 3.2 Retrieved vertical velocity in MCS reflectivity zones

This section investigates links between retrieved vertical velocity from Doppler measurement and MCS reflectivity zones. We assume that Vz ($V_d$) = $w_{ret}$ + Vt, where Vt is the terminal velocity of hydrometeors (Delanoë et al., 2007, 2014) and $w_{ret}$ the vertical wind speed. In a first order, our study investigates variability of bulk microphysical properties of the icy part of MCS as function of temperature range and Z range (i.e. MCS reflectivity zones). As it is noted in the introduction no clear tendencies have been found between variability of ice microphysical parameters presented in our study and vertical velocities. Then, we investigate the probability to observe significant vertical movement in each range of Z (or MCS reflectivity zones). In other words, we investigate if there is any relationship between MCS reflectivity zones and vertical dynamic of MCS. We assume that convective part of MCS are associated with pronounced updraft and downdraft and that stratiform part of MCS have non-pronounced vertical velocity ($w \approx 0$ m $s^{-1}$) (see Figure 16 from Houze 2004).

Figure 3 shows median updraft ($w_{ret}>0$ m $s^{-1}$) and downdraft ($w_{ret}<0$ m $s^{-1}$) in each MCS reflectivity zones (MCSRZ 2 to MCSRZ 8 from the top line to the bottom line respectively) and for each airborne campaign (Cayenne, Darwin, Maldives Island and Niamey, from left column to right column respectively). Black lines represent median updraft and downdraft for each respective airborne campaigns, while grey lines are median (solid line), 25th and 75th percentiles (dashed lines) and 10th and 90th percentiles (dotted lines) for the merged dataset. Black lines and grey lines are calculated using RASTA vertical profiles. The red stars are median downdraft and updraft when we use only vertical velocity measured by the aircraft (w; in-situ measurement).

We can observe a symmetry between updraft and downdraft in all MCS reflectivity zones for each campaigns, meaning that at a given altitude, absolute magnitude of downdraft is about the magnitude of updraft for median, 25th, 75th,10th and 90th calculated percentiles. For RASTA measurement, we can see that median updraft ($w_{ret}>0m.s^{-1}$) and median downdraft ($w_{ret}<0$ m $s^{-1}$) for each airborne campaigns agree well with median updraft and downdraft for the merged dataset in all MCS reflectivity zones. Except for Maldives observations where median $w_{ret}$ are smaller for T < 255K. Also, median in-situ w tend to be a bit smaller than median $w_{ret}$, except for updraft in Maldives above the bright band; $w \approx 2.5$ m $s^{-1}$ versus $w_{ret} \approx 1$ m $s^{-1}$.

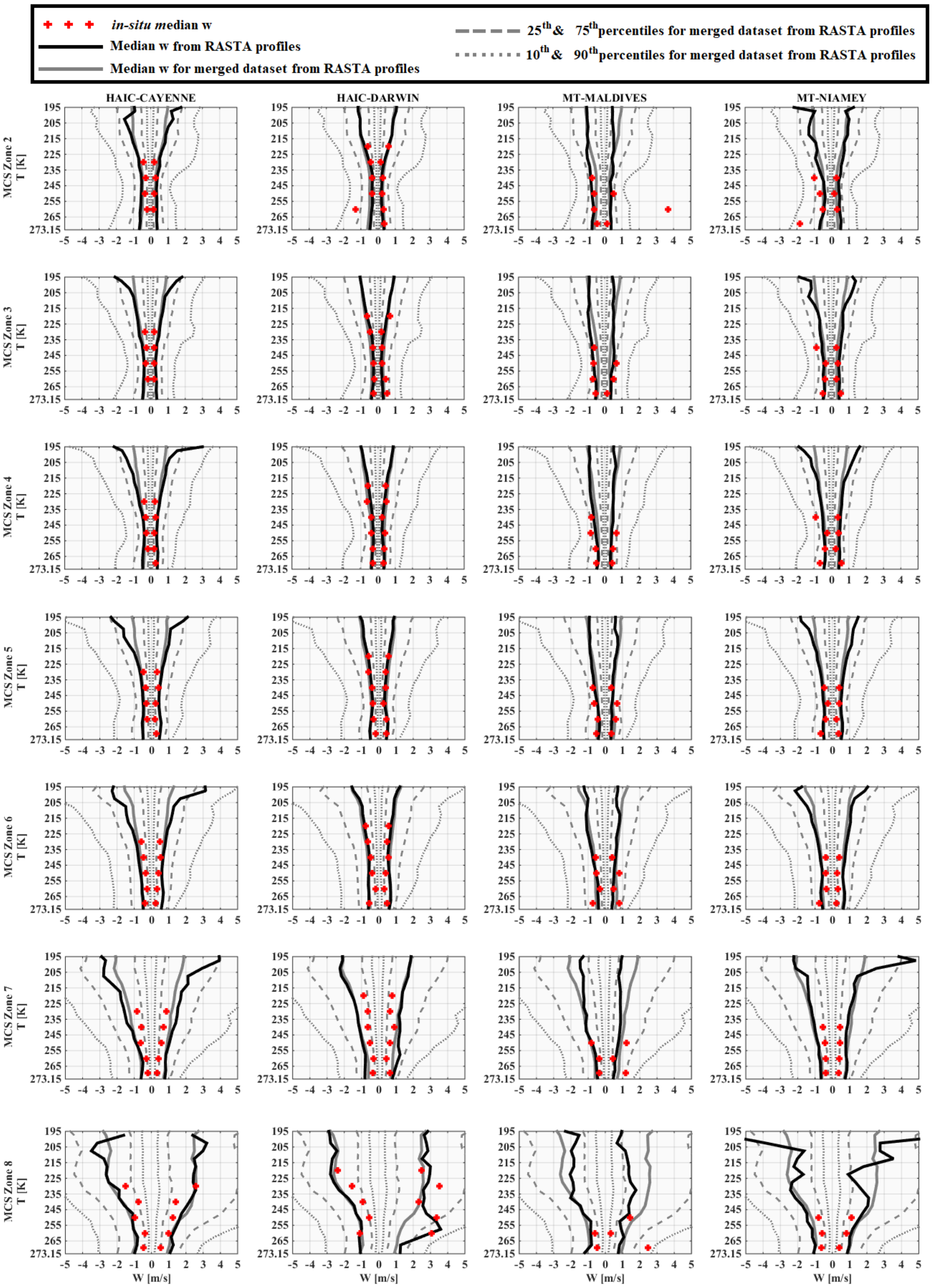

**Figure 3: from the top line to the bottom line vertical velocities for MCS reflectivity zone 2 to MCS reflectivity zone 8.**

In general magnitude of updraft and downdraft increase with altitude and MCS reflectivity zones, where magnitudes of vertical velocity (negative and positive) are highest for MCS reflectivity zones 8. For all 4 datasets vertical wind speeds of MCS reflectivity zones 2-6 are smaller than or about 1 m $s^{-1}$.

To complete our investigation between MCS reflectivity zones and vertical velocity, we study the probability to observe vertical movement. We use a threshold for vertical velocity to distinguish between discernible vertical movement and nearly not. We take roughly a value of 1m.$s^{-1}$ to be the threshold to detect vertical movement (Houze 2004), such -1 m $s^{-1}$ < w < 1 m

$s^{-1}$ there is no noticeable vertical movement neither upward nor downward. The decision of taking a threshold of 1m $s^{-1}$ for updraft and downdraft, is motivated by the fact that we have to take into account the measurement uncertainty (less than 0.25-0.5 m $s^{-1}$). Moreover, knowing that variance of vertical turbulences is about 1.5 $m^2$ $s^{-2}$ (Large Eddy Simulations at 50 m resolution; Verrelle et al., 2017; Strauss et al., 2019). The fact that median $w_{ret}$ for the merged dataset in MCS reflectivity zones 2 to 6 are smaller than 1m.$s^{-1}$ consolidate our decision to take a threshold of 1m.$s^{-1}$.

Then, knowing T and Z, a probability to observe | wret | ≥ 1m $s^{-1}$ is calculated as a function of MCS reflectivity zones and temperature, both for in-situ measurement and cloud radar measurement. Colored solid lines in Figure 4 are probabilities calculated from RASTA measurement and dashed lines with stars are probabilities calculated with vertical velocity measured at the aircraft level (in-situ measurement). Both type of probabilities are different in each MCS zones and probabilities made with in-situ measurement are smaller than these calculated with RASTA retrievals; except in MCS reflectivity zones 8 in Darwin where they are similar. Hence, in the point of view of observations of vertical velocity, statistic are different between in-situ measurement and RASTA retrievals: different probabilities to observe vertical velocity with magnitude larger than 1m.$s^{-1}$ (updraft and downdraft) for the same range of Z and range of T.

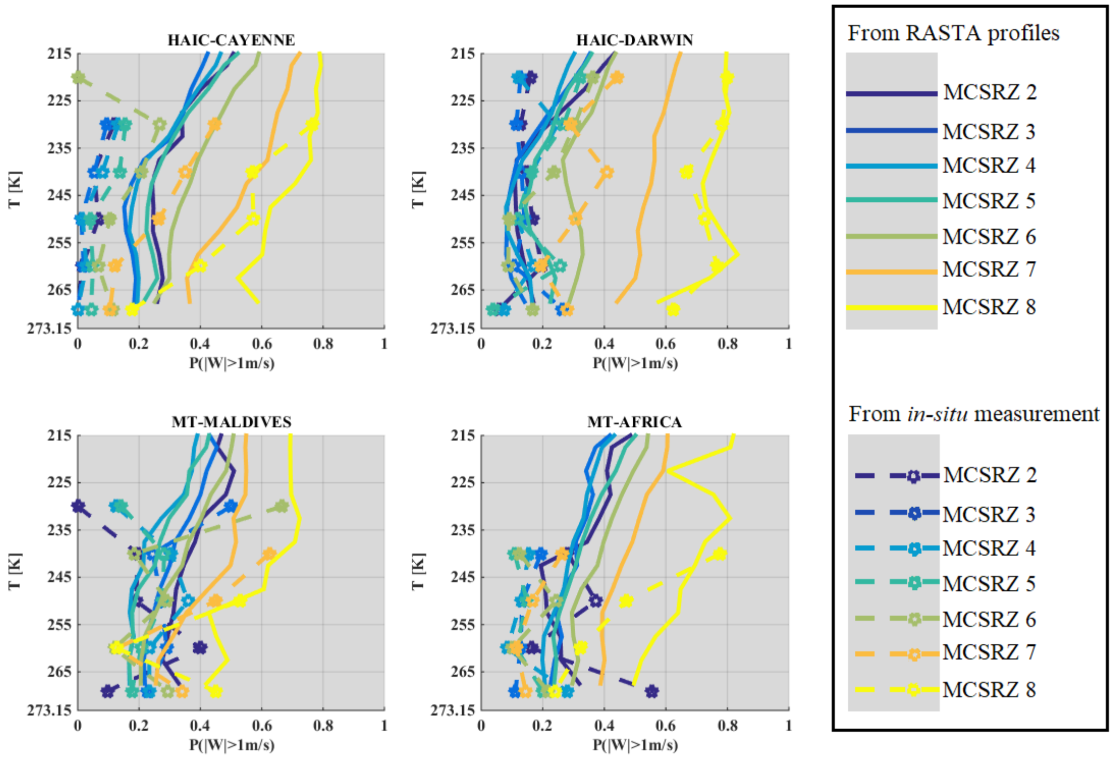

**Figure 4: Probability to observe vertical velocity with absolute magnitude larger than 1m.$s^{-1}$ in each MCS reflectivity zone (MCSRZ; color scale) for measurement from the radar Doppler RASTA in solid lines and in dashed lines with stars marker for in-situ measurement.**

In Figure 4 we show that probabilities to observe | $w_{ret}$ | ≥ 1m $s^{-1}$ are highest for MCS reflectivity zones 8 then 7 and 6, meaning that these MCS reflectivity zones tend to be more impacted by vertical movement (convective areas of MCS), than it is the case for other MCS reflectivity zones. Also, these probabilities generally increase with altitude for all airborne campaigns. Which meet the conclusions from Figure 3. Generally, in MCS reflectivity zones 5, 4, 3, and 2, the probabilities P(|$w_{ret}$ ≥1 m $s^{-1}$) as a function of T are close to each other with a decreasing trend as reflectivity decreases, except for the Maldives campaign. Statistically, MCS reflectivity zones 7 and 8 represent for all 4 datasets the most convective part of our observations in MCS. Contrariwise the lower MCS reflectivity zones 2 to 5 represent the stratiform part of MCS with significantly lower vertical wind speeds.

## 4 Method of intercomparison

This study compares and discusses a series of ice cloud properties, such as IWC, visible extinction, *α* and *ß* coefficients of the dynamically retrieved m(D) power law, size of largest ice crystal of PSD, crystal number concentrations $N_T$, PSD 2nd and 3rd moments ($M_2$ and $M_3$, respectively), and the ratio of IWC/$M_2$. The above mentioned ice hydrometeor properties in all 4 MCS locations will be investigated as a function of *T* and MCS reflectivity zones (range of *Z* given by percentiles of *Z* as a function of *T*) which have been introduced in section 3. In the subsequent section 5 a series of figures presenting results for above mentioned ice cloud properties (parameter *X*) will be presented in a uniform format. In all these Figures (5, 7, 9, 11, 13, 15, 17, 21, 23, 25) we show the median values of *X*, averaging MCS data from the 4 merged dataset (with 25th and 75th percentiles represented by whiskers), as a function of T and MCS reflectivity zones (colored lines). The grey band shows 25th and 75th percentiles of the parameter for the entire merged dataset thereby merging data from all MCS reflectivity zones. 25th, median, and 75th percentiles of all parameters in each MCS reflectivity zones presented in the figures for the merged dataset are given in Annexe C, in order to allow comparison with other datasets and evaluation of numerical weather prediction. If the range of variability of this median of parameter *X* in MCS reflectivity zone ***i*** defined by its 25th and 75th percentiles, does not overlap with corresponding ranges of variability of *X* defined by the 25th and 75th percentiles of MCS reflectivity zones ***i***-1 and ***i***+1, respectively, this makes the median (4 tropical campaigns) of *X* a candidate for *X* parametrization as a function of MCS reflectivity zone and T.

Then, in all the Figures 6, 8, 10, 12, 14, 16, 18, 22, 24 and 26 we calculate the median relative difference in percent (hereafter MRD-*X*) for all 4 individual MCS datasets (Cayenne (a), Darwin (b) , Maldives (c), and Niamey (d)) with respect to the median of *X* as a function of MCS reflectivity zone and *T*. In order to take into account the uncertainties in all type of measurements (hereafter noted U(X)/X), uncertainties (represented by grey bands) for each parameter X were taken from Baumgardner et al. (2017). So, when the MRD-*X* is larger than *U(X)/X*, it means that there is a significant difference between the median of the studied parameter for the merged dataset and the respective *X* of the selected individual MCS dataset. For the case that MRD-*X* is smaller than or equal to *U(X)/X*, the median of *X* of the merged dataset, under the condition that the median (4 tropical campaigns) of *X* is distinguishable between neighboring MCS reflectivity zones, can be used for the respective type of MCS. Hence, if the latter case is true for all 4 MCS locations, then the median (4 tropical campaigns) of *X* is suitable to represent all 4 types (=location) of observed MCS.

Note that in all figures (Figures 5-26) temperature of in-situ observations will be on the y axis, while MCS reflectivity zones are color coded.

The comparison of ice hydrometeors' properties of the 4 MCS locations investigated in this study, will mainly focus on the question, if MRD-*X* (for individual MCS reflectivity zones) is larger or smaller than *U(X)/X*, also depending on MCS locations. For each parameters presented in this study, either for the merged dataset or the campaigns individually (for calculation of MRD-X), the calculation are performed with the same conditions. The samples in each conditions (T range and MCS reflectivity zones) have the same size for all parameters. Indeed, data are selected if they meet the temperature and radar reflectivity criteria, but also the total concentration has to be positive (for $D_{max}$ >50µm); mixed phased conditions being excluded. So, the size of the samples is equal (i.e. number of data points in each ranges of T and of Z) for IWC, visible extinction, *α* and *ß* coefficients of m(D) power law, largest particle of PSDs, crystal number concentrations *NT*, PSD 2nd and 3rd moments ($M_2$ and $M_3$, respectively), and the ratio of IWC/$M_2$.

## 5 In-situ Observations in tropical MCS: HAIC-HIWC and Megha-Tropiques projects

### 5.1 Ice water content

This section discusses the IWC measured during HAIC-HIWC project and the IWC retrieved for the Megha-Tropiques project. IWC from the four data sets were merged to calculate the main statistic (merged dataset). Figure 5 shows median IWC for the merged dataset as a function of T and as function of MCS reflectivity zones (color coded lines). Solely, the graphical representation is limited to medians of IWC for MCS reflectivity zones 4 to 8. Because, IWC in MCS reflectivity zones 2 and 3 are linked to IWC smaller than 0.1 g m$^{-3}$, where IWC data are subject to less confidence. In total, 30% of the data observed in 4 tropical data sets have an IWC lower than 0.1g m$^{-3}$ because the lower limit of MCS reflectivity zone 4 is defined with the 30th percentiles of Z. The figure reveals an IWC increases with increasing MCS reflectivity zone for a given range of temperature. IWC median values differ clearly as a function of the MCS reflectivity zone, and this for the entire range of temperatures, with only a few exceptions above the freezing level (T $\in$ [265 K; 273 K[), between MCS reflectivity zones 4 and 5, and MCS reflectivity zones 7 and 8, respectively, with small overlap in IWC ranges. In MCS reflectivity zones 4 to 7, median IWC increase with increasing T between 215 K and 260 K (where IWC has its maximum) and then slightly decrease as T further increases towards 273K. In MCS reflectivity zone 8 IWC behaves rather similar with a maximum IWC already reached at 250 K.

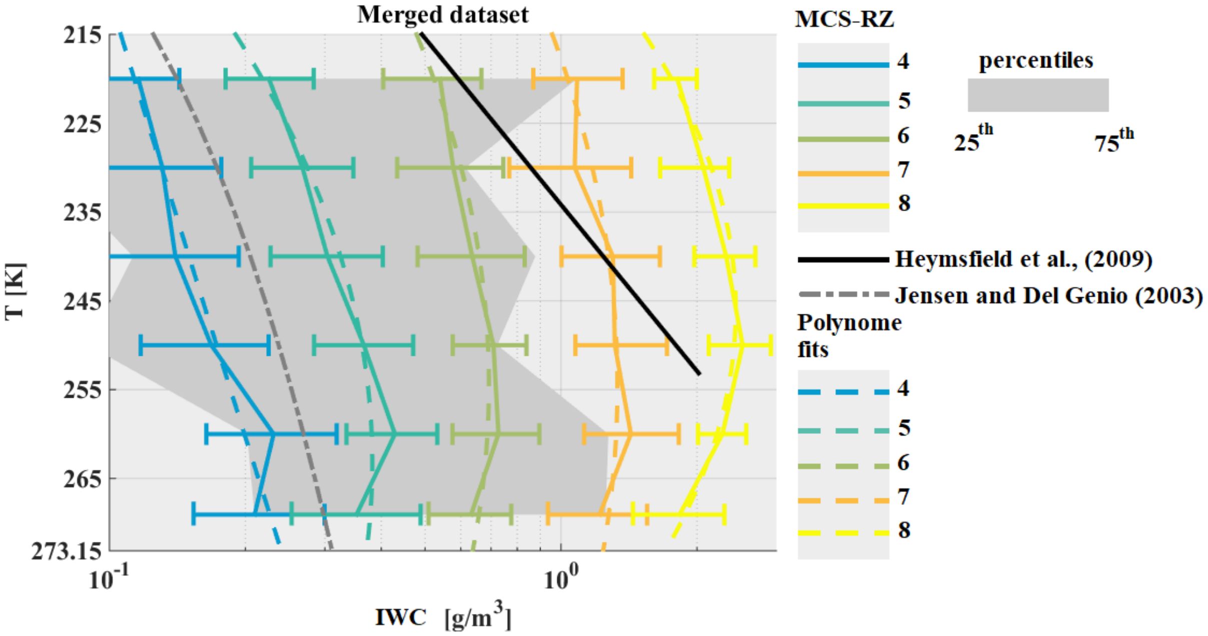

**Figure 5: Median of IWC in [g.m$^{-3}$] on x-axis, as a function of temperature in [K] on y-axis for different MCS reflectivity zones. Results for the merged dataset include both MT and both HAIC-HIWC datasets. The grey band represents 25th and 75th percentiles of merged dataset. Extremity of error bar show 25th and 75th percentiles of IWC in each MCS-RZ.**

Figure 6 shows MRD-IWC for the four different campaigns. It is necessary that we recall that median IWC as function of T and MCS reflectivity zones are calculated using a merged dataset where there are IWC from direct measurement and retrieved IWC from Z and PSD (Fontaine et al., 2017). Then, there is two different uncertainties to consider to evaluate the MRD-IWC in each campaigns. Firstly, for Darwin and Cayenne campaigns the IWC were measured with IKP-2 probe (direct measurement) with an uncertainty on measured IWC increasing with temperature (~5% at 220K and ~20% at 273.15 K; Strapp et al., 2016). Secondly, for Niamey and Maldives IWC were retrieved using the method described by Fontaine et al., (2017) (indirect measurement) with an uncertainty with regards to the IKP estimated by about ±32%. Hence, in Figure 6-a) and Figure 6-b) the grey bands area show the uncertainty of the IKP-2 probe that was used for Cayenne and Darwin campaigns. While in Figure 6-c) and Figure 6-d) the grey bands area describe the uncertainty on the retrieval method for IWC that was used for datasets of Niamey and Maldives.

Note that confidence in direct bulk IWC measurements from the IKP-2 is significantly higher than in indirect IWC calculations from the retrieval method (Fontaine et al., 2017).

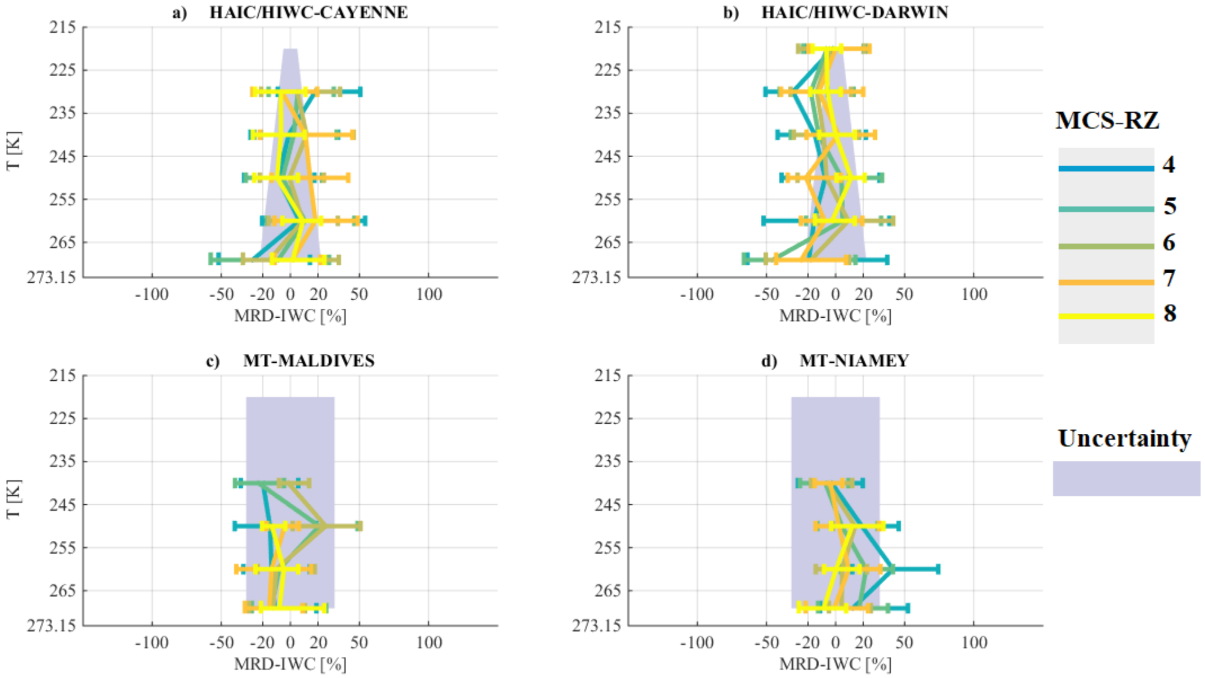

**Figure 6: Median relative difference (MRD) of IWC during a) HAIC-HIWC in Cayenne, b) HAIC-HIWC in Darwin, c) Megha-Tropiques Maldives Islands and d) Megha-Tropiques in Niamey, with respect to median of IWC for the merged dataset on x-axis as a function of temperature in [K] on y-axis. The grey bands represent the uncertainties of the IWC measurement in b) and c), and the median deviation between measurement and the IWC retrieval method (Fontaine et al. 2017) in d) and e). Lines are color coded as a function of the MCS reflectivity zones where in-situ measurement were performed, dashed color coded lines represent the polynomial fit. Extremity of error bar show 25th and 75th percentiles of IWC relative error in each MCS reflectivity zone.**

Then, Figure 6(a), (b), (c), and (d) show MRD-IWC for all MCS reflectivity zones as a function of T. For all 4 tropical MCS, MRD-IWC in MCS reflectivity zones 4 to 8 are distributed around 0 and are in general less than 30-40% (25th to 75th percentiles). Measured IWC in MCS reflectivity zone 8 are in good agreement with the median IWC for all 4 tropical datasets. Uncertainty U(IWC)/IWC for IKP-2 measurements (Darwin and Cayenne) especially at high altitude (about 5%) is smaller than the expected deviation MRD-IWC. For mid and lower altitudes, MRD-IWC for Darwin and Cayenne particularly for zones 5 and 8 are of the order of corresponding U(IWC)/IWC. Concerning, MCS over Niamey and the Maldives Island, MRD-IWC (25th to 75th percentiles) in general do not exceed corresponding U(IWC)/IWC.

For comparison purposes with former studies, two IWC-T relationships from literature are added in Figure 5. Jensen and Del Genio (2003) suggested an IWC-T relationship in order to account for the limited sensitivity of the precipitation radar aboard the TRMM satellite, not allowing for small ice crystals at the top of convective clouds' anvils to be observed. They used radar reflectivity factors of a 35GHz radar based on Manus Island (North-East of Australia; 2.058°S, 147.425°E), thereby calculating IWC from an IWC-Z relationship ($IWC=0.5*(0.5.Z^{0.36})$; Jensen et al., 2002). The resulting IWC-T relationship given by Jensen and Del Genio (2003) is reported by a dashed-dotted grey line, which fits between 75th percentiles of merged median IWC of MCS reflectivity zone 4 and 25th percentile of MCS reflectivity zones 5. We recall that IWC, as a function of T, in MCS reflectivity zones 4 and 5 are related to Z between 30th-50th and 50th-70th percentiles, respectively. Hence, IWC-T relationship from Jensen and Del Genio (2003) is more adapted to stratiform part of MCS where convective movement occurs less often.

Moreover, Heymsfield et al., (2009) established an IWC-T relationship based on 7 fields campaigns (black line in Figure 5). They focused their study on maritime updrafts in tropical atmosphere for a temperature range $T \in [213.15K; 253.15K]$. Their suggested IWC tend to be in the range of IWC of MCS reflectivity zones 6- 8 with IWC increasing with T. We already showed in section 3.2 that MCS reflectivity zones 7 and 8 have higher probabilities to be convective (updraft regions with higher magnitudes of vertical velocity), as compared to other MCS reflectivity zones. Therefore, Heymsfield et al., (2009) IWC parametrizations for maritime updrafts are not inconsistent with data from this study.

Overall, this section demonstrates that variation of IWC with the temperature is similar in all type of MCSs for corresponding ranges of radar reflectivity factors. Hence, we assume that IWC-Z-T relationships developed in Protat et al., (2016) is valid for all types of MCS in the Tropics, at least for IWC larger than 0.1 g m$^{-3}$.

### 5.2 Visible extinction

Figure 7 shows visible extinction coefficients (σ) calculated from OAP 2D images (approximation of large particles; Van de Hulst, 1981) where S(Dmax) is the projected area recorded by OAP and $\Delta D_{max}$ is the bin resolution equal to 10µm:

$$\sigma = 2 \cdot \sum_{15\mu m}^{12845\mu m} N(D_{max}) \cdot S(D_{max}) \cdot \Delta D_{max} \qquad [m^{-1}] \tag{1}$$

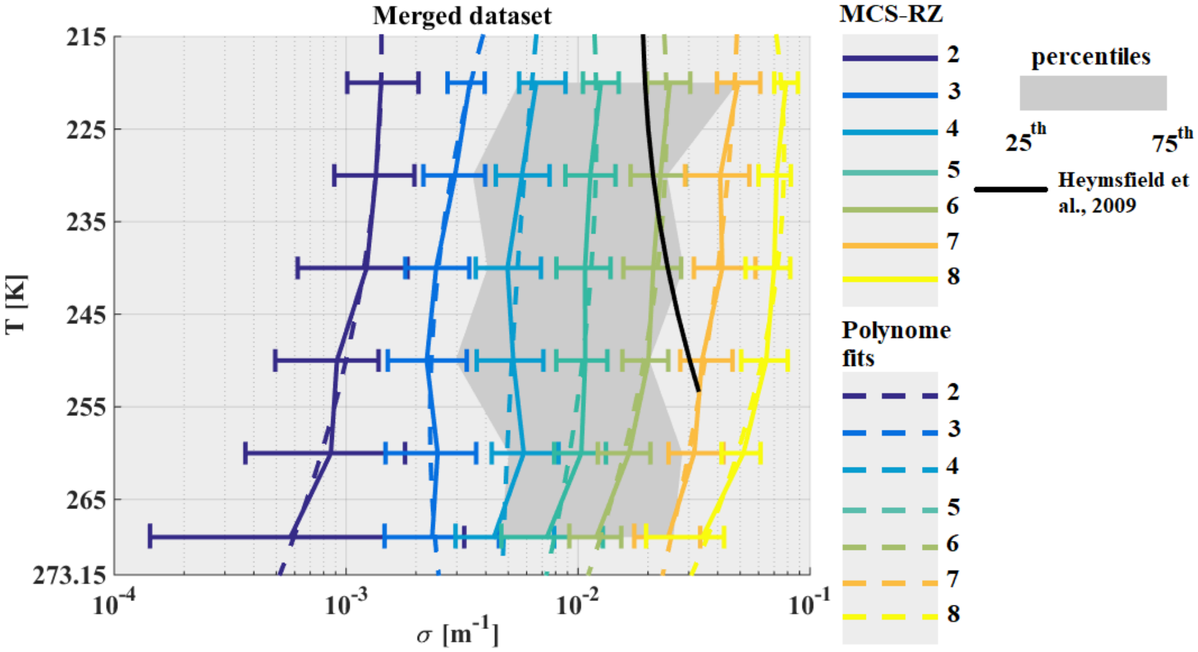

**Figure 7: Same as Figure 5 but for visible extinction σ given on x-axis in m$^{-1}$.**

In Figure 7, median σ for the merged dataset (4 tropical campaigns) increase with MCS reflectivity zone as expected, and also increase with altitude (decrease with T), with larger gradients for T ∊ [245; 273.15] than for T ∊ [215K; 245K] in MCS reflectivity zones 5 to 8.

The uncertainty (U(σ)/σ) (grey band in Figure 8(a) to Figure 8(d) is calculated as follows:

$$\frac{U(\sigma)}{\sigma} = \sqrt{2 \cdot \frac{U(D)}{D}^2 + \frac{U(N)}{N}^2} = \pm 57\% \tag{2}$$

With $\frac{U(D)}{D} = \pm 20\%$, taking into account the uncertainty in the calculation of the size of hydrometeors and $\frac{U(N)}{N} = \pm 50\%$ for the uncertainty on the calculation of the concentration of hydrometeors from optical array probes (Baumgardner et al., 2017). Above uncertainties are those for particles larger than 100 µm. Note, that if we took uncertainties for particles smaller than 100µm (with (U(D))/D=±50% and (U(N))/N=±100%) the uncertainty on the calculation of σ would increase to ± 122%. The reason why we do not take into account uncertainty of smaller particle is due to that these particles contribute little to the visible extinction (2% in the range [235K; 273.15] and 10% in the range [215K; 225K].

For all 4 types of tropical MCS, MRD-σ shown in Figure 8(a), 8(b), 8(c), and Figure 8(d) are in general smaller or equal to $\pm\frac{U(\sigma)}{\sigma}$. Hence, visible extinction in tropical MCS tend to be similar for all types of MCS observed in the same range of T and MCS reflectivity zone.

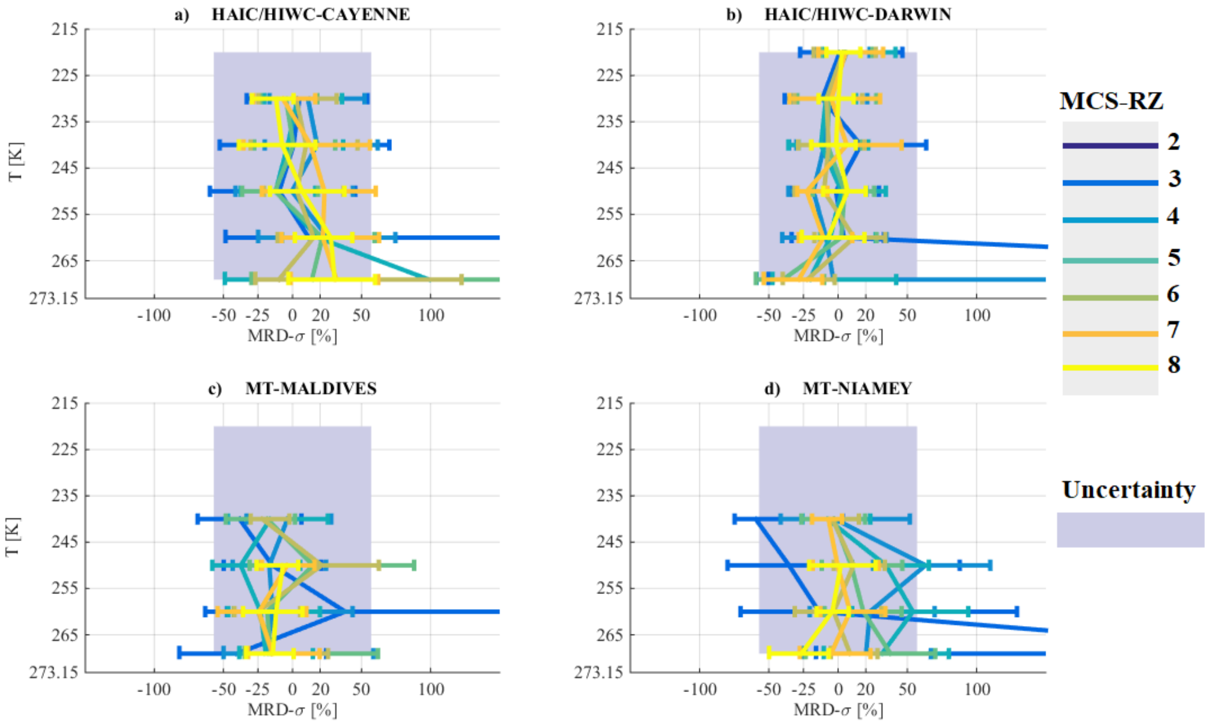

**Figure 8: Same as Figure 6 but for visible extinction MRD-σ.**

Furthermore, a σ–T relationship from Heymsfield et al. (2009) (black line) is added in Figure 7, which is calculated, as a function of T, as the sum of the total area of particles larger than 50µm plus the total area of particles smaller than 50µm times a factor of 2 in order to satisfy Eq. (1) and to compare with results of this study. We conclude that σ–T estimation presented in Heymsfield et al. (2009) for maritime convective clouds is rather comparable to median σ calculations (merged dataset) in MCS reflectivity zones 6 to 7 corresponding to higher reflectivity zones, and thus statistically to zones with some remaining convective strength.

### 5.3 Concentration of ice hydrometeors

Subsequently are presented observed total concentrations for the merged datasets integrating particle sizes beyond 50µm ($N_T(D_{max} > 50\mu m)$; hereafter $N_{T,50}$):

$$N_T(D_{max} > 50\mu m) = \sum_{Dmax=50}^{Dmax=12845} N(D_{max}) \cdot \Delta D_{max} \qquad [L^{-1}] \tag{3}$$

Median of $N_{T,50}$ as a function of T and MCS reflectivity zones are shown in Figure 9 as well as MRD-$N_{T,50}$ for the 4 tropical MCS locations in Figure 10 (a), 10(b), 10(c), and 10(d). We observe an increase of median $N_{T,50}$ with altitude for all MCS reflectivity zones. Also $N_{T,50}$ increases with MCS reflectivity zones for a given T, with highest $N_{T,50}$ in MCS reflectivity zone 8. The range of variability for $N_{T,50}$ reveals significant overlap of 25th and 75th percentiles of neighboring MCS reflectivity zones.

Figure 10 show MRD-$NT_{50}$ where measurement uncertainty on concentrations are assumed ±100% (Baumgardner et al., 2017). MRD- $N_{T,50}$ in 4 different tropical MCS locations, particularly for higher MCS reflectivity zones are of the order and even larger (75th percentile MRD-$N_{T,50}$) than the measurement uncertainty. Even if the limit of concentrations of ice hydrometeors are not well defined between neighboring MCS reflectivity zones (Figure 9). These concentrations tend to be similar for a given range of T and Z for the four different MCS locations.

A similar investigation is performed for total concentrations integrating beyond 15 µm (NT). Since major conclusion are similar to those given for $NT_{50}$, figures for $N_T$ are shown in Appendices A. Overall, median of $N_{T,50}$ for the merged dataset are smaller by about one order of magnitude with respect to the median of $N_T$ for the same MCS reflectivity zone. And $N_T$ over

Maldives tend to be larger than median $N_T$ for the merged dataset. It shows that for a given range of T and Z, we can observe very different concentrations of very small particles (about 15µm to 50µm) over the 4 different MCS locations (especially for Maldives: oceanic MCS) with a factor of 10 even larger. But when looking total concentrations beyond 50µm, the differences between the 4 locations mitigate, in order that for the 4 locations MRD-$NT_{50}$ are about to be similar or smaller than measurement uncertainty of ice hydrometeors concentrations.

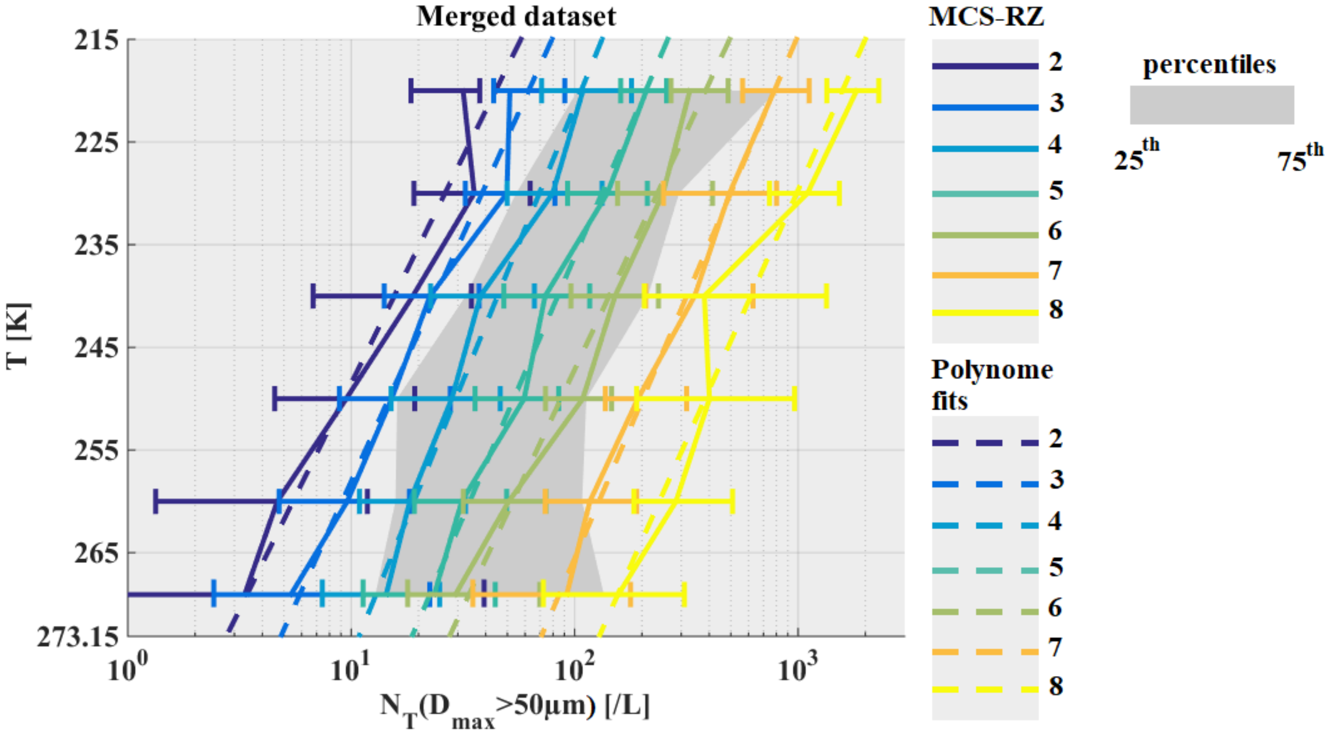

**Figure 9: Same as Figure 5, but for total concentrations integrated beyond $D_{max}$=50µm in [$L^{-1}$].**

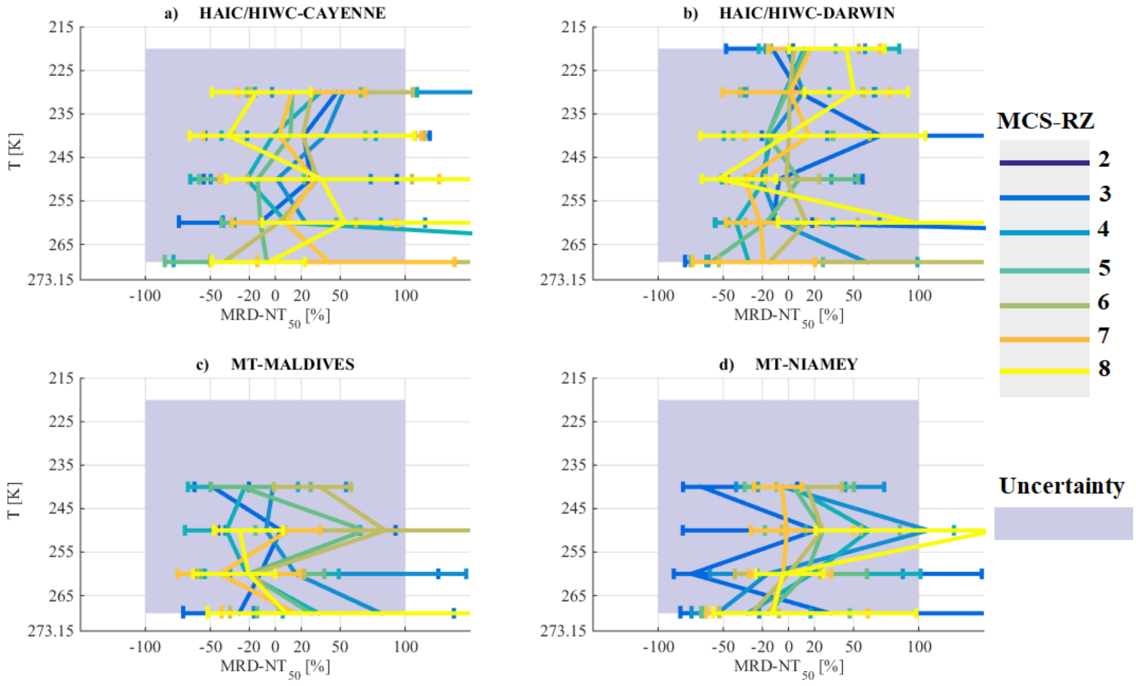

**Figure 10: Same as Figure 6, but for MRD-$NT_{50}$.**

Concerning concentration of larger hydrometeors, Figure 11 shows concentrations of hydrometeors when PSD are integrated beyond 500µm (hereafter $N_{T,500}$; eq. (4)), where the uncertainty on their measurement is estimated as about ±50% for hydrometeors larger than 100µm (Baumgardner et al., 2017).

$$N_T(D_{max} > 500\mu m) = \sum_{Dmax=505}^{Dmax=12845} N(D_{max}) \cdot \Delta D_{max} \qquad [L^{-1}] \tag{4}$$

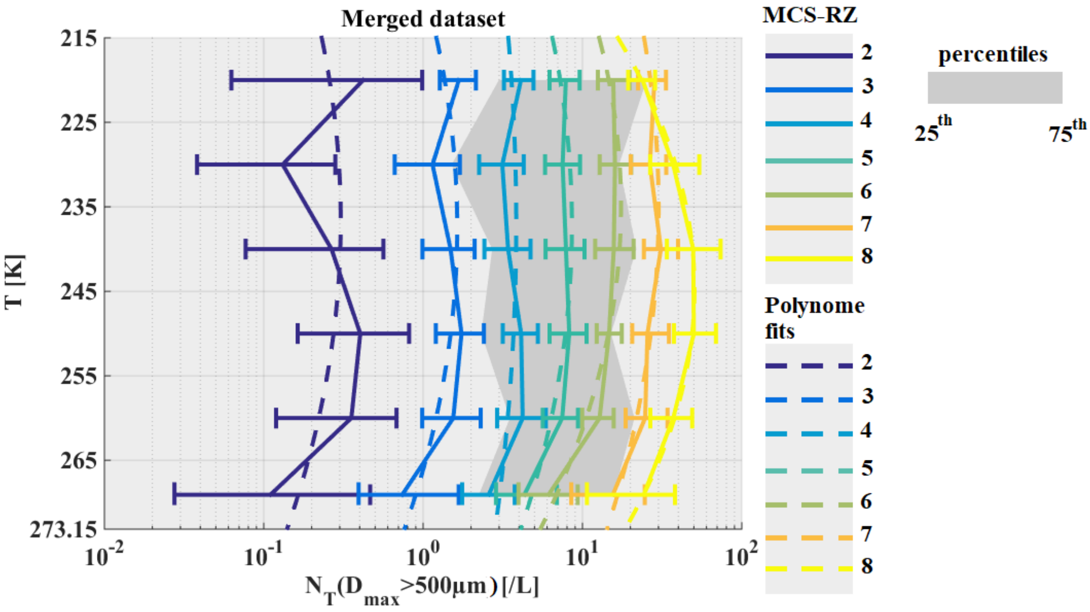

**Figure 11: Same as Figure 5, but for concentrations of hydrometeors integrated beyond $D_{max}$ =500µm in [$L^{-1}$].**

In Figure 11 median $N_{T,500}$ are presented as a function of T and MCS reflectivity zone. The curves of median $N_{T,500}$ are different from curves of median $N_T$ and $N_{T,50}$. Indeed, particularly for higher MCS reflectivity zones and in lower altitude levels (T ∊ [250K; 273.15K]), $N_{T,500}$ tends to increase with altitude, reaches a maximum value around T ∊ [235K; 250K], and then rather decreases for T ∊ [215K; 235K]. The range of variability for $N_{T,500}$ reveals a rather small overlap, if any, of 25th and 75th percentiles of neighboring MCS reflectivity zones 8, 7, and 6, mainly at coldest T ∊ [215K; 225K]. No overlap for MCS reflectivity zones 2-5 and concentration of ice hydrometeors beyond 500µm are rather constant from 215K to 265K for observations in MCS reflectivity zones 3 to 5.

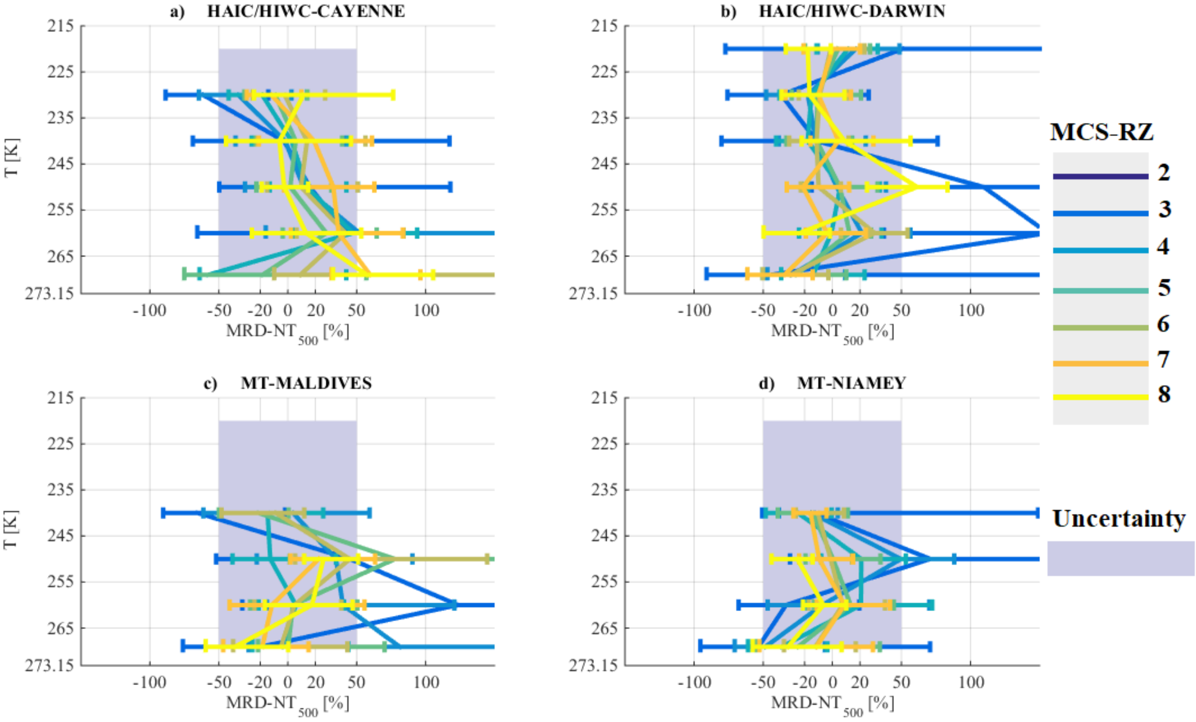

**Figure 12: Same as Figure 6, but for MRD-NT$_{500}$.**

Figure 12 (a), 12(b), 12(c), and 12(d) reveal that MRD-N$_{T,500}$ in higher MCS reflectivity zones are considerably smaller or roughly equal to the measurement uncertainty for large hydrometeors. Some smaller exceptions are noticeable where MRD-N$_{T,500}$ are larger than the measurement uncertainty for very low altitudes at T $\in$ [265K; 273.15K[, namely Cayenne in MCS reflectivity zones 7 and 8, and Darwin in MCS reflectivity zone 8. Note, that in general MRD-N$_{T,\ 500}$ have smaller 75th percentiles (from Figure 10 (b), 10(c), 10(d), and 10(e)) compared to respective MRD-N$_{T,50}$ and MRD-N$_T$, showing that variability in each MCS reflectivity zone for hydrometeors larger than 500µm is smaller than the variability of concentrations which include smaller (N$_{T,50}$) and smallest (N$_T$) hydrometeors. This finding is clearly related to the uncertainty estimation given by (Baumgardner et al., 2017)) that small hydrometeors (D$_{max}$< 100µm) have a larger estimated uncertainty of 100% (due to shattering, very small sample volume), compared to the uncertainty of only 50% for larger hydrometeors (D$_{max}$>100µm). Hence, it is not surprising that variability around a median value is larger for N$_T$ and N$_{T,55}$ than for N$_{T,500}$. It is important to resume here that not just MRD-N$_{T,500}$ is smaller than the uncertainty of 50%, but also that MRD-N$_{T,500}$ is tremendously smaller than MRD-N$_{T,50}$ and MRD-N$_T$. Even though we have to keep in mind that we'll never have sufficient statistics in flight data, due to sampling bias of flight trajectories and variability of microphysics from one system to another. Indeed, Leroy et al., (2017) demonstrated that median mass diameter MMD$_{eq}$ generally decrease with T and increasing IWC for the dataset of HAIC-HIWC over Darwin. However, for two flights performed in the same MCS, Leroy et al., (2017) showed that high IWC were linked to large MMD$_{eq}$, where MMD$_{eq}$ tends to increase with IWC. This demonstrates that comparable high IWC can be observed for two different microphysical conditions (short-lived typical oceanic MCS versus long lasting tropical storm in one and the same dataset).

We observe that total concentrations starting from 15µm can be different between MCS locations as a function of T and Z, especially in oceanic MCS over Maldives Islands in the more stratiform part of these MCSs where measured concentrations can reach 10 times the median concentrations observed for the merged dataset. Also MCS over Niamey show larger concentrations near the convective part of MCS. However, concentrations of ice hydrometeors beyond 50µm tend to be more similar as function of T and Z for all type of MCS, even if the limits between each MCS reflectivity zones are not well defined. Between 4 MCS locations, differences of aerosol loads and available ice nuclei might exist. Despite those possible differences, ice crystal formation mechanisms may be primarily controlled by dynamics, thermodynamics and particularly by secondary ice production rather than primary nucleation (Field et al., 2016; Phillips et al., 2018; Yano and Phillips, 2011) that regulate the concentrations of hydrometeors beyond ~55µm making these concentrations quiet rather similar for different MCS locations.

### 5.4 Coefficients of mass-size relationship

The relationship between mass and size of ice crystals is complex. Usually in field experiments the mass of individual crystals is not measured, instead bulk IWC is measured which is the integrated mass of an ice crystal population per sample volume to be linked to PSDs of ice hydrometeors. Yet IWC is not always measured or with low accuracy. Due to the complex shape of ice hydrometeors, various assumptions allow to estimate the mass of ice crystals for a given size. Indeed, many habits of ice crystals can be observed in clouds, primarily as a function of temperature and ice saturation (Magono and Lee, 1966; Pruppacher et al., 1998). Also hydrometeors of different habits can be observed at the same time (Bailey and Hallett, 2009). Locatelli and Hobbs (1974) and Mitchell (1996) suggested mass-size relationships represented as power laws with $m = \alpha \cdot D^{\beta}$ for different precipitating crystal habits. Coefficients $\alpha$ and $\beta$ vary as a function of the ice crystals habit. Further studies performed calculations of mean mass-size relationships (also using power law approximations) retrieved from simultaneous measurements of particle images combined with bulk ice water content measurements (Brown and Francis, 1995; Cotton et al., 2013; Heymsfield et al., 2010). Schmitt and Heymsfield (2010), Fontaine et al (2014), Leroy et al. (2016) showed that mass-size relationship coefficients $\alpha$ and $\beta$ vary as a function of temperature. In the latter studies, coefficient $\beta$ is calculated from OAP images, and then α is retrieved either also from processed images or constrained with integral measured IWC or radar reflectivity factor Z. Recently, Coutris et al (2017) retrieved masses of hydrometeors by an inverse method using direct measurement of PSD and IWC. In this latter study, the mass of ice crystals is retrieved without any assumption on the type of function linking mass and size of ice hydrometeors.

This study uses the power law assumption to constrain the mass of ice hydrometeors. Thereby, the β exponent of the mass-size power law relationship is calculated (Eq. 5) as presented in Leroy et al (2016) for hydrometeors defined by $D_{max}$ dimension:

$$\beta = 1.71 \cdot f_s - 0.62 \cdot f_p \qquad (5)$$

Here, $f_p$ is the exponent and $e_p$ is the pre-factor of the perimeter-size power law relationship (Duroure et al. 1994) with $P(D_{max}) = e_p \cdot D_{max}^{fp}\ [cm]$ while $f_s$ is the exponent and $e_s$ is the pre-factor of the 2D image area-size relationship (Mitchell, 1996) with $S(D_{max}) = e_s \cdot D_{max}^{fs}\ [cm^2]$. These two relationships are calculated using Images from 2D-S and PIP. Hence, $\beta$ is a proxy parameter that describe the global (all over the size range of hydrometeors from 50µm to 1.2cm) variability of the shape of the recorded hydrometeors during the sampling process (Leroy et al., 2016; Fontaine et al., 2014). Figure 13 shows the variability of $\beta$ as a function of temperature and MCS reflectivity zones for the merged dataset. For a given MCS reflectivity zone, $\beta$ increases with increasing temperature. Also for a given temperature, $\beta$ increases with MCS reflectivity zone, although MCS reflectivity zones 4, 5, 6, 7, and 8 share a range of common values for $\beta$, making it more uncertain to predict with a good accuracy using a parametrization as function of IWC and T.

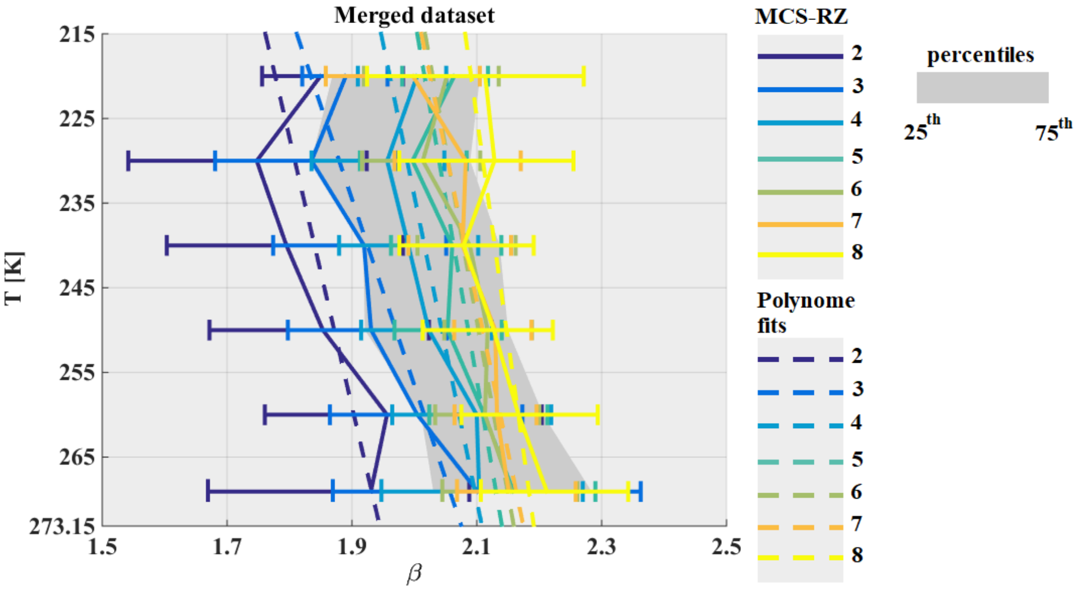

**Figure 13: As Figure 5, but for exponent β of mass-size relationships for used ice hydrometeor size definition $D_{max}$.**

In order to estimate the uncertainty on the calculation of $\beta$ (grey band in Figure 14 (a), (b), (c), and (d)), results from Leroy et al., (2016) have been used, with U(β)/β=±2.3%. However, if we had calculated the uncertainty on retrieved $\beta$ from the uncertainty on the measurement of the size and concentration of hydrometeors from OAP images, the uncertainty would have been by about 44%. Considering the small range of variability for $\beta$ (1 to 3), the uncertainty given by Leroy et al., (2016) allow to highlight some differences overall ice particle habit. In general, MRD-$\beta$ in MCS reflectivity zones 8 and 7 tend to be in the range of U($\beta$)/$\beta$ assuming that $\beta$ are similar for all observed MCS in the four campaigns for the conditions described by MCS reflectivity zones 7 and 8.

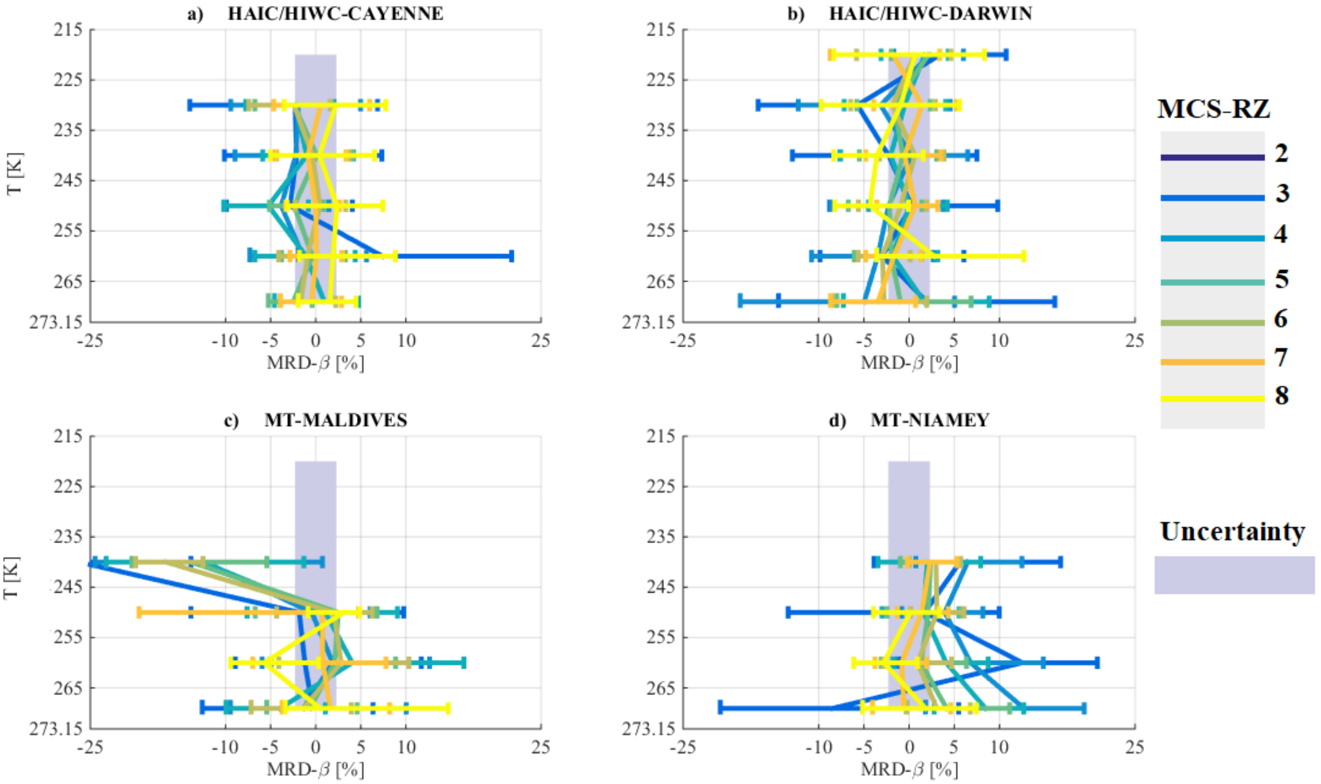

**Figure 14: As Figure 6, but for exponent MRD-β.**

However, in MCS reflectivity zones 2 to 6 MRD-β are more scattered around U(β)/β with sometimes larger MRD-β than uncertainty of β. Especially for MCS over Maldives and Niamey. Over Maldives at higher altitudes β tend to be smaller compared to the median β calculated for the merged dataset. While, MCS over Niamey tend to have β larger than median β calculated for the merged dataset.

Overall, the predictability of β coefficients as a function of T and MCS reflectivity zone remains challenging. We are aware of the fact that the power-law approximation has certain limits, trying to impose one single β to an entire crystal population composed of smaller (dominated by pristine ice) and larger crystals (more aggregation, also riming).

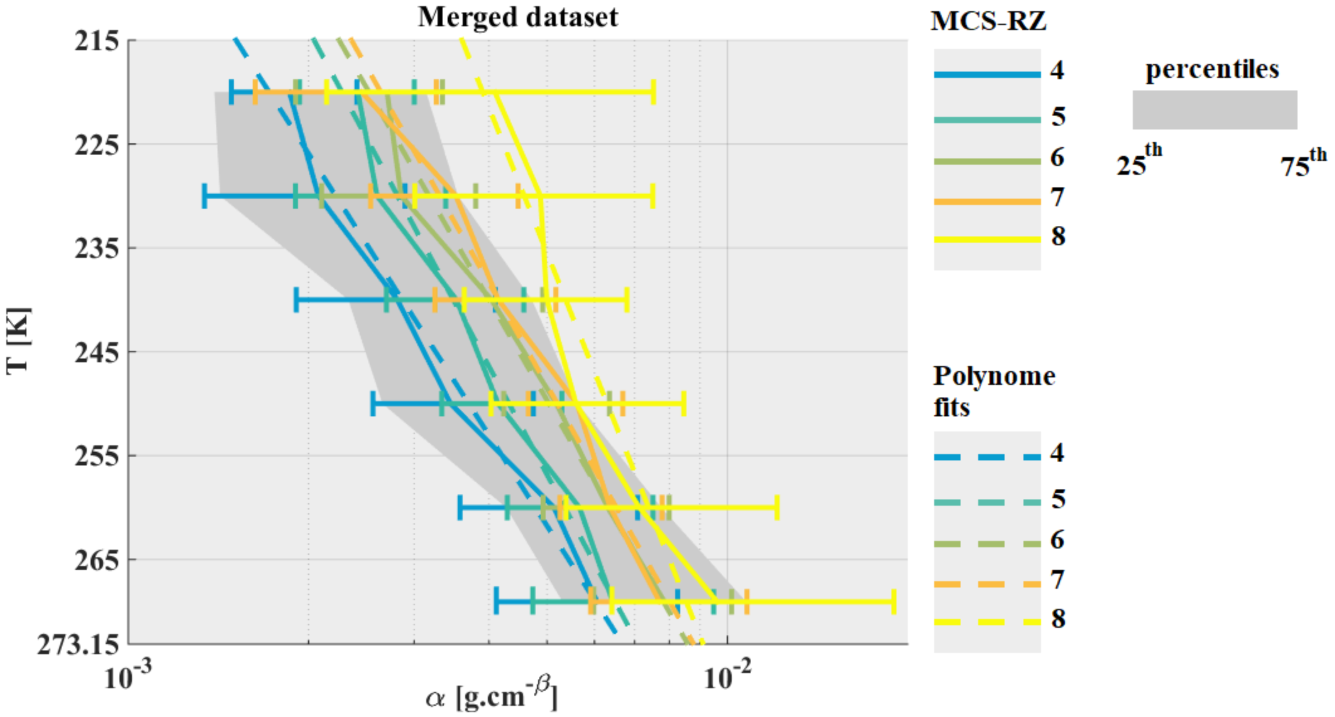

**Figure 15: Same as Figure 5, but for α of mass-size relationships for used ice hydrometeor size definition $D_{max}$.**

For HAIC-HIWC datasets, coefficients α are retrieved, while matching measured IWC from IKP-2 with calculated IWC thereby integrating PSD times m(D) power law relationship. For Maldives and Niamey datasets, coefficients α are retrieved from T-matrix simulations of the reflectivity factor (Fontaine et al., 2017).

For both situation, α calculation is solely constrained by the fact that the mass of ice crystals remains smaller or equal than the mass of an ice sphere with the same diameter $D_{max}$:

$$\alpha = \frac{IWC}{\sum_{15}^{12845} N(D_{max})\cdot D_{max}^{\beta}\cdot \Delta D_{max}} \quad | \quad \alpha \cdot D_{max}^{\beta} \le 0.917 \cdot \frac{\pi}{6} \cdot D_{max}^{3} \qquad \left[g\ cm^{-\beta}\right]. \tag{6}$$

For the uncertainty calculation of α we take the maximum value of β which is 3:

$$\frac{U(\alpha)}{\alpha} = \sqrt{\left(\frac{U(IWC)}{IWC}\right)^2 + 3\cdot\left(\frac{U(D)}{D}\right)^2 \left(\frac{U(N)}{N}\right)^2} \tag{7}$$

Figure 15 shows median α coefficients as a function of T and MCS reflectivity zone. As it has been already stated in previous studies, α is strongly linked to the variability of β (Fontaine et al., 2014; Heymsfield et al., 2010). Figure 15 compared to Figure 13, confirms that results for α have similar trends as those discussed for β. However, α vary from $5.10^{-4}$ (in MCS reflectivity zone 2) to $\approx 2.10^{-2}$ (in MCS reflectivity zone 8). In general, α increases as a function of T for a given MCS reflectivity zone and also increases as a function of MCS reflectivity zone (and associated IWC) for a given T level. As already stated for the median exponent β in Figure 13, median α in MCS reflectivity zones 4, 5, 6, 7 and 8 are more or less overlapping.

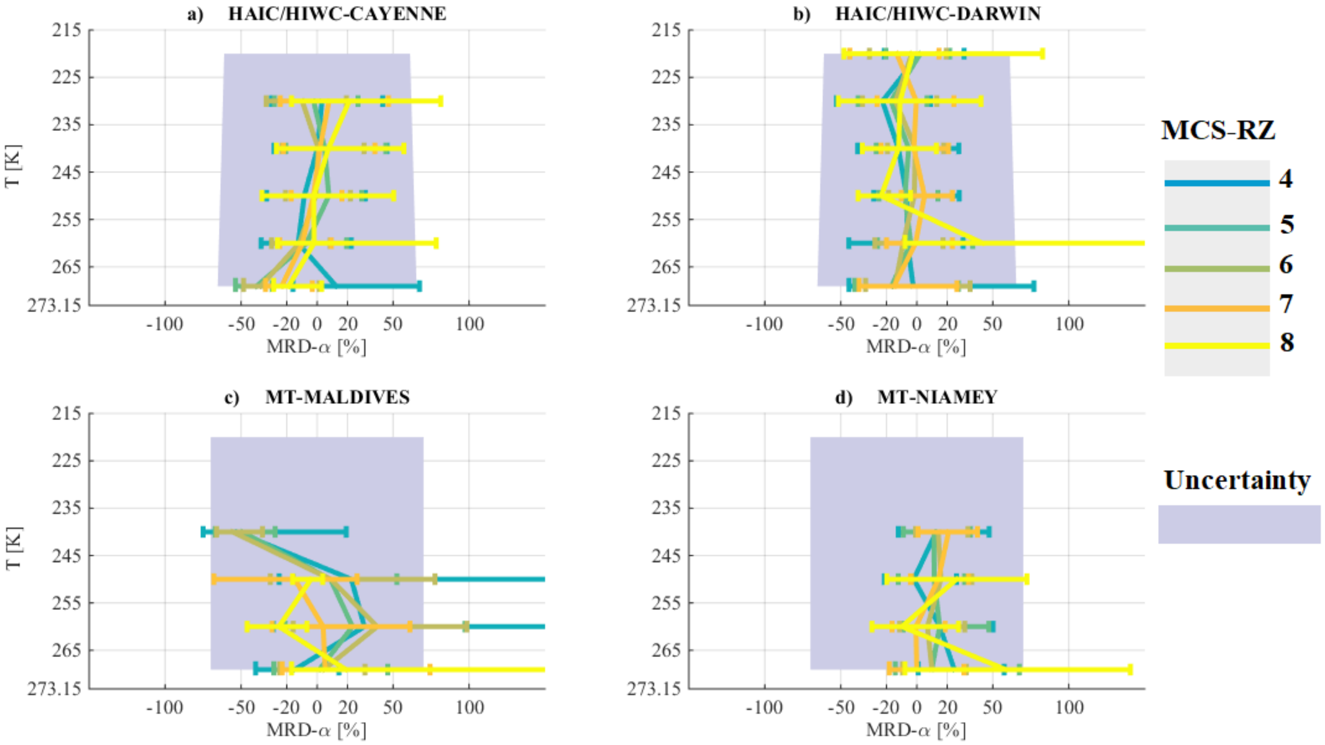

**Figure 16: As Figure 6, but for exponent MRD-α.**

From Figure 16(a) and Figure 16(b), we note that even with a good accuracy of the measured IWC (from IKP-2; U(IWC)/IWC ≈ ±5% for the typical IWC values observed in HAIC-HIWC at 210K), the uncertainty of α, is rather large which is mainly due to uncertainties in OAP size and concentration measurements. Taking into account the large uncertainty on the retrieved α, we find that MRD-α for all 4 merged datasets for MCS reflectivity zones 4, 5, 6, 7, and 8 are smaller than U(α)/α. For observations from Niamey (Figure 16 (d)), α tend to be larger than median α for the merged dataset (MRD-α not centered on 0, but shifted to positive values).

In previous sections, this study documented similar IWC values and visible extinction coefficients for a given range of Z and T and a clear increase of IWC and visible extinction coefficient from MCS reflectivity zones 4 to 8. The increase of α and β with MCS reflectivity zones is not as much clearly visible, whereas at least α seems to increase with temperature in different

MCS reflectivity zones). Moreover, we cannot ignore that $\alpha$ and $\beta$ tend to be larger in MCS reflectivity zone 8 than in MCS reflectivity zone 4, especially at higher altitude. But, the increase of IWC and visible extinction with MCS reflectivity zone Z is not linked to an increase of the mass-size coefficients. This conclusion takes into account the variability of the mass-size coefficients shown by 25 and 75 percentiles. Furthermore, ice hydrometeors habits describe with $\beta$ in MCS reflectivity zone 4, 5 and 6 are different in MCS over Maldives and MCS over Niamey compared to MCS over Darwin and Cayenne (smaller $\beta$ over Maldives and larger $\beta$ over Niamey).

Because visible extinction (hence projected surface) and IWC are similar for the same range of T and Z in all types of MCS, but the shapes of crystals might be different from one to another MCS location. We assume that ratio of projected surface vs IWC is similar. In other words the density of ice per surface unity (or by pixels of projected surface) is similar as function of T and Z in all types of MCS even if there might be a possibility that the habit or the shape can be different (pure oceanic MCS vs pure continental MCS). Note that these assumptions are established for IWC larger than 0.1g $m^{-3}$.

### 5.5 Largest ice hydrometeors

Figure 17 investigates the variability of the size of the largest ice hydrometeors in the PSD (hereafter max($D_{max}$) as defined in Fontaine et al (2017)). Figure 17 reveals for all MCS reflectivity zones that the median of max($D_{max}$) increases with T, with larger hydrometeors at cloud base compared to cloud top, particularly in the stratiform cloud part, where PSD are mainly impacted by a combination of aggregation and sedimentation. At higher levels for T $\in$ [215K; 245K[ largest median of max($D_{max}$) are observed in the most convective MCS reflectivity zone 8, followed by zones 7, 6, and 5, where sedimentation becomes more and more active. Below the 250K level, largest max($D_{max}$) can be observed in MCS reflectivity zones 6 and 7 (still significant sedimentation source from above), followed by 5 (increasing depletion of large crystals) and 8 (more convective or at least transition zone from convective to stratiform cloud part). Smallest max($D_{max}$) are observed in MCS reflectivity zones 2 and 3.

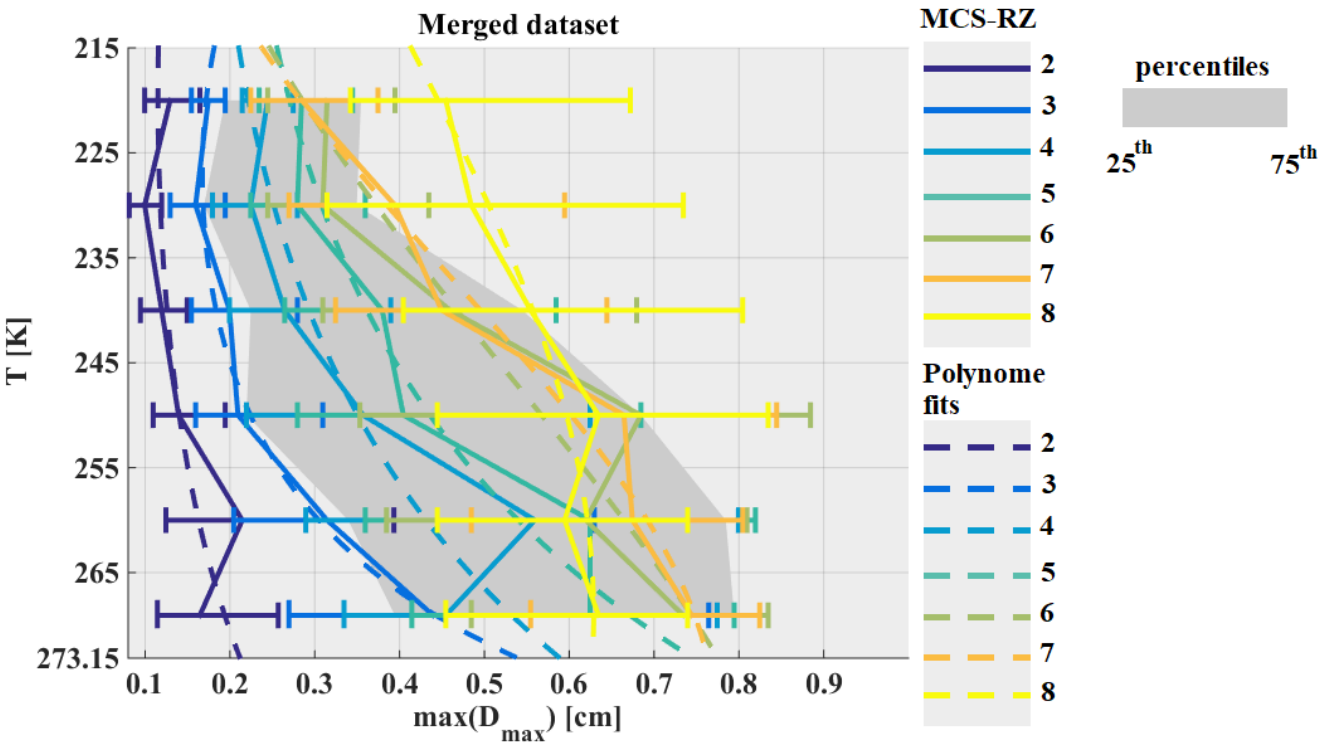

**Figure 17: As Figure 5, but for maximum size of hydrometeors max($D_{max}$) in PSD in [cm].**

MRD-max($D_{max}$) shown in Figure 18(a), 18(b), 18(c), and 18(d) are a bit larger than the measurement uncertainty estimated with ±20% ( (Baumgardner et al., 2017). Cayenne, Darwin, and Niamey data are centered around the median max($D_{max}$) of the merged dataset in MCS reflectivity zone 8 for all type of MCSs, in MCSs reflectivity zone 7 for MCS over Darwin, Cayenne and Niamey. MCSs over Cayenne and Darwin tend to have similar max($D_{max}$) in other MCS reflectivity zones. Maldives dataset shows mainly negative MRD-max($D_{max}$) values, indicating that max($D_{max}$) for the Maldives Island data are generally smaller than those of the other three tropical locations. Also MCS over Niamey show larger max($D_{max}$) in MCS reflectivity zones 2 to 4, illustrating that snow aggregates can reach larger sizes during the West African monsoon than in other MCS locations. It confirms conclusions from Frey et al., (2011) and Cetrone and Houze (2009), who suggest that there are larger ice hydrometeors in MCS over continent than MCS over maritime regions.

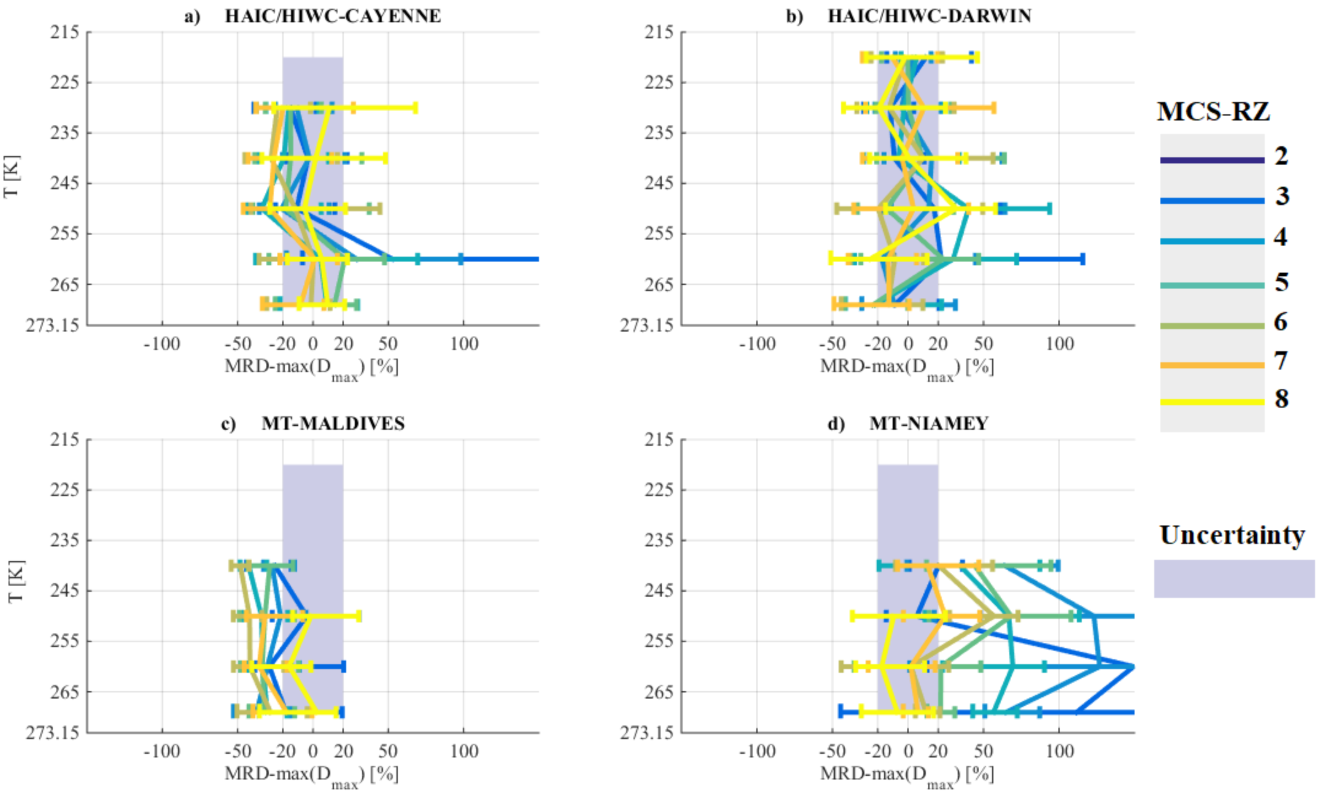

**Figure 18: As Figure 6, but for maximum size of hydrometeors max($D_{max}$)**

In this section, it is shown that in the stratiform part of MCS, largest hydrometeors are larger in MCSs over Niamey than in other types of MCS and tend to be smaller in MCS over Maldives Islands. Mainly, large crystals (Dmax > 1mm) are agglomerates of pristine ice crystals, for which the growth process is leaded by aggregations (by sedimentation) instead of vapour diffusion. There is a possibility that largest hydrometeors are large pristine ice. Indeed, some large pristine ice (large dendrites) were found in the dataset (especially over Maldives see Figure 1 in Fontaine et al., 2014). However, their size do not exceed 3 to 4 mm. Hence, aggregation efficiency is different from one MCS type of MCS to another, this could explain the differences of mass-size coefficient β, as it is calculated using the slope in a log-log scale of mean perimeter and mean surface as a function of median diameter in each size bin; where large hydrometeors have a non-negligible impact on the slope (i.e. fp and fs, see Eq. (5)).

### 5.6 note on the impact of vertical velocity on ice microphysic

This section discuses about the results of an investigation performed about the impact of vertical velocity on ice microphysical parameters presented earlier in this section 5. Aside the statistic performed on the merged dataset where vertical velocity are not considered, similar statistics were calculated for three sub-datasets such: i) $w < -1$ m $s^{-1}$ , (ii) $-1$ m $s^{-1} < w < 1$ m $s^{-1}$ and (iii) $w > 1$ m $s^{-1}$. Then, median relative difference for the three conditions and for each parameters presented in this section 5 were calculated and compared to the median relative difference when no distinction is performed as function of vertical velocity. Firstly, we noticed that MRD-X for the merged dataset and MRD-X for the second condition (i.e. 1 m $s^{-1} < w < 1$ m $s^{-1}$) are similar (MRD-X: X being used to replace IWC, σ, NT, $NT_{50}$, $NT_{500}$, β, α, max(Dmax)). Secondly, differences of MRD-X in updraft and in downdraft with regards to MRD-X for merged dataset and no vertical movement are visible. But most of the times these differences are of the order of or smaller than measurement uncertainties (U(X)/X). Hence, the impact of vertical velocity (>0 m $s^{-1}$ or < 0 m $s^{-1}$) on ice microphysic parameters presented in section 5 is not significant; except for IWC, NT and $NT_{50}$. Figures for these latter parameters are presented in Appendices B.

Appendices B shows when updraft have an impact on IWC $N_T$ and $N_{T,50}$ for a given range of temperature and MCS reflectivity zones. Figure B1 shows MRD-IWC, Figure B2 shows MRD-$N_T$ and Figure B3 shows MRD-$N_{T,50}$. For the others parameters impact of updraft are uncommon.

It appears that updraft tends to impact mainly concentrations of small hydrometeors and IWC for some type of MCS and some MCS reflectivity zones. So for $N_T$ (Figure B2), we observe larger $N_T$ for updraft in MCS observed over Cayenne, Maldives and Niamey. For Cayenne, we get similar conclusion in MCS reflectivity zone 5 and 6 for temperatures between 245K and 265 K with $N_T$ 2 to 3 times larger than $N_T$ for merged dataset. For MCS over Maldives, median $N_T$ are 5 times to 20 times larger than $N_T$ when there is no noticeable vertical movement in MCS reflectivity zones 6, 7 and 8. Finally, for MCS over Niamey, we observe larger $N_T$ in updraft than $N_T$ for the merged dataset in MCS reflectivity zones 6 for T around 240 K and in MCS reflectivity zones 8 above the bright band. We have similar conclusions for $N_{T,50}$ (Figure B3), except that ratios between $N_{T,50}$ in updraft and $N_{T,50}$ when no updraft is smaller than the ratio between $N_T$ in updraft and $N_T$ when no updraft.

IWC are impacted by updraft, only for MCS over Cayenne, in MCS reflectivity zone 4, 5, 6 and 7. IWC in updraft tend to be larger about +50% than IWC when no updraft, except in MCS reflectivity zones 5 where IWC are about 2 times larger in updraft than IWC when no updraft.

This investigation on the impact of updraft and downdraft on ice microphysics, shows that updraft may have an impact on concentrations of small hydrometeors and IWC. However, updraft does not impact all type of MCS in the same way. So, there will need to perform deeper investigations on updraft impact.

Despites some noticeable impact of updraft on ice microphysic for our datasets, there is no significant (recurrence trough all types of MCS or as function of T or Z) results to assess them for the merged dataset. So, parameterizations developed in the next section are only as function of IWC and T, with no consideration of convective movement.

## 6. Parameterizations as function of IWC and T

### 6.1 visible extinction

We concluded from Figure 7 and Figure 8 that visible extinction σ and IWC in tropical MCS tend to be similar for all MCS locations in the same range of T and for corresponding MCS reflectivity zones 4 to 8. Then, Figure 19 shows that there is a linear relationship between log(σ) and log(IWC). And log(σ) decrease with temperature increasing at constant log(IWC). Then, we performed a surface fitting using input coefficients log(IWC) and T to fit log(sigma) to deduce a parametrization of σ (Eq. (8)) as a function of IWC and T. This parameterization is limited for deep convective cloud (merged dataset) and data with IWC > 0.1g $m^{-3}$:

$$\sigma = exp(-0.0194587 \cdot T + 0.9134019 \cdot ln(IWC) + 1.2423609) \qquad [m^{-1}] \qquad (8)$$

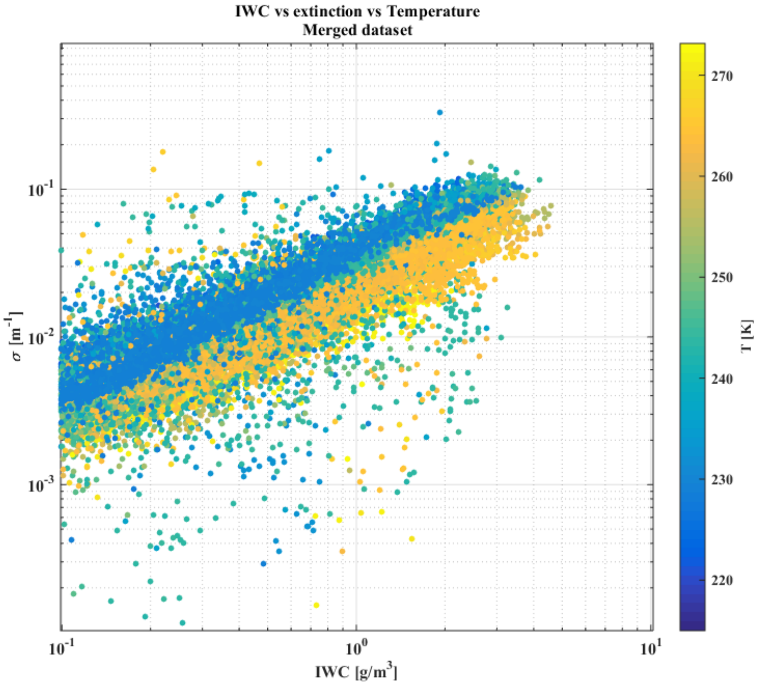

**Figure 19: visible extinction in [m$^{-1}$] on y-axis as function of IWC in [kg m$^{-3}$] on x axis and as function of T in [K] indicated by the color scale. Scatter plot using the merged dataset (4 campaigns).**

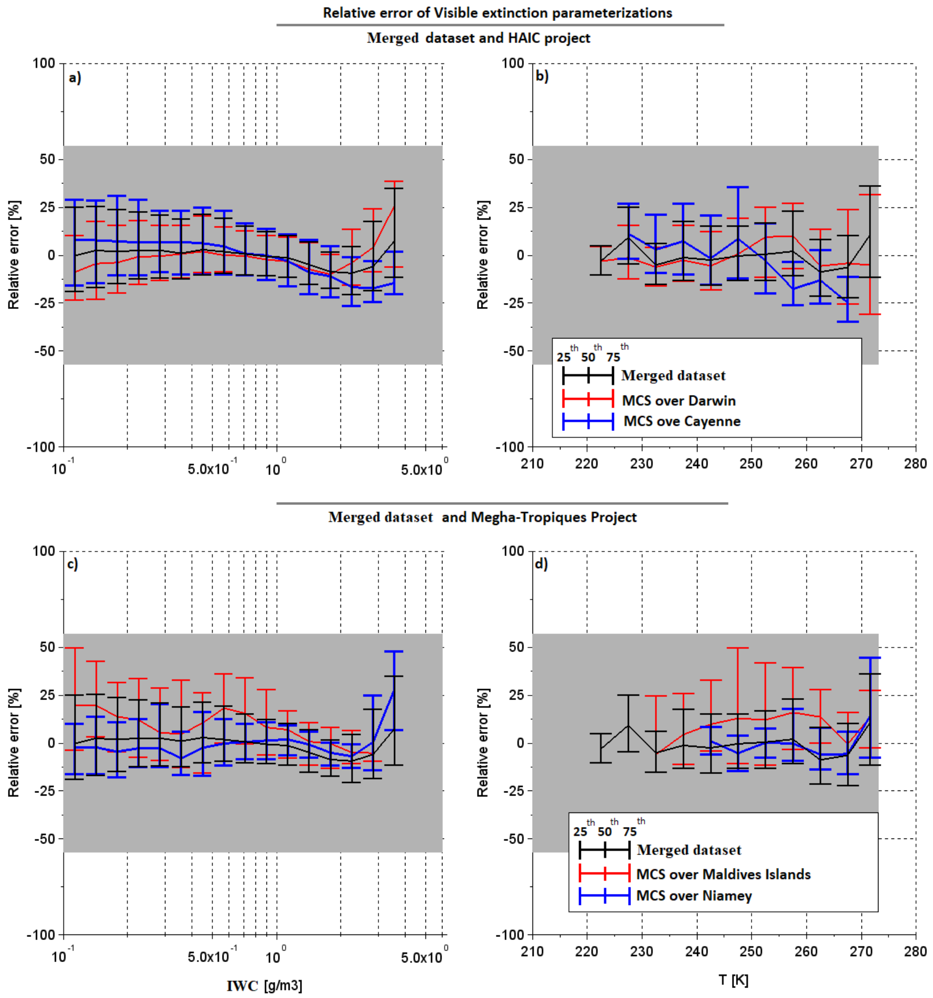

**Figure 20: Relative errors of predicted visible extinction Eq. (8) with respect to measured visible extinction for a), b), c), and d. Relative errors as a function of IWC in a) and c) and as a function of T in b) and d). Black lines in 4 sub figures represent the relative errors when calculated for the merged dataset. In a) and b) red lines show median relative error for MCS over Darwin, and blue line for MCS over Cayenne. In c) and d) red line represent median relative errors for MCS over Maldives Islands and blue lines for MCS over Niamey. Bottom of error bar shows 25th percentiles of relative errors and 75th percentiles are given by top of error bar.**

An evaluation of this parametrization is presented in Figure 20, where black lines in Figure 20-a) to Figure 20-d) represent median relative errors of σ (with 25th and 75th percentiles represented by whiskers) for the merged dataset predicted with Eq. (8), with respect to retrieved σ from OAP images from Eq. (1). In addition, median relative errors of σ for individual MCS datasets over Darwin, Cayenne, Maldives Islands, and Niamey with respect to σ calculations (Eq. (8)) are shown in Figure 20(a), Figure 20(b), Figure 20 (c), and Figure 20(d), respectively. The uncertainty $\pm \frac{U(\sigma)}{\sigma}$ is given with the grey band. All relative errors (25th - 75th percentiles) tend to be smaller than $\pm \frac{U(\sigma)}{\sigma}$, with median relative errors that are smaller than ±25% of σ uncertainty calculated from Eq. (2). In general, Eq. (8) seems to produce smallest relative errors for σ of Niamey and Darwin datasets (especially for IWC<2 g $m^{-3}$).

Noteworthy, optically thick clouds are responsible of large errors in retrieved cloud water path and condensed water concentration profiles retrieved from satellite imageries (Smith, 2014; Yost et al., 2010). Parameterizations, such as presented here, could help to improve retrieval methods on cloud water path but more investigations on the benefit of such parameterizations are needed, which is beyond the scope of this study.

### 6.2 Parameterization of ice hydrometeors distributions

#### 6.2.1 Observations of PSD moment

Moments of PSD are convenient for numerical weather prediction to model microphysics of hydrometeor populations, since knowing the PSD nth order moment allows to roughly describe cloud processes and their hydrometeors properties. Commonly, PSD of ice hydrometeors are modeled with Gamma distributions (Heymsfield et al., 2013; McFarquhar et al., 2007). The calculation of the nth order moment is defined in Eq. (9) for PSD obtained from measurements of hydrometeors images, for example with OAP:

$$M_n = \sum_{D_{max}=50\mu m}^{D_{max}=1,2cm} N(D_{max}) \cdot D_{max}^{n} \cdot \Delta D_{max} \qquad [m^{n-3}] \qquad (9)$$

The uncertainty of the nth (n=2 and 3 in our study) moment is:

$$\frac{U(M_n)}{M_n} = \sqrt{n \cdot \frac{U(D)^2}{D} + \frac{U(N)^2}{N}} \qquad (10)$$

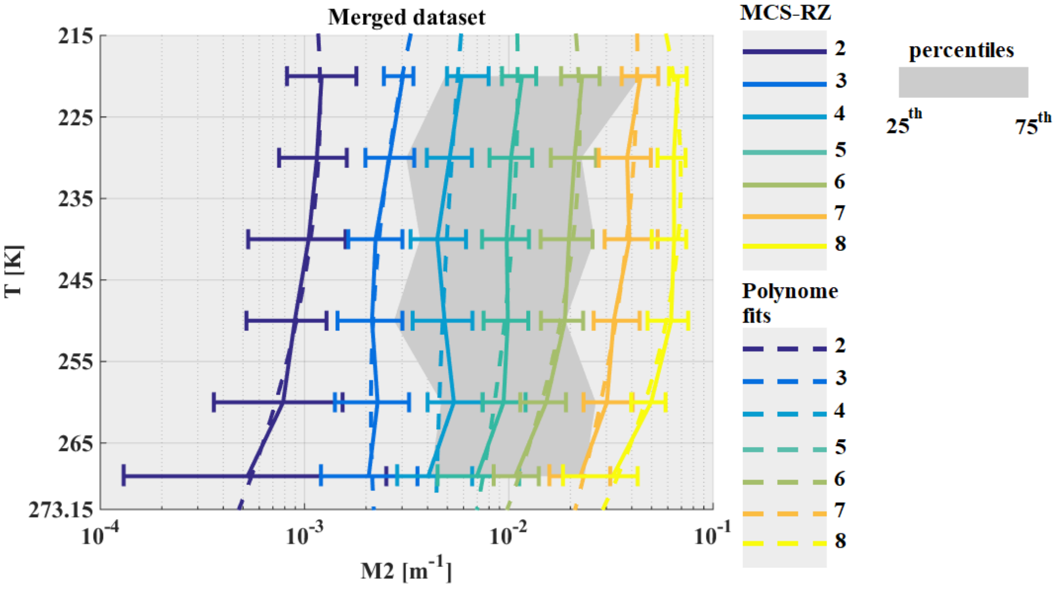

**Figure 21: Same as Figure 5, but for $M_2$ per meter.**

Figure 21 shows median second moment $M_2$ as a function of T for all MCS reflectivity zones for the merged dataset. Median $M_2$ slightly decrease with temperature for all individual MCS reflectivity zones, and distinctly increase with MCS reflectivity zone for a given T. The range of variability of median $M_2$ shows mainly negligible overlap, if any, of 25th and 75th percentiles of neighboring MCS reflectivity zones with the exception between MCS reflectivity zones 8 and 7 at low altitude (T ∈[265; 273.15[).

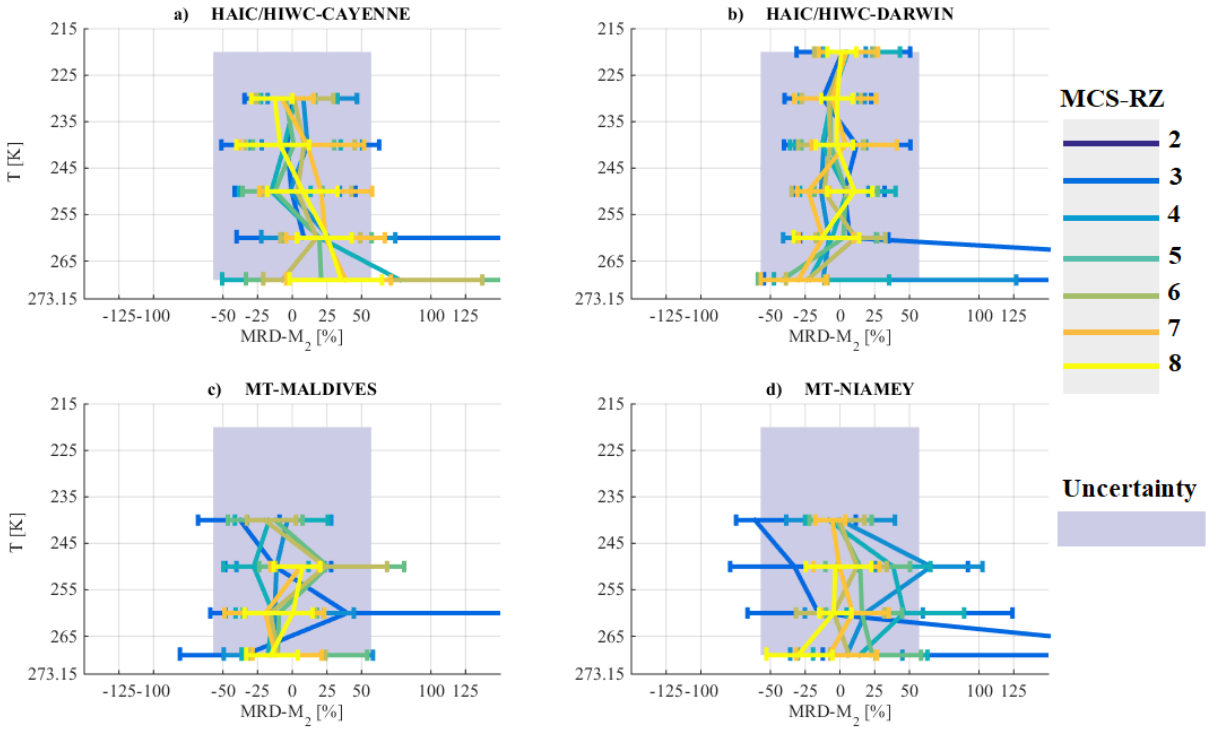

**Figure 22: Same as Figure 6, but for MRD-M2.**

All 4 tropical MCS (Figure 22 (a), (b), (c), and (d)) show good agreement with the medians of $M_2$ in MCS reflectivity zones 3 to 8, with MRD-$M_2$ significantly smaller than U($M_2$)/$M_2$. Few minor exceptions can be found for MCS over Cayenne (Figure 22 (b)) and Darwin (Figure 22 (c)) in the temperature range [265K; 273.15[. Also MCS over Niamey (Figure 22 (e)) show a larger MRD-$M_2$ in MCS reflectivity zones 2 and 3 for T ∈ [265K; 273.15K[ and T ∈ [245K; 255K[, respectively.

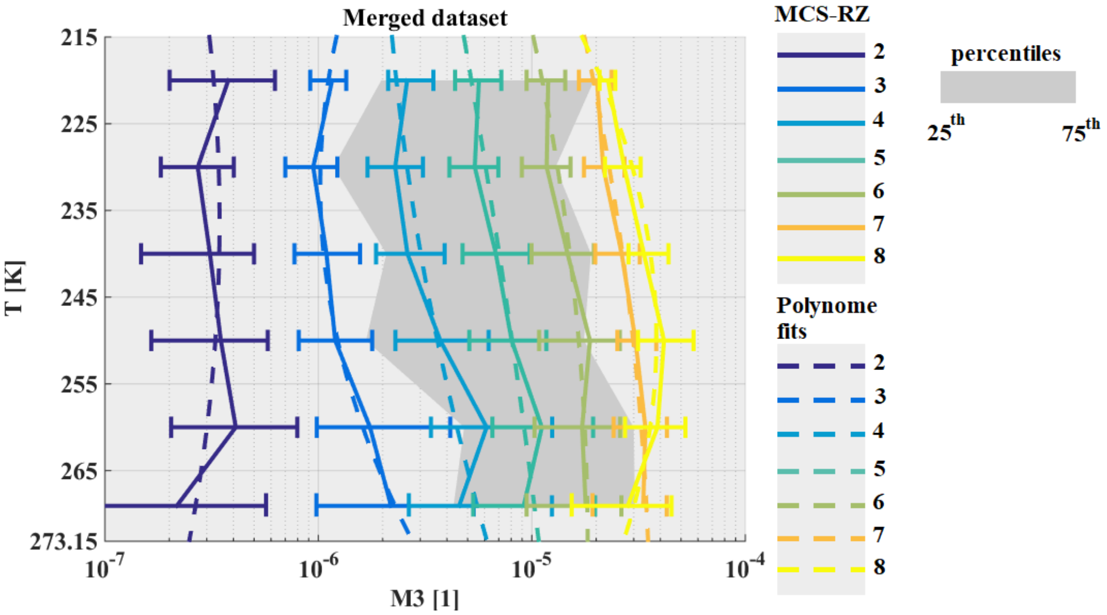

**Figure 23: Same as Figure 5, but for the $M_3$ for unity dimension.**

Figure 23 presents median third moment $M_3$ for merged dataset as a function of T and for different MCS reflectivity zones. Median $M_3$ in highest MCS reflectivity zones 8, 7, and to some extent zone 6 resemble the corresponding curves of median IWC (Figure 5), with a maximum value for median $M_3$ for T ∈ [245K; 260K[. We also note an increase of median $M_3$ with

MCS reflectivity zone from 2 to 8. The range of variability for $M_3$ reveals no overlap of 25th and 75th percentiles of neighboring MCS reflectivity zones 2-7, solely zone 7 overlaps with zone 8 for all temperatures. Third moment of MCS over Cayenne, Darwin and Maldives Islands in MCS reflectivity zones 2 to 8, shows MRD-$M_3$ smaller than $U(M_3)/M_3$, with few minor exceptions basically in the range of $T \in [265K; 273.15K[$. MCS over Niamey tend to have MRD-$M_3$ that are sometimes larger than $U(M_3)/ M_3$. Indeed, $M_3$ for MCS over Niamey tend to be larger in MCS reflectivity zones 5 and 2 in the range of $T \in [265K; 273.15K[$, and in MCS reflectivity zone 4 for T larger than 255K as well as in MCS reflectivity zone 3 for T larger than 245K.

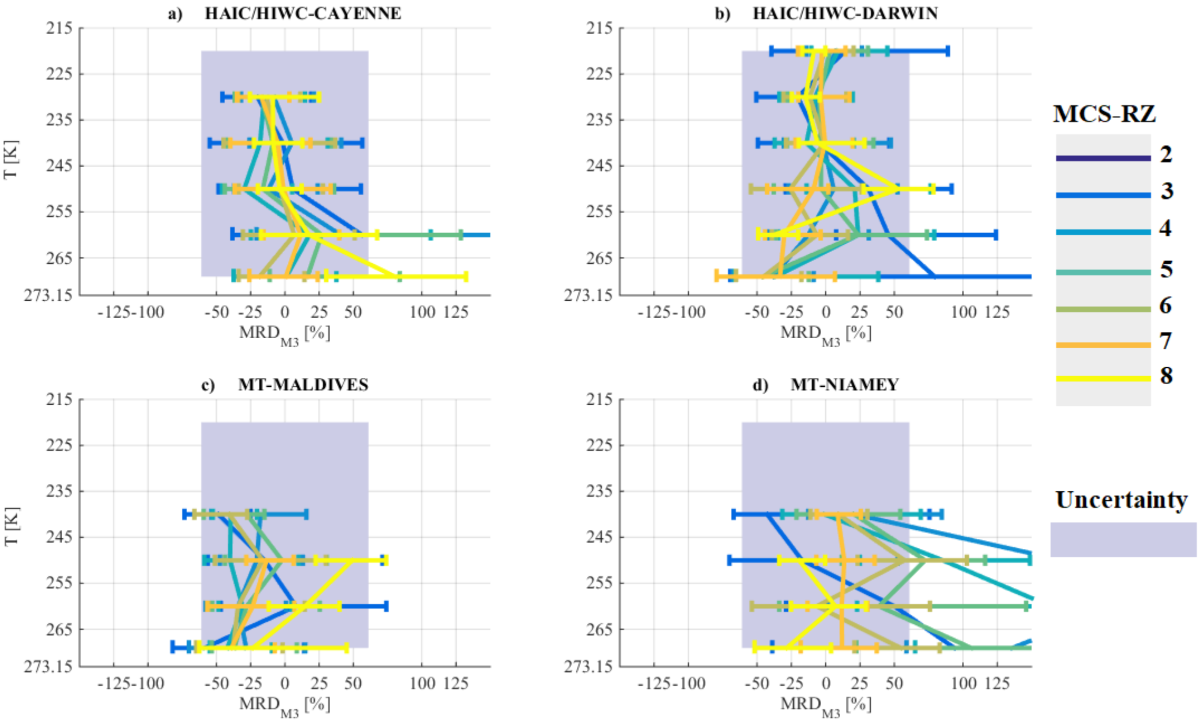

**Figure 24: Same as Figure 6, but for the $M_3$.**

Overall, this section illustrates that second and third moments of PSD are similar as a function of T and Z for all MCS locations of the underlying dataset. However, there are exceptions in MCS reflectivity zones 2, 3 and 4 in MCS over Niamey where larger third moments are calculated compared to those deduced for the merged dataset. Despite those exceptions, the next section explores the possibility to parameterize the second and third PSD moments as a function of IWC and temperature.

### 6.2.2 Parameterizations of $M_2$ and $M_3$

This section presents parametrizations to predict the 2nd and 3rd moment of the PSD for the merged dataset as a function of T and IWC (for this section IWC in the next equations are in [kg $m^{-3}$]), including IWC data larger than 0.1g $m^{-3}$. Indeed some moments can be directly linked to bulk properties of hydrometeor populations. For example, moment $M_0$ for ice and liquid hydrometeors is equal to the total number concentration ($N_T$), moments $M_2$ and $M_3$ for liquid particles are proportional to visible extinction and liquid water content. However, for ice hydrometeors the physical interpretation of moments $M_2$ and $M_3$ is less obvious since ice hydrometeors are not spherical particles. The results for α and β coefficients of the $m(D_{max})$ relationship presented in section 5.4, illustrate that β varies between 1.5 and 2.3. This means that IWC is proportional to PSD moments between $M_{1.5}$ and $M_{2.3}$. Also uncertainties on the retrieved β coefficients do not allow to assess the variability of β as a function of IWC and T. Former studies performed in different cloud environments report mean values of β around 2. For example, Leroy et al., (2016) found β=2.15 for HAIC-HIWC in Darwin, Cotton et al., (2013) suggested β=2.0, Heymsfield et al., (2010) suggested β=2.1, and Brown and Francis (1995) established β=1.9. We are also aware of the fact that findings of β also depend on the utilized size parameter ($D_{max}$, $D_{eq}$, etc…) of 2D images (Leroy et al., 2016). Hence, we decide to apply β=2 as an approximation, also proposed by Field et al., (2007), in order to link the second moment of hydrometeor PSD with IWC (Eq. 11). Subsequently, the ratio IWC/$M_2$ is calculated and denoted A.

$$M_2 = \frac{IWC}{A} \qquad [m^{-1}] \tag{11}$$

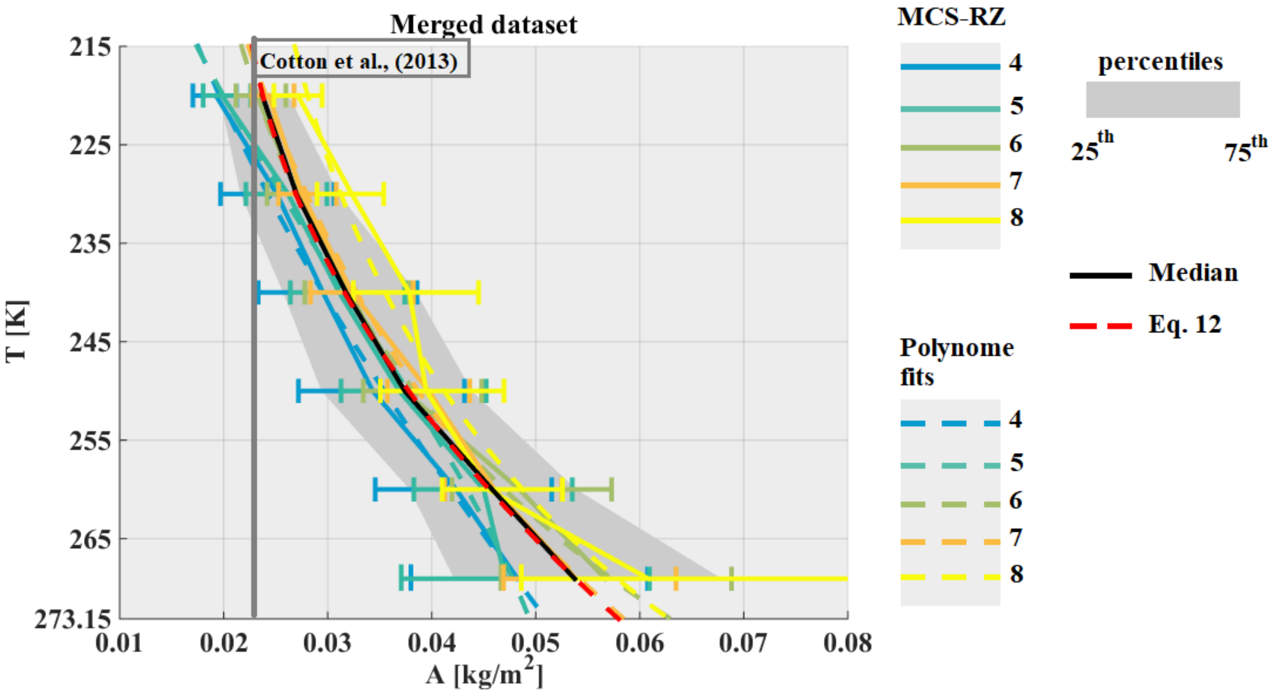

**Figure 25: Same as Figure 5, but for the ratio A= IWC/$M_2$ in [kg.m$^{-2}$].**

Figure 25 shows retrieved median coefficients A for the merged dataset as a function of MCS reflectivity zones and T. Note that A is calculated in SI units (in Eq. (11) IWC is in kg m$^{-3}$). The black solid line gives the median of A as a function of T, thereby merging all MCS reflectivity zones for the merged dataset with IWC > 0.1g m$^{-3}$. The grey band gives corresponding 25th and 75th percentiles of that median A. In addition, are calculated median A for all individual MCS reflectivity zones (on Figure 25) are solely illustrated median A for zones 4 to 8) for the merged dataset as a function of T. In general, median A calculated for individual MCS reflectivity zones 5, 6 and 7 are very similar to the median A when merging all MCS reflectivity zones (black solid line), whereas median A calculated for MCS reflectivity zone 4 tends to have smaller A values and median A calculated for MCS reflectivity zone 8 have larger median A values than the overall median A (all MCS reflectivity zones merged) for comparable temperatures.

However, when taking into account the variability in median A calculated for individual MCS reflectivity zones and associated 25th and 75th percentiles, we can state that median A generally increases with T, however it is not possible to assess that A increases with MCS reflectivity zones or IWC at constant temperature. As a comparison, we include the value of the pre-factor $\alpha$ (in SI unity) from Cotton et al. (2013) mass-size relationship ($\beta$=2.0, as is for second moment $M_2$, and $\alpha$=0.0257). Clearly, $\alpha$=0.0257 is not suited for deep convective systems as it represents ice crystals for T $\in$[215K; 225K[.

Figure 26 (a-d) illustrate that MRD-A are significantly smaller than U(A)/A, (same uncertainty than $\alpha$: $U(\alpha)/\alpha = U(A)/A$) with median MRD results centered around 0%. Comparing results of A (Figure 26) with results presented for $\alpha$ (Figure 15, section 5.4) it is obvious in terms of variability and MRD in each type of MCS that A is better adapted to parametrize the PSD 2nd moment as a function of T. Eq. (12) fits the median of ratio A for the merged dataset (red dashed line, all MCS reflectivity zones merged), as a function of T in deep convective systems for IWC larger 0.1g m$^{-3}$:

$$A(T) = 0.0000075 \cdot T^2 - 0.0030598 \cdot T + 0.3334963 \qquad [kg\ m^{-2}] \tag{12}$$

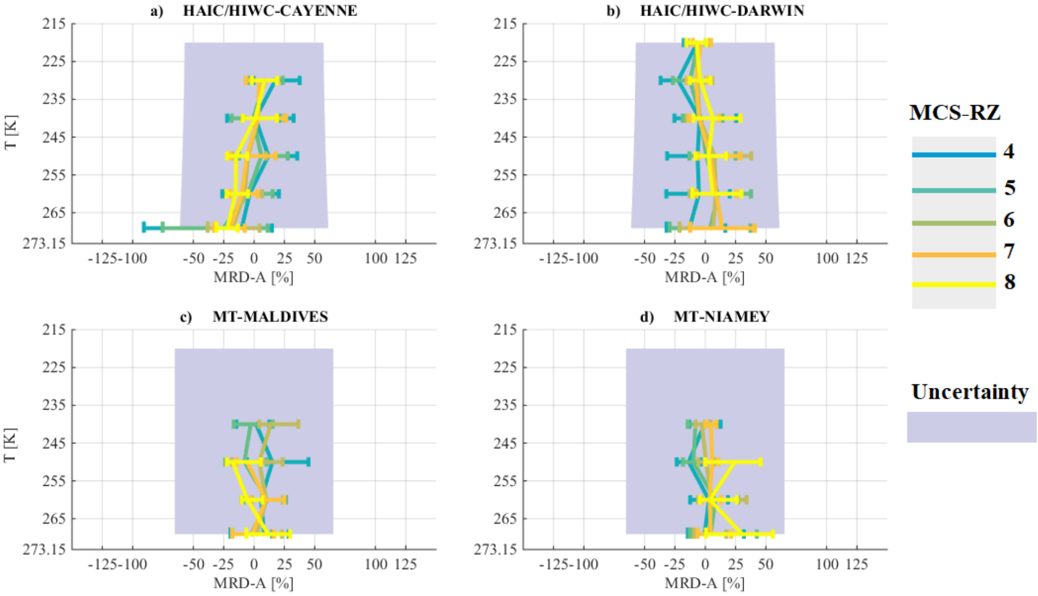

**Figure 26: Same as Figure 6, but for the ratio MRD-A.**

Hence, Field et al., (2007) proposed to retrieve the third moment $M_3$ as function of $M_2$ and T. These equations are recalled here with (in our case n=3):

$$M_n = M_2^{F(n)} \cdot D(n) \cdot exp(E(n) \cdot T_c) \tag{13}$$

$T_C$ denotes temperature in °C and D(n), E(n) and F(n) are given by:

$$D(n) = exp(13.6 - 7.76 \cdot n + 0.479 \cdot n^2) \tag{14}$$

$$E(n) = -0.0361 + 0.0151 \cdot n + 0.00149 \cdot n^2 \tag{15}$$

$$F(n) = 0.807 + 0.00581 \cdot n + 0.0457 \cdot n^2 \tag{16}$$

Figure 27 provides median relative errors (whiskers represent 25th and 75th percentiles) of parametrized moments $M_2$ (Figure 27 (a) and Figure 27 (b)) and $M_3$ (Figure 27 (c) and Figure 27 (d)) compared to respective moments calculated directly (Eq. (9) from PSD measurements (merged dataset). These relative errors are shown as a function of IWC (Figure 27(a) and Figure 27(c)) and as a function of T (Figure 27(b) and Figure 27(d)). Firstly, the red line shows median relative error of $M_2$ retrieved from Eq. (12) compared to $M_2$ derived from measured PSD (Eq. 9). In addition the grey band illustrates the uncertainty $U(M_2)/M_2$. Figure 27 (a) illustrates that below 2g $m^{-3}$, the median of this relative error is close to 0% with 25th and 75th percentiles significantly smaller than $U(M_2)/M_2$. However, for largest IWC beyond 2g $m^{-3}$, median relative errors are getting large (40% for 4g $m^{-3}$ and 75% for 4.5g $m^{-3}$) and need to be corrected in order to reduce the bias between predicted $M_2$ and observed $M_2$. This is why Eq. (11) is modified with an expression shown in Eq. (17) in order to improve prediction of $M_2$ compared to measured $M_2$ (Eq. (10)) for highest IWC:

$$M_2 = \frac{IWC}{A(T)} \cdot exp\big(0.005853 \cdot exp(1025 \cdot IWC)\big) \qquad [m^{-1}] \tag{17}$$

The effect of the expression added in Eq. (17) is illustrated by the blue line in Figure 27 (a) and Figure 27 (b), where median relative error of predicted $M_2$ are now closer to 0% also for large IWC. Note that in Figure 27 (b), median relative errors of the two above parametrizations (red and blue solid line) of $M_2$ are superposed as a function of T with a median relative error close to 0%. This means that the second part of equation (17) does not introduce any significant bias as a function of T, since the occurrence of IWC > 2g $m^{-3}$ is smaller than 1% for the merged dataset.

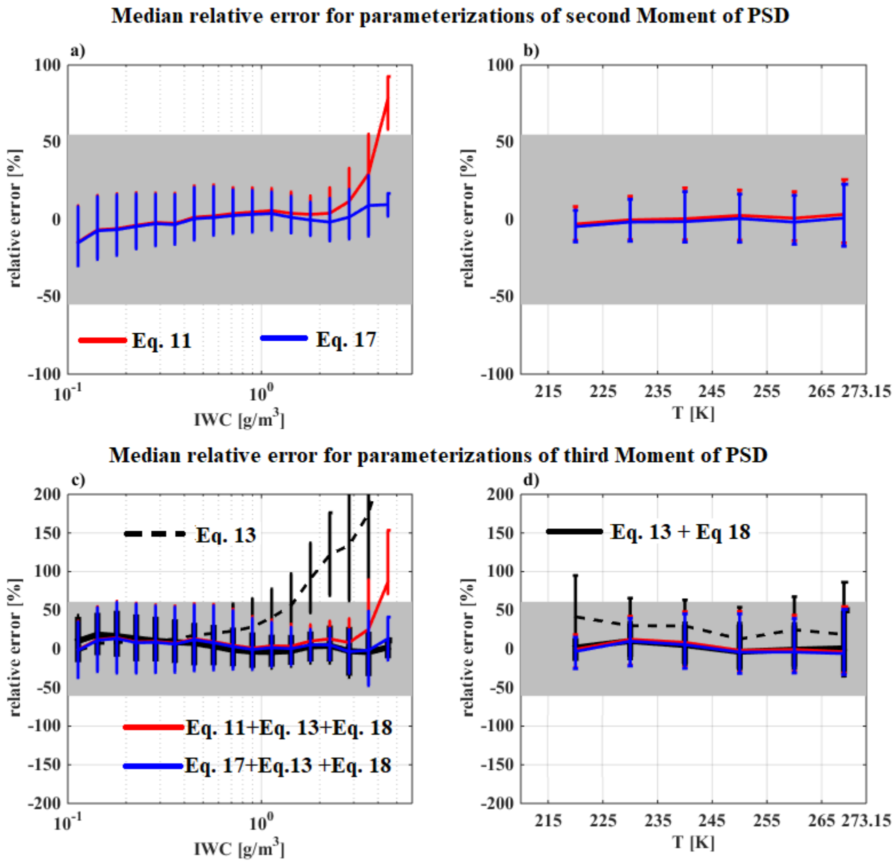

**Figure 27: Relative error of parametrized $M_2$ and $M_3$ for merged dataset as a function of IWC in a) and c), and as a function of T in b) and d). Solid lines give median relative error and whiskers denote 25th and 75th percentiles of relative error. Grey bands shows measurement uncertainties for $M_2$ (55%; a) and b)) and $M_3$ (61%; c) and d)), respectively.**

In Figure 27 (c) and Figure 27 (d)) are shown median relative error for parameterizations of the third moment, where the median relative error for all parameterization are calculated as function of measured $M_3$. First, we discuss the median relative error for parametrization of 3rd moment $M_3$ according to Field et al., (2007) (Eq. (13); black dashed lines) using the measured $M_2$. Hence, we can see that the parameterization of Field et al., (2007) overestimate $M_3$ for IWC larger than 1g.m$^{-3}$ and this overestimation of $M_3$ increase with IWC. Moreover, this overestimation of $M_3$ tend to decrease a bit as function of T.

To reduce this significant median relative error on measured $M_3$, particularly for large IWC in deep convective cloud systems, we provide a $M_3$ correction function for Eq. (13) as function of T and IWC:

$$M_3 = [-5.605 - 1.059 \cdot log(IWC) + 0.009536 \cdot T - 0.0418 \cdot log(IWC)^2 + 0.0007889 \cdot log(IWC) \cdot T] \cdot M_2^{F(3)} \cdot D(3) \cdot exp(E(3) \cdot T_c) \qquad (18)$$

Then we discuss the three series of median relative error of $M_3$ where $M_3$ are computed with Eq. (18). First, Eq. (18) is used with measured $M_2$ (black solid lines) to show the efficiency of the correction applied as function of IWC and T and described in Eq. (18). Then, Eq. (18) is applied to $M_2$ calculated using Eq. (11) where there is no correction as function of IWC to calculate $M_2$ (red solid lines). We observe that M3 are overestimated for IWC larger than 3g.m$^{-3}$ and that there is no bias as function of T with median relative error close to 0%. Finally, Eq. (18) is used to compute $M_3$ from $M_2$ calculated with Eq. (17) when impact of large IWC is taken into account. We can see median relative error close to 0% for the third example of parameterization (i.e. Eq. (17) and Eq. (18)) with no bias as function of IWC and T.

An identical investigation on median relative errors in the prediction of 2nd and 3rd moment as presented in Figure 27 has been investigated for individual MCS locations (figures not shown). For all type of tropical MCS, we observe that $M_2$ from Eq. (17) and $M_3$ from Eq. (18) tend to have smaller to equal median relative errors compared to the relative uncertainties $U(M_2)/M_2$ and $U(M_3)/M_3$, respectively. Beyond this general statement there are two noticeable observations. The first observation is that median relative errors of $M_3$ from Eq. (18) calculated either with $M_2$ from measurements (Eq. (9)) or from parametrized $M_2$

from Eq. (17) for MCS over Maldives Islands are close to U($M_3$)/$M_3$ with 75th percentiles reaching 100% for IWC in the range [0.3; 0.6] g $m^{-3}$. The second observation is that for MCS over Niamey, $M_3$ from Eq. (18) with $M_2$ from Eq. (9) or from Eq. (17) tend to overestimate respective moments calculated directly from PSD measurements by about 30 or 50%, respectively, in the area of higher IWC ([2; 3] g $m^{-3}$).

This section aims to produce parameterizations of the second and third moments of ice hydrometeor size distributions, which can be useful for the calculation of hydrometeor size distributions in numerical weather prediction using gamma distributions, but also (see the next section) for calculating rescaled ice hydrometeors size distributions (Field et al., 2007).

### 6.2.3 Rescaling of measured ice hydrometeors size distributions

From bulk properties as mixing ratio and total concentration in numerical weather prediction (NWP), ice hydrometeors size distributions (or PSD) properties can be derived from moment parameterization allowing simplified prediction of cloud microphysical processes such as precipitation. Usually, ice hydrometeors size distributions for hydrometeors are modeled by gamma distributions (Heymsfield et al., 2013; McFarquhar et al., 2007). Since the method of gamma distributions is relatively well documented, we focus this study on another type of PSD parameterization, which studies ‘rescaled PSD’ dealing with a ‘mean diameter’ defined by the ratio of the third moment over the second moment.

In this section, we propose an update for the method proposed by Field et al., (2007) for deep convective cloud systems and IWC larger than 0.1g $m^{-3}$. For the entire dataset of this study we therefore apply the method using Eq. (19) and Eq. (20) to calculate function $\Phi_{2,3}(x)$ and $x$ for individual measured PSD :

$$\Phi_{2,3}(x) = N(D_{max}) \cdot \frac{M_3^3}{M_2^4} \tag{19}$$

With $x$ being the characteristic size:

$$x = D_{max} \cdot \frac{M_2}{M_3} = \frac{D_{max}}{L_{2,3}} \tag{20}$$

$\Phi_{2,3}(x)$ and $x$ are dimensionless functions. Moreover, Field et al., (2007) deduced from their dataset, $\Phi_{2,3}(x)$ depending on cloud location; i.e. tropical troposphere or mid-latitude troposphere (here we focus on the equation established for the tropics):

$$Tropics\text{:}\ \Phi_{2,3}(x) = 152 \cdot exp(-12.4 \cdot x) + 3.28 \cdot x^{-0.78} \cdot exp(-1.94 \cdot x) \tag{21}$$

Hence, the variability of PSD in clouds, is not given by $\Phi_{2,3}(x)$, but by the variability of the 2nd and 3rd moments that allow retrieving functions $x$ and$\Phi_{2,3}(x)$. Then, knowing$x$,$\Phi_{2,3}(x)$, $M_2$, and $M_3$ concentrations of ice hydrometeors can be parameterized such:

$$D_{max} = x \cdot \frac{M_3}{M_2} \tag{22}$$

and

$$N(D_{max}) = \Phi_{2,3}(x) \cdot \frac{M_2^4}{M_3^3} \tag{23}$$

Figure 28 shows the probability distribution function (PDF) of observed rescaled PSD in tropical MCS as a function of the $x$ parameter. Thick black line represents $\Phi_{2,3}(x)$ from Field et al., (2007), thin dashed grey line represents median of $\Phi_{2,3}(x)$ for a given range of x, with whiskers showing 25th and 75th percentiles of $\Phi_{2,3}(x)$. The figure illustrates that Eq. (21) from Field et al., (2007) represents rather well $\Phi_{2,3}(x)$ as a function of $x$ in highest PDF region (light yellow area) and fits well the median plot for $x \in [0.3; 6]$. However, Field et al., (2007) performed their study for diameter larger than 100µm while this study calculates rescaled PSD for $D_{max}$ larger than 15µm for the underlying dataset. Thus, Eq. (21) does not fit median $\Phi_{2,3}(x)$ for $x$ smaller than 0.3. Also for $x > 6$, Eq. (21) decreases too fast compared to the median of $\Phi_{2,3}(x)$ calculated for the global tropical dataset of this study, although Field et al., (2007) considered ice hydrometeors up to 2cm, whilst this study extrapolates PSD until 1.2845cm only (reconstruction of partial images to calculate particle size according to Korolev and Sussman 2000).

A likely assumption to explain the differences for large $x > 6$ might be that the merged dataset of this study may have measured PSD with largest hydrometeors at a far higher frequency than this was the case for the dataset of Field et al., (2007).

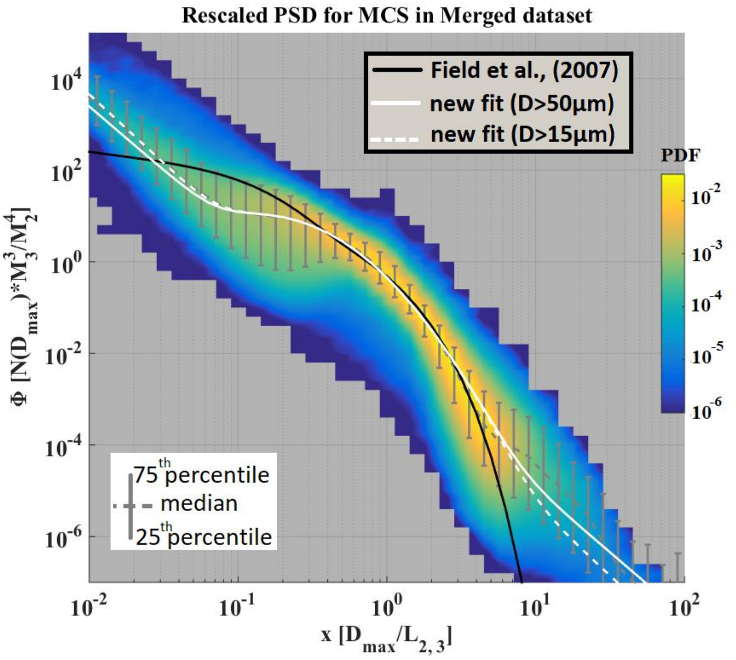

**Figure 28: Probability distribution function of rescaled PSD ($\Phi_{2,3}$) on y axis as a function of hydrometeor characteristics size (x) on x axis, for the merged datasets. Black lines show fitted functions from Field et al., (2007), grey dotted lines show median rescaled PSD with error bar from 25th and 75th percentiles of rescaled PSD. Solid white line presents the new fitted function for the merged dataset for PSD beyond 55µm and dashed white line shows fitted function for PSD beyond 15µm (Eq. 24).**

White lines (dashed and solid) show new fitted $\Phi_{2,3}(x)$ for the merged dataset of this study. The white dashed and solid lines can be represented by the following equation and aim to fit the median ($\Phi_{2,3}(x)$) of Figure 28 as a function of $x$:

$$Tropics: \Phi_{2,3}(x) = [exp(a_1) \cdot x^{a_2}] + \left[b_1 \cdot exp\left(-\frac{(ln(x) - b_2)^2}{b_3^2}\right)\right] \tag{24}$$

Where b1 = 9.484, b2 = -1.895 and b3 = 1.083. Note that dashed and solid white lines use different sets of coefficients $a_1$ and $a_2$ (Table 1). For white dashed line, $a_1$ and $a_2$ are calculated for $D_{max}$ beyond 15µm, whereas for white solid line, $a_1$ and $a_2$ are calculated for $D_{max}$ beyond 55µm. We can notice that the function for $D_{max} \geq 15$µm produces higher $\Phi_{2,3}(x)$ as compared to the function fitted for $D_{max} \geq 55$µm. In order to explain this difference, we recall that for MCSs over the Maldives Island concentrations of hydrometeors with $D_{max} \leq 55$µm are higher compared to 3 other tropical MCS locations, which could affect the fitted coefficients $a_1$ and $a_2$ in the two different versions of $\Phi_{2,3}(x)$ calculations for the merged dataset. Another difference in small particle measurements could be a pure technical difference in small particle measurements (including shattering/out-of-focus/small sample volume artefacts) between 2D-S probe (this study) and 2D-C probe (Field et al. (2007) study).

**Table 1 : Coefficients a1 and a2 for Eq. (24).**

| | $a_1$ | $a_2$ |
|---|---|---|
| Tropics: $D_{max}$ >15µm | -5.4114 | -3.0026 |
| Tropics: $D_{max}$ > 55µm | -5.0032 | -2.7822 |

The parameterization developed in this study is performed on ice hydrometeors distributions defined as function of $D_{max}$. However, NWP usually assumes that ice hydrometeors are spherical. So, Appendices E explores the impact of assuming that ice hydrometeors are spherical in the context of this study, noting that volumes of ice hydrometeors recorded by OAP are not directly measured. This latter short study is performed supposing that the truth to define ice hydrometeors distribution might be around using $D_{max}$ or spherical diameter. For both assumptions there is a need to perform sensitivity studies to assess which parameterization is more suited for NWP.

## 6 Discussion and conclusion

In this study we analyze in-situ aircraft observations of ice hydrometeor images and simultaneous cloud radar observations collected in tropical MCS in order to characterize the statistical properties of ice microphysics. The results are focused on the tropical MCS that include observations from: (i) the raining season over Cayenne (South America), (ii) the North-Australian monsoon over Darwin, (iii) deep convective systems over the Maldives Island in the ITCZ, and (iv) the West-African monsoon over Niamey.

The overall data analysis of ice hydrometeor properties has been performed as a function of temperature and the range of radar reflectivity factors measured at 94GHz. Therefore, all vertical profiles of aircraft onboard radar reflectivity measurements have been gathered and statistically analyzed in order to define delimited radar reflectivity zones, thereby reducing possible vertical bias due to the chosen flight track/altitude in the MCS systems. Hence, this study defines 8 MCS reflectivity zones that have been determined from radar reflectivity factor percentiles (1st 10th 30th 50th 70th 90th and 99th) as a function of temperature, thereby merging all vertical reflectivity profiles of the entire merged dataset used for this study. Analysis of the retrieved vertical wind speeds in each MCS reflectivity zone reveals that the probability to observe a magnitude of vertical winds larger than 1m.s$^{-1}$ are similar in MCS reflectivity zones 1 to 5, but then strongly increase from MCS reflectivity zone 6 to 8. Generally, these probabilities increase with decreasing temperature for all MCS reflectivity zones. Also, the simple magnitude of vertical wind speeds is larger in MCS reflectivity zones 7 and 8, while in MCS reflectivity zones 1 to 6 the magnitude is rather small and similar, however the magnitude is a function of T. Our investigation do not allow to link directly MCS reflectivity zones and the stage of life cycle of MCS (i.e. Formation, maturation, decaying). But, the analysis of geostationary satellites data would be more suited for this topic (Fiolleau and Roca 2013). Then, studying the distribution of MCS reflectivity zones as function of life cycle of MCS and brightness temperature and/or visible reflectance could help to answer to this question.

However, this study demonstrates that MCS reflectivity zones 7 and 8 exhibit highest probability to be related to the active convective zone and/or the most turbulent transition zone between the inaccessible part of the convective core and the stratiform part of MCS clouds. Whereas MCS reflectivity zones 1 to 5 are rather associated with the so-called stratiform parts of MCS. MCS reflectivity zone 6 then represents the transition between stratiform and convective area of an MCS with a relatively small median magnitude of vertical winds, however with relatively high probability of vertical wind magnitudes beyond 1m.s$^{-1}$.

Subsequently, the study compares microphysical properties (such as ice water content, extinction, concentrations, largest hydrometeor sizes, etc…) as a function of MCS reflectivity zone and temperature. The statistical analysis (median values, 25th and 75th percentiles) is performed for the individual MCS locations, whereas the merged dataset of the 4 tropical MCS locations serves as a reference. Relative differences of median microphysical properties in one MCS location compared to respective median properties of the reference dataset were quantified. Also uncertainties for all type of microphysical measurements and retrieved cloud parameters were calculated from Baumgardner et al. (2017).

Within the range of uncertainties, we showed that the variability of IWC, $\sigma$, $N_{T,50}$, $N_{T,500}$, $M_2$ and $M_3$ as a function of temperature and specific MCS reflectivity zones tends to be similar. For example, for IWC these conclusions apply for MCS reflectivity zones 4 to 8. MCS data from Niamey flight campaign (compared to the three other tropical MCS locations) reveal more exceptions when compared with median parameters calculated for the global tropical dataset, with a trend of larger 3rd PSD moments and larger hydrometeor sizes in the stratiform area of MCS. Assuming that largest hydrometeors ($max(D_{max})$) can be considered as a proxy for the aggregation process efficiency, findings of this study reveal that aggregation process efficiency is higher for MCS over land than over islands and higher over islands close to large land masses than over islands in the middle of an ocean. It seems to confirm the results of Frey et al., (2011) and Cetrone and Houze (2009).

From the tropical dataset a parametrization of visible extinction is developed as a function of temperature and IWC (Eq. 8). This model allows retrieving $\sigma$ from OAP measurements with an accuracy smaller than the measurement uncertainty of $\sigma$

($U(\sigma)/\sigma$ = 57%; Eq. (2)) for all four types of tropical MCS. Eq. (8) reveals best accuracy to represent directly calculated $\sigma$ in MCS over Darwin and Niamey.

Also in this study the relationship between mass and size of ice hydrometeors ($m=\alpha.D^{\beta}$) is formulated with a classical power law approximation. A basic finding is that the variability of retrieved $\beta$ throughout all MCS reflectivity zones is too large compared to its uncertainty. This would mean for example that varying $\beta$ parameterization in NWP is not worthy to do. Indeed, NWP schemes are used to describe ice microphysics with PSD moments (here $M_2$ and $M_3$). Setting $\beta$=2 for the mass-size relationship allows to link IWC to the second moment directly as stated in Field et al., (2007).

Defining $A$ as the ratio $IWC/M_2$, this study illustrates that $A$ increases with temperature. Also $A$ in MCS reflectivity zones 5, 6 and 7 are similar to the median $A$ calculated for the entire dataset (Figure 16(a)). In MCS reflectivity zone 4 (smaller zones were not considered) $A$ tends to be smaller and in MCS reflectivity zone 8, $A$ tends to be larger than the median of $A$ for the merged dataset. However, MCS reflectivity zones 4 and 8 share a wide range of variability with MCS reflectivity zones 5, 6 and 7. Hence, we use the variability of $A$ as a function of temperature (parametrization in Eq. (12)) to predict the 2nd PSD moment in tropical MCS. Whereas Eq. (11) retrieves $M_2$ in all type of MCS with a good accuracy, a correction is needed for high IWC (Eq. 17).

Hence, in this study the model of PSD moments presented by Field et al., (2007), has been considerably modified for PSD in deep convective clouds systems in order to predict the 3rd moment ($M_3$) from the known 2nd moment ($M_2$), IWC, and temperature $T$. This new parametrization of $M_3$ for deep convective clouds systems and IWC larger than 0.1 g m$^{-3}$ is given by Eq. (12), Eq. (17) and Eq. (18). The prediction of $M_2$ (Eq. 17) is more accurate than the prediction of $M_3$ (Eq. 18), when compared with $M_2$ and $M_3$ directly calculated from the measured PSD. Indeed, the predicted $M_2$ have median relative errors in the range [-25%; 25%] (corresponds to 25th and 75th percentiles of relative error of $M_2$) with an uncertainty of measured $M_2$ of about 55%. The predicted $M_3$ have median relative errors in the range [-40%; 55%] (which corresponds to 25th and 75th percentiles of relative error of $M_3$) with an uncertainty of measured $M_3$ of 61%. Note, that the use of this parameterization might lead to underestimate the third moments of PSD in NWP of the stratiform part of West African monsoon's MCS.

Furthermore, we applied on the 4 tropical datasets the method of Field et al., (2007) of PSD rescaling with 2nd and 3rd moments of the measured PSD.

Field et al., (2007) gave for their dataset a parametrized function $\Phi_{2,3}$ that models rescaled PSD in the tropics as a function of the mean diameter (ratio between the 3rd moment and the 2nd moment of the PSD). The calculated rescaled PSD for the 4 tropical datasets are in good agreement with $\Phi_{2,3}$ parametrization given by Field et al., (2007) from diameters between 0.3-6 times the mean diameter (dimensionless characteristic size $x$). Below, 0.3 times the mean diameter, $\Phi_{2,3}$ of Field et al., (2007) tend to overestimate the rescaled PSD and finally underestimate them again below 0.03 times the mean diameter. These differences can be explained because of different diameter threshold to calculate the rescaled PSD. In our study, we calculate rescaled PSD starting at 15µm (or 50µm; see table 1 and Eq. (24)) while Field et al., (2007) used PSD only beyond 100µm. Also for large mean diameters we note significant differences between the rescaled PSD for the dataset of this study and $\Phi_{2,3}$ parametrization from Field et al., (2007). Indeed, for diameters larger than 6 times the mean diameter, $\Phi_{2,3}$ of Field et al., (2007) decreases rapidly and therefore underestimates the rescaled PSD by about 1 order of magnitude at diameters equal to 10 times the mean diameter. We do not think that these differences are due to the difference in the cut-off diameter of PSD (last available diameter for PSD) which has been 20000µm in Field et al., (2007) against 12845µm in this study. Field et al., (2007) used PSD of ice hydrometeors measured in anvils and cirrus clouds while the entire dataset for this study has been gathered closest to MCS stratiform and convective zones of deep convective systems.

This latter fact more likely explains differences between the rescaled PSD of this study and parametrized $\Phi_{2,3}$ from Field et al., (2007). Probably, the underlying dataset for this study contains more large hydrometeors in non-negligible concentrations, and related increased statistics on large hydrometeor concentrations.

The parametrization based on tropical PSD data beyond 15µm seems to degrade parametrization results for largest diameters (rescaled concentrations beyond parametrization). We suspect that this is due to very high concentrations of small hydrometeors in the range 15-55µm in MCS over Maldives Islands, which would finally suggest to recommend parametrization for tropical MCS solely based on PSD beyond 50µm, in order to retrieve ice properties in deep convective clouds that could serve in NWP.

To conclude on the parameterization of ice hydrometeors distribution. We performed an update of the computation of PSD as function of IWC and T performed by Field et al., 2007 for tropical convective clouds (see Eq. (11), Eq. (17) and Eq. (18)). This parameterization was used in the microphysical scheme based on (Wilson and Ballard, 1999) used in the configuration of the Met Office Global Atmosphere version 6.1 (Walters et al., 2017). Which was the version of the Unified Model used operationally by the Met Office for global weather and climate prediction. More precisely, the ice-snow concentrations was computed with the moment parameterization developed by (Field et al., 2007) and the mass-diameter relationship from Cotton et al., (2013). Here, we suggest to use the new parameterization developed in our study for ice-snow concentrations when IWC are larger than 0.1 g.m$^{-3}$. Otherwise, we suggest to keep either the original version of Field et al., (2007) parameterization with the Cotton et al., (2013) mass size relationship. Or use the original version of Field et al., (2007) parameterization with A as function of temperature which would be a fit of the 25th percentile of A in MCS reflectivity zone 4 (see Table C12 in Appendices C).

We showed that IWC tend to be similar as function of temperature and MCS reflectivity zone, suggesting that IWC-Z-T relationship developed by Protat et al., (2016) would be applicable for IWC larger than 0.1g.m-3 in tropical MCS. In other words there is a confident relationship between IWC, Z and T in tropical MCS. Then, for the evaluation of NWP, we suggest to define the MCS reflectivity zones using the 25th percentiles of IWC as the lower limit of each MCS reflectivity zones (see Table C2 in Appendices C). Hence, for each MCS reflectivity zone visible extinction, hydrometeors concentrations ($NT_{50}$, $NT_{500}$, $M_2$ and $M_3$), reflectivity factors at 94GHz and vertical velocities from NWP can be compared with the findings of this study (see Table in Appendices C). This methodology should help to identify where NWP fails to represent the links between different parameters and IWC. Indeed, study the spatiotemporal variability of IWC in MCS is a complex topic. It needs a time reference and a space reference. For MCS, the time reference can be its life cycle, but there are MCS that have a more complex life cycle than others (merging of MCS, a new growing stage after a decaying stage). Concerning the space reference, there is a common view which is to observe the MCS from its most active area; its convective part. There are two difficulties to take into account here. First, there are very few direct measurement of cloud microphysic in the very convective area of MCS. Second, MCS can be the aggregation of many convective cells that can be well or not well organized (Houze 2004). Moreover, we saw that large IWC tend to be more associated to vertical movement than lower IWC, but it is not always true.

To test NWP of extreme weather events such MCS, we suggest using the statistic performed in this study, by testing the different conditions of others microphysical parameters observed for a given IWC and temperature.

Finally, several findings from this study suggest more investigations on the variability on the relationship between projected surface and mass of ice hydrometeors encountered in underlying observations. Indeed, we find that ice "density" is similar as a function of *T* and *Z* reflectivity ranges in all 4 MCS locations. Hence, this is referring to the possibility to investigate a surface-mass relationship in MCS that should be a function of *T* and *Z (IWC)*. Estimating that aerosol loads and corresponding CCN and IN properties may be more or less different in these four locations (continental aerosol over Africa with a strong influence of dust from Sahara, more cleaner troposphere over the Indian ocean, merging of continental and oceanic influences), we stipulate the need of investigating secondary ice production processes, that seem to regulate the concentrations of ice hydrometeors beyond 55µm.

## Author contribution

Emmanuel Fontaine, Julien Delanoë, Alfons Schwarzenboëck and Alain Protat for conceptualized this study. John Walter Strapp, Lyle Edward Lilie, Emmanuel Fontaine, Delphine Leroy, Julien Delanoë and Alain Protat for data curation of this study. John Walter Strapp, Lyle Edward Lilie, Delphine Leroy, Julien Delanoë and Emmanuel Fontaine to perform the formal analysis. Alain Protat and Fabien Dezitter for funding acquisition for campaign observations. Alfons Schwarzenboëck, Lyle Edward Lilie, John Walter Strapp, Alain Protat Delphine Leroy, Julien Delanoë and Emmanuel Fontaine for investigations performed in this study. Lyle Edward Lilie, Delphine Leroy, Julien Delanoë and Emmanuel Fontaine for developing methodology used in this study. John Walter Strapp, Fabien Dezitter and Alfons Schwarzenboëck for the project administration. Alfons Schwarzenboëck, John Walter Strapp and Julien Delanoë for providing resources. Lyle Edward Lilie, Delphine Leroy and Emmanuel Fontaine for the development of software used in this study. Alfons Schwarzenboëck for the supervision of this study. Emmanuel Fontaine to provide visualization.

Emmanuel Fontaine for writing original draft. Alfons Schwarzenboëck, Alain Protat, John Walter Strapp, Fabien Dezitter and Julien Delanoë for writing review and editing.

## Data availability

The HAIC-HIWC dataset that has been used within this study is shared within the European and North American HAIC/HIWC community for analysis and completion of aircraft industry/rulemaking and science objectives. A data sharing protocol has to be agreed upon and signed by all the parties. This means that post-processed data will be available to public not before January 2021. Therefore we cannot reply positively to demands, since rulemaking is actually ongoing within FAA and EASA aviation safety agencies, thereby processing the HAIC/HIWC data set. Concerning the dataset for the campaigns of observations of the Megha-Tropiques project: optical array probes data are available by contacting Alfons Schwarzenboëck and radar data are available by contacting Julien Delanoë.

## Acknowledgements

The authors are grateful to Centre National d'Etude Spatiale (CNES) for funding the aircraft measurement campaigns within the Megha-Tropiques project. The data were collected using instruments from the French Airborne Measurement Platform, a facility partially funded by CNRS/INSU and CNES. The research leading to these results (HAIC-HIWC project) has received funding from (i) the European Union's Seventh Framework Program in research, technological development and demonstration under grant agreement no. ACP2-GA-2012-314314, (ii) the European Aviation Safety Agency (EASA) Research Program under service contract no. EASA.2013.FC27, and (iii) the Federal Aviation Administration (FAA), Aviation Research Division, and Aviation Weather Division, under agreement CON-I-1301 with the Centre National de la Recherche Scientifique. Funding to support flight project was also provided by the NASA Aviation Safety Program, the Boeing Co., and Transport Canada. Additional support was also provided by Airbus SAS Operations, Science Engineering Associates, the Bureau of Meteorology, Environment Canada, the National Research Council of Canada, and the universities of Utah and Illinois. The authors thank the SAFIRE facility for the scientific airborne operations. SAFIRE (http://www.safire.fr) is a joint facility of CNRS, Météo-France, and CNES dedicated to flying research aircraft.

The authors thank Dr. Frey and Dr. Baumgardner to review and help to improve this publication.

## References

Bailey, M.P., Hallett, J.: A Comprehensive Habit Diagram for Atmospheric Ice Crystals: Confirmation from the Laboratory, AIRS II, and Other Field Studies. J. Atmos. Sci. 66, 2888–2899. https://doi.org/10.1175/2009JAS2883.1, 2009.

Baumgardner, D., Abel, S.J., Axisa, D., Cotton, R., Crosier, J., Field, P., Gurganus, C., Heymsfield, A., Korolev, A., Krämer, M., Lawson, P., McFarquhar, G., Ulanowski, Z., Um, J.: Cloud Ice Properties: In Situ Measurement Challenges. Meteorological Monographs 58, 9.1-9.23. https://doi.org/10.1175/AMSMONOGRAPHS-D-16-0011.1, 2017.

Baumgardner, D., Brenguier, J.L., Bucholtz, A., Coe, H., DeMott, P., Garrett, T.J., Gayet, J.F., Hermann, M., Heymsfield, A., Korolev, A., Krämer, M., Petzold, A., Strapp, W., Pilewskie, P., Taylor, J., Twohy, C., Wendisch, M., Bachalo, W., Chuang, P.: Airborne instruments to measure atmospheric aerosol particles, clouds and radiation: A cook's tour of mature and emerging technology. Atmospheric Research 102, 10–29. http://dx.doi.org/10.1016/j.atmosres.2011.06.021, 2011.

Baumgardner, D. and Rodi, A.: Laboratory and Wind Tunnel Evaluations of the Rosemount Icing Detector, J. Atmos. Oceanic Technol., 6(6), 971–979, doi:10.1175/1520-0426(1989)006<0971:LAWTEO>2.0.CO;2, 1989.

Brown, P.R.A., Francis, P.N., 1995. Improved Measurements of the Ice Water Content in Cirrus Using a Total-Water Probe. Journal of Atmospheric and Oceanic Technology 12, 410–414. https://doi.org/10.1175/1520-0426(1995)012<0410:IMOTIW>2.0.CO;2, 1995.

Cetrone, J., Houze, R.A.: Anvil clouds of tropical mesoscale convective systems in monsoon regions. Quarterly Journal of the Royal Meteorological Society 135, 305–317. https://doi.org/10.1002/qj.389, 2009

Claffey, K. J., Jones, K. F. and Ryerson, C. C.: Use and calibration of Rosemount ice detectors for meteorological research, Atmospheric Research, 36(3), 277–286, doi:10.1016/0169-8095(94)00042-C, 1995.

Cober, S. G., Isaac, G. A. and Korolev, A. V.: Assessing the Rosemount Icing Detector with In Situ Measurements, J. Atmos. Oceanic Technol., 18(4), 515–528, doi:10.1175/1520-0426(2001)018<0515:ATRIDW>2.0.CO;2, 2001.

Cotton, R.J., Field, P.R., Ulanowski, Z., Kaye, P.H., Hirst, E., Greenaway, R.S., Crawford, I., Crosier, J., Dorsey, J.: The effective density of small ice particles obtained from in situ aircraft observations of mid-latitude cirrus. Q.J.R. Meteorol. Soc. 139, 1923–1934. https://doi.org/10.1002/qj.2058, 2013.

Coutris, P., Leroy, D., Fontaine, E., Schwarzenboeck, A.: An Inverse Problem approach for the retrieval of ice particle mass from in-situ measurements. J. Atmos. Oceanic Technol. https://doi.org/10.1175/JTECH-D-17-0013.1, 2017

Davison, C. R., Strapp, J. W., Lilie, L., Ratvasky, T. P., and Dumont, C.: Isokinetic TWC Evaporator Probe: Calculations and Systemic Error Analysis, 2016, 8th AIAA Atmospheric and Space Environments Conference, Washington, DC. AIAA-4060. http://dx.doi.org/10.2514/6.2016-4060, June 17, 2016.

Davison, C. R., Landreville, C., and MacLeod, J. D.: Initial Development and Testing of Isokinetic Probe to Measure Total Water Content During Ground and Airborne Testing," NRC, LTR-GTL-2010-0002, Ottawa, Mar. 2010.

Field, P.R., Wood, R., Brown, P.R.A., Kaye, P.H., Hirst, E., Greenaway, R., Smith, J.A.: Ice Particle Interarrival Times Measured with a Fast FSSP. J. Atmos. Oceanic Technol. 20, 249–261. https://doi.org/10.1175/1520-0426(2003)020<0249:IPITMW>2.0.CO;2, 2003.

Delanoë, J., Protat, A., Bouniol, D., Heymsfield, A., Bansemer, A., Brown, P.: The Characterization of Ice Cloud Properties from Doppler Radar Measurements. J. Appl. Meteor. Climatol. 46, 1682–1698. https://doi.org/10.1175/JAM2543.1, 2007.

Delanoë, J.M.E., Heymsfield, A.J., Protat, A., Bansemer, A., Hogan, R.J.: Normalized particle size distribution for remote sensing application. Journal of Geophysical Research: Atmospheres 119, 4204–4227. https://doi.org/10.1002/2013JD020700, 2014.

Delrieu, G., Nicol, J., Yates, E., Kirstetter, P.-E., Creutin, J.-D., Anquetin, S., Obled, C., Saulnier, G.-M., Ducrocq, V., Gaume, E., Payrastre, O., Andrieu, H., Ayral, P.-A., Bouvier, C., Neppel, L., Livet, M., Lang, M., du-Châtelet, J.P., Walpersdorf, A., Wobrock, W.: The Catastrophic Flash-Flood Event of 8–9 September 2002 in the Gard Region, France: A First Case Study for the Cévennes–Vivarais Mediterranean Hydrometeorological Observatory. J. Hydrometeor 6, 34–52. https://doi.org/10.1175/JHM-400.1, 2005.

Drigeard, E., Fontaine, E., Wobrock, W., Schwarzenböck, A., Duroure, C., Williams, E.R., Russell, B., Protat, A., Delanoë, J., Cazenave, F., Gosset, M.: A Comparison of Airborne In Situ Cloud Microphysical Measurement with Ground-Based C-

Band Radar Observations in Deep Stratiform Regions of African Squall Lines. J. Appl. Meteor. Climatol. 54, 2461–2477. https://doi.org/10.1175/JAMC-D-14-0262.1, 2015.

Ducrocq, V., Braud, I., Davolio, S., Ferretti, R., Flamant, C., Jansa, A., Kalthoff, N., Richard, E., Taupier-Letage, I., Ayral, P.-A., Belamari, S., Berne, A., Borga, M., Boudevillain, B., Bock, O., Boichard, J.-L., Bouin, M.-N., Bousquet, O., Bouvier, C., Chiggiato, J., Cimini, D., Corsmeier, U., Coppola, L., Cocquerez, P., Defer, E., Delanoë, J., Di Girolamo, P., Doerenbecher, A., Drobinski, P., Dufournet, Y., Fourrié, N., Gourley, J.J., Labatut, L., Lambert, D., Le Coz, J., Marzano, F.S., Molinié, G., Montani, A., Nord, G., Nuret, M., Ramage, K., Rison, W., Roussot, O., Said, F., Schwarzenboeck, A., Testor, P., Van Baelen, J., Vincendon, B., Aran, M., Tamayo, J.: HyMeX-SOP1: The Field Campaign Dedicated to Heavy Precipitation and Flash Flooding in the Northwestern Mediterranean. Bull. Amer. Meteor. Soc. 95, 1083–1100. https://doi.org/10.1175/BAMS-D-12-00244.1, 2013.

Field, P.R., Lawson, R.P., Brown, P.R.A., Lloyd, G., Westbrook, C., Moisseev, D., Miltenberger, A., Nenes, A., Blyth, A., Choularton, T., Connolly, P., Buehl, J., Crosier, J., Cui, Z., Dearden, C., DeMott, P., Flossmann, A., Heymsfield, A., Huang, Y., Kalesse, H., Kanji, Z.A., Korolev, A., Kirchgaessner, A., Lasher-Trapp, S., Leisner, T., McFarquhar, G., Phillips, V., Stith, J., Sullivan, S.: Secondary Ice Production: Current State of the Science and Recommendations for the Future. Meteorological Monographs 58, 7.1-7.20. https://doi.org/10.1175/AMSMONOGRAPHS-D-16-0014.1, 2016.

Field, P. R., Heymsfield, A. J. and Bansemer, A.: Shattering and Particle Interarrival Times Measured by Optical Array Probes in Ice Clouds, J. Atmos. Oceanic Technol., 23(10), 1357–1371, doi:10.1175/JTECH1922.1, 2006.

Field, P.R., Wood, R., Brown, P.R.A., Kaye, P.H., Hirst, E., Greenaway, R., Smith, J.A.: Ice Particle Interarrival Times Measured with a Fast FSSP. J. Atmos. Oceanic Technol. 20, 249–261. https://doi.org/10.1175/1520-0426(2003)020<0249:IPITMW>2.0.CO;2, 2003.

Fiolleau, T., Roca, R.: An Algorithm for the Detection and Tracking of Tropical Mesoscale Convective Systems Using Infrared Images From Geostationary Satellite. Geoscience and Remote Sensing, IEEE Transactions on 51, 4302–4315. https://doi.org/10.1109/TGRS.2012.2227762, 2013.

Fontaine, E., Leroy, D., Schwarzenboeck, A., Delanoë, J., Protat, A., Dezitter, F., Grandin, A., Strapp, J.W., Lilie, L.E.: Evaluation of radar reflectivity factor simulations of ice crystal populations from in situ observations for the retrieval of condensed water content in tropical mesoscale convective systems. Atmos. Meas. Tech. 10, 2239–2252. https://doi.org/10.5194/amt-10-2239-2017, 2017.

Fontaine, E., Schwarzenboeck, A., Delanoë, J., Wobrock, W., Leroy, D., Dupuy, R., Gourbeyre, C., Protat, A.: Constraining mass diameter relations from hydrometeor images and cloud radar reflectivities in tropical continental and oceanic convective anvils. Atmospheric Chemistry and Physics 14, 11367–11392. https://doi.org/10.5194/acp-14-11367-2014, 2014.

Frey, W., Borrmann, S., Kunkel, D., Weigel, R., Reus, M. de, Schlager, H., Roiger, A., Voigt, C., Hoor, P., Curtius, J., Krämer, M., Schiller, C., Volk, C. M., Homan, C. D., Fierli, F., Donfrancesco, G. D., Ulanovsky, A., Ravegnani, F., Sitnikov, N. M., Viciani, S., D'Amato, F., Shur, G. N., Belyaev, G. V., Law, K. S. and Cairo, F.: In situ measurements of tropical cloud properties in the West African Monsoon: upper tropospheric ice clouds, Mesoscale Convective System outflow, and subvisual cirrus, Atmospheric Chemistry and Physics, 11(12), 5569–5590, doi:https://doi.org/10.5194/acp-11-5569-2011, 2011.

Gayet, J.-F., Mioche, G., Bugliaro, L., Protat, A., Minikin, A., Wirth, M., Dörnbrack, A., Shcherbakov, V., Mayer, B., Garnier, A., Gourbeyre, C.: On the observation of unusual high concentration of small chain-like aggregate ice crystals and large ice water contents near the top of a deep convective cloud during the CIRCLE-2 experiment. Atmos. Chem. Phys. 12, 727–744. https://doi.org/10.5194/acp-12-727-2012, 2012.

Heymsfield, A. J., Schmitt, C. and Bansemer, A.: Ice Cloud Particle Size Distributions and Pressure-Dependent Terminal Velocities from In Situ Observations at Temperatures from 0° to −86°C, J. Atmos. Sci., 70(12), 4123–4154, doi:10.1175/JAS-D-12-0124.1, 2013.

Heymsfield, A.J., Bansemer, A., Heymsfield, G., Fierro, A.O.: Microphysics of Maritime Tropical Convective Updrafts at Temperatures from −20° to −60°. Journal of the Atmospheric Sciences 66, 3530–3562. https://doi.org/10.1175/2009JAS3107.1, 2009.

Heymsfield, A.J., Schmitt, C., Bansemer, A., Twohy, C.H.: Improved Representation of Ice Particle Masses Based on Observations in Natural Clouds. Journal of the Atmospheric Sciences 67, 3303–3318. https://doi.org/10.1175/2010JAS3507.1, 2010.

Heymsfield, A.J., Schmitt, C., Bansemer, A., van Zadelhoff, G.-J., McGill, M.J., Twohy, C., Baumgardner, D.: Effective Radius of Ice Cloud Particle Populations Derived from Aircraft Probes. J. Atmos. Oceanic Technol. 23, 361–380. https://doi.org/10.1175/JTECH1857.1, 2006.

Hogan, R.J., Tian, L., Brown, P.R.A., Westbrook, C.D., Heymsfield, A.J., Eastment, J.D.: Radar Scattering from Ice Aggregates Using the Horizontally Aligned Oblate Spheroid Approximation. J. Appl. Meteor. Climatol. 51, 655–671. https://doi.org/10.1175/JAMC-D-11-074.1, 2011.

Houze, R.A.: Mesoscale convective systems. Reviews of Geophysics 42, n/a–n/a. https://doi.org/10.1029/2004RG000150, 2004.

Huffman, G.J., Bolvin, D.T., Nelkin, E.J., Wolff, D.B., Adler, R.F., Gu, G., Hong, Y., Bowman, K.P., Stocker, E.F.: The TRMM Multisatellite Precipitation Analysis (TMPA): Quasi-Global, Multiyear, Combined-Sensor Precipitation Estimates at Fine Scales. J. Hydrometeor 8, 38–55. https://doi.org/10.1175/JHM560.1, 2007.

Jensen, M.P., Ackerman, T.P., Sekelsky, S.M.: Radiative Impacts of Anvil Cloud during the Maritime Continent Thunderstorm Experiment. J. Appl. Meteor. 41, 473–487. https://doi.org/10.1175/1520-0450(2002)041<0473:RIOACD>2.0.CO;2, 2002.

Jensen, M.P., Del Genio, A.D.: Radiative and Microphysical Characteristics of Deep Convective Systems in the Tropical Western Pacific. Journal of Applied Meteorology 42, 1234–1254. https://doi.org/10.1175/1520-0450(2003)042<1234:RAMCOD>2.0.CO;2, 2003.

Korolev, A., Isaac, G.A.: Shattering during Sampling by OAPs and HVPS. Part I: Snow Particles. J. Atmos. Oceanic Technol. 22, 528–542. https://doi.org/10.1175/JTECH1720.1, 2005.

Korolev, A., Sussman, B.: A Technique for Habit Classification of Cloud Particles. Journal of Atmospheric and Oceanic Technology 17, 1048–1057. https://doi.org/10.1175/1520-0426(2000)017<1048:ATFHCO>2.0.CO;2, 2000.

Lawson, R.P., Jensen, E., Mitchell, D.L., Baker, B., Mo, Q., Pilson, B.: Microphysical and radiative properties of tropical clouds investigated in TC4 and NAMMA. Journal of Geophysical Research: Atmospheres 115, n/a–n/a. https://doi.org/10.1029/2009JD013017, 2010.

Lawson, R.P., O’Connor, D., Zmarzly, P., Weaver, K., Baker, B., Mo, Q., Jonsson, H.: The 2D-S (Stereo) Probe: Design and Preliminary Tests of a New Airborne, High-Speed, High-Resolution Particle Imaging Probe. J. Atmos. Oceanic Technol. 23, 1462–1477. https://doi.org/10.1175/JTECH1927.1, 2006.

Leroy, D., Fontaine, E., Schwarzenboeck, A., Strapp, J.W.: Ice Crystal Sizes in High Ice Water Content Clouds. Part 1: On the computation of Median Mass Diameter from in-situ measurements. Journal of Atmospheric and Oceanic Technology 0, null. https://doi.org/10.1175/JTECH-D-15-0151.1, 2016.

Leroy, D., Fontaine, E., Schwarzenboeck, A., Strapp, J. W., Korolev, A., McFarquhar, G., Dupuy, R., Gourbeyre, C., Lilie, L., Protat, A., Delanoe, J., Dezitter, F. and Grandin, A.: Ice Crystal Sizes in High Ice Water Content Clouds. Part II: Statistics of Mass Diameter Percentiles in Tropical Convection Observed during the HAIC/HIWC Project, Journal of Atmospheric and Oceanic Technology, 34(1), 117–136, doi:10.1175/JTECH-D-15-0246.1, 2017.

Li, J.-L., Jiang, J.H., Waliser, D.E., Tompkins, A.M.: Assessing consistency between EOS MLS and ECMWF analyzed and forecast estimates of cloud ice. Geophysical Research Letters 34, n/a–n/a. https://doi.org/10.1029/2006GL029022, 2007.

Li, J.-L., Waliser, D.E., Jiang, J.H., Wu, D.L., Read, W., Waters, J.W., Tompkins, A.M., Donner, L.J., Chern, J.-D., Tao, W.-K., Atlas, R., Gu, Y., Liou, K.N., Del Genio, A., Khairoutdinov, M., Gettelman, A.: Comparisons of EOS MLS cloud ice measurements with ECMWF analyses and GCM simulations: Initial results. Geophysical Research Letters 32, n/a–n/a. https://doi.org/10.1029/2005GL023788, 2005.

Locatelli, J.D., Hobbs, P.V.: Fall speeds and masses of solid precipitation particles. Journal of Geophysical Research 79, 2185–2197. https://doi.org/10.1029/JC079i015p02185, 1974.

Madden, R.A., Julian, P.R.: Observations of the 40–50-Day Tropical Oscillation—A Review. Mon. Wea. Rev. 122, 814–837. https://doi.org/10.1175/1520-0493(1994)122<0814:OOTDTO>2.0.CO;2, 1994.

Madden, R.A., Julian, P.R.: Detection of a 40–50 Day Oscillation in the Zonal Wind in the Tropical Pacific. J. Atmos. Sci. 28, 702–708. https://doi.org/10.1175/1520-0469(1971)028<0702:DOADOI>2.0.CO;2, 1971.

Magono, C., Lee, C., Woo.: Meteorological Classification of Natural Snow Crystals. Journal of the Faculty of Science, Hokkaido University 2(4): 321-335, 1966.

Martini, A., Viltard, N., Ellis, S.M., Fontaine, E.: Ice microphysics retrieval in the convective systems of the Indian Ocean during the CINDY–DYNAMO campaign. Atmospheric Research. http://dx.doi.org/10.1016/j.atmosres.2014.12.013, 2015.

McFarquhar, G. M., Timlin, M. S., Rauber, R. M., Jewett, B. F., Grim, J. A. and Jorgensen, D. P.: Vertical Variability of Cloud Hydrometeors in the Stratiform Region of Mesoscale Convective Systems and Bow Echoes, Monthly Weather Review, 135(10), 3405–3428, doi:10.1175/MWR3444.1, 2007.

Mitchell, D.L.: Use of Mass- and Area-Dimensional Power Laws for Determining Precipitation Particle Terminal Velocities. J. Atmos. Sci. 53, 1710–1723. https://doi.org/10.1175/1520-0469(1996)053<1710:UOMAAD>2.0.CO;2, 1996.

Phillips, V.T.J., Patade, S., Gutierrez, J., Bansemer,: A. Secondary ice production by fragmentation of freezing drops: formulation and theory. J. Atmos. Sci. https://doi.org/10.1175/JAS-D-17-0190.1, 2018.

Protat, A., Zawadzki, I.: A Variational Method for Real-Time Retrieval of Three-Dimensional Wind Field from Multiple-Doppler Bistatic Radar Network Data. J. Atmos. Oceanic Technol. 16, 432–449. https://doi.org/10.1175/1520-0426(1999)016<0432:AVMFRT>2.0.CO;2, 1999.

Protat, A., Bouniol, D., Delanoë, J., O'Connor, E., May, P.T., Plana-Fattori, A., Hasson, A., Görsdorf, U., Heymsfield, A.J.: Assessment of Cloudsat Reflectivity Measurements and Ice Cloud Properties Using Ground-Based and Airborne Cloud Radar Observations. J. Atmos. Oceanic Technol. 26, 1717–1741. https://doi.org/10.1175/2009JTECHA1246.1, 2009.

Protat, A., Delanoë, J., Strapp, J.W., Fontaine, E., Leroy, D., Schwarzenboeck, A., Lilie, L., Davison, C., Dezitter, F., Grandin, A., Weber, M.: The Measured Relationship between Ice Water Content and Cloud Radar Reflectivity in Tropical Convective Clouds. Journal of Applied Meteorology and Climatology 55, 1707–1729. https://doi.org/10.1175/JAMC-D-15-0248.1

Pruppacher, H.R., Klett, J.D., Wang, P.K., 1998. Microphysics of Clouds and Precipitation. Aerosol Science and Technology 28, 381–382. https://doi.org/10.1080/02786829808965531, 2016.

Roca, R., Brogniez, H., Chambon, P., Chomette, O., Cloché, S., Gosset, M.E., Mahfouf, J., Raberanto, P., Viltard, N.: The Megha-Tropiques mission: a review after three years in orbit. Frontiers in Earth Science 3. https://doi.org/10.3389/feart.2015.00017, 2015.

Schmitt, C.G., Heymsfield, A.J.: The Dimensional Characteristics of Ice Crystal Aggregates from Fractal Geometry. Journal of the Atmospheric Sciences 67, 1605–1616. https://doi.org/10.1175/2009JAS3187.1, 2010.

Smith, W.L.: 4-D Cloud Properties from Passive Satellite Data and Applications to Resolve the Flight Icing Threat to Aircraft. University Of Wisconsin-Madison. Ph.D thesis, 179pp., 2014.

Stephens, G.L., Vane, D.G., Boain, R.J., Mace, G.G., Sassen, K., Wang, Z., Illingworth, A.J., O'Connor, E.J., Rossow, W.B., Durden, S.L., Miller, S.D., Austin, R.T., Benedetti, A., Mitrescu, C., CloudSat Science Team, T.: THE CLOUDSAT MISSION AND THE A-TRAIN. Bull. Amer. Meteor. Soc. 83, 1771–1790. https://doi.org/10.1175/BAMS-83-12-1771, 2002.

Stith, J.L., Avallone, L.M., Bansemer, A., Basarab, B., Dorsi, S.W., Fuchs, B., Lawson, R.P., Rogers, D.C., Rutledge, S., Toohey, D.W.: Ice particles in the upper anvil regions of midlatitude continental thunderstorms: the case for frozen-drop aggregates. Atmospheric Chemistry and Physics 14, 1973–1985. https://doi.org/10.5194/acp-14-1973-2014, 2014.

Strapp, J.W., Lilie, L.E., Ratvasky, T.P., Davison, C.R., and C. Dumont.: Isokinetic TWC Evaporator Probe: Development of the IKP2 and Performance Testing for the HAIC-HIWC Darwin 2014 and Cayenne Field Campaigns, 8th AIAA Atmospheric and Space Environments Conference, AIAA Aviation, AIAA 2016-4059. http://dx.doi.org/10.2514/6.2016-4059, 2016a.

Strapp, J. W., G. A. Isaac. A. Korolev, T. Ratvasky, R. Potts, P. May, A. Protat, P. Minnis, A. Ackerman, A. Fridlind, J. Haggerty, and J. Riley.: The High Ice Water Content (HIWC) Study of deep convective clouds: Science and technical plan. FAA Rep. DOT/FAA/TC-14/31, available at http://www.tc.faa.gov/its/worldpac/techrpt/tc14-31.pdf. 105 pp., 2016b

Strauss, C., Ricard, D., Lac, C. and Verrelle, A.: Evaluation of turbulence parametrizations in convective clouds and their environment based on a large-eddy simulation, Quarterly Journal of the Royal Meteorological Society, 0(0), doi:10.1002/qj.3614, n.d.

Yano, J.-I., Phillips, V.T.J.: Ice–Ice Collisions: An Ice Multiplication Process in Atmospheric Clouds. J. Atmos. Sci. 68, 322–333. https://doi.org/10.1175/2010JAS3607.1, 2011.

Van de Hulst, H.C.: Light scattering by small particles, 470 pp, Dover, Mineola, N.Y., 1981.

Yost, C.R., Bedka, K.M., Minnis, P., Nguyen, L., Strapp, J.W., Palikonda, R., Khlopenkov, K., Spangenberg, D., Smith Jr., W.L., Protat, A., Delanoe, J.: A prototype method for diagnosing high ice water content probability using satellite imager data. Atmos. Meas. Tech. 11, 1615–1637. https://doi.org/10.5194/amt-11-1615-2018, 2018.

Walters, D., Boutle, I., Brooks, M., Melvin, T., Stratton, R., Vosper, S., Wells, H., Williams, K., Wood, N., Allen, T., Bushell, A., Copsey, D., Earnshaw, P., Edwards, J., Gross, M., Hardiman, S., Harris, C., Heming, J., Klingaman, N., Levine, R., Manners, J., Martin, G., Milton, S., Mittermaier, M., Morcrette, C., Riddick, T., Roberts, M., Sanchez, C., Selwood, P., Stirling, A., Smith, C., Suri, D., Tennant, W., Vidale, P. L., Wilkinson, J., Willett, M., Woolnough, S. and Xavier, P.: The Met Office Unified Model Global Atmosphere 6.0/6.1 and JULES Global Land 6.0/6.1 configurations, Geoscientific Model Development, 10(4), 1487–1520, doi:https://doi.org/10.5194/gmd-10-1487-2017, 2017.

Wilson, D. R. and Ballard, S. P.: A microphysically based precipitation scheme for the UK meteorological office unified model, Quarterly Journal of the Royal Meteorological Society, 125(557), 1607–1636, doi:10.1002/qj.49712555707, 1999.

Yost, C.R., Minnis, P., Ayers, J.K., Spangenberg, D.A., Heymsfield, A.J., Bansemer, A., McGill, M.J., Hlavka, D.L.: Comparison of GOES-retrieved and in situ measurements of deep convective anvil cloud microphysical properties during the Tropical Composition, Cloud and Climate Coupling Experiment (TC4). Journal of Geophysical Research: Atmospheres 115, n/a–n/a. https://doi.org/10.1029/2009JD013313, 2010.

## Appendices A: total concentrations for $D_{max}$ > 15 microns

Figure A1 shows median total concentration ($N_T$) as a function of T and MCS reflectivity zone for the merged datasets where concentrations of ice hydrometeors are integrating beyond 15µm:

$$N_T = \sum_{Dmax=15}^{Dmax=12845} N(D_{max}) \cdot \Delta D_{max} \qquad [L^{-1}] \tag{A1}$$

Median $N_T$ systematically increase with MCS reflectivity zone and altitude, however with significant overlap of 25th and 75th percentiles of neighboring MCS reflectivity zones. Measurement uncertainty on concentrations given for small hydrometeors is about ±100% (Baumgardner et al., 2017).

Figure A2 (a), Figure A2 (b), Figure A2 (c), and Figure A2 (d) show MRD-$N_T$ of MCS in the different tropical locations. For MCS over Darwin and Cayenne, in all MCS reflectivity zones MRD-$N_T$ are smaller than the measurement uncertainty, whereas for Niamey data this is the case only in MCS reflectivity zones 2, 5, 6 and 7. MCS over Maldives Islands yield significantly larger MRD-$N_T$ than the measurement uncertainty, and those are primarily positive. Hence, MCS over Maldives Islands have larger concentrations of hydrometeors for a same range of T and Z, than the three other types of tropical MCS. However, these larger concentrations observed do not concern zones where highest concentrations of hydrometeors were observed. For example, in MCS reflectivity zone 4 where MRD-$N_T$ is reaching 1000%, $N_T$ for the Maldives dataset are approximately 1000 $L^{-1}$, which is similar to $N_T$ observed in MCS reflectivity zones 7 and 8 for the same range of T ∈ [235K; 245K[ for the merged dataset. We recall that identical image data processing to remove shattering artefacts and to correct out of focus images (Field et al., 2003; Korolev and Isaac, 2005; Leroy et al., 2016) have been applied for all 4 tropical datasets. Also the presence of super cooled droplets has been investigated (RICE, CDP probe), and few periods with super cooled water content have been removed for this study. Moreover, we show in section 5.5 that MCSs over Maldives Islands tend to have smaller max($D_{max}$) especially in MCS reflectivity zones 4, 5, 6 and 7 compared to the other MCS locations and that concentrations beyond 500µm in Maldives Islands observations are in the same range as the other types of MCS.

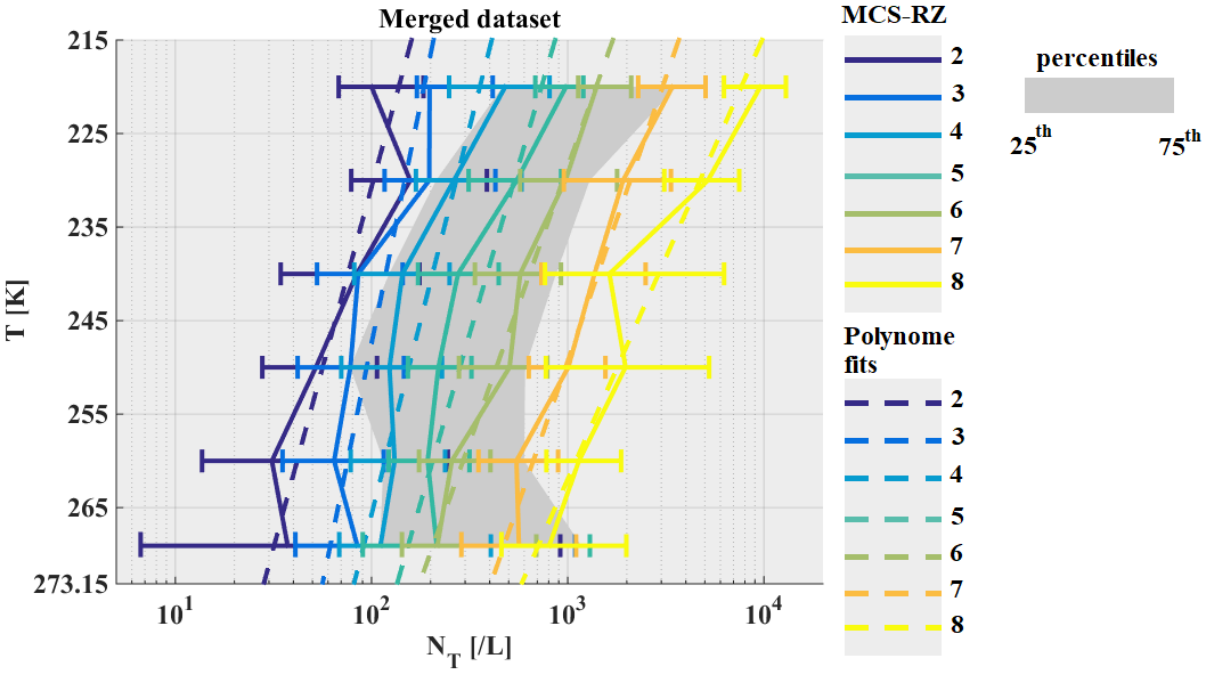

**Figure A1: Same as Figure 5, but for concentrations of hydrometeors integrated beyond $D_{max}$ =15µm in [$L^{-1}$].**

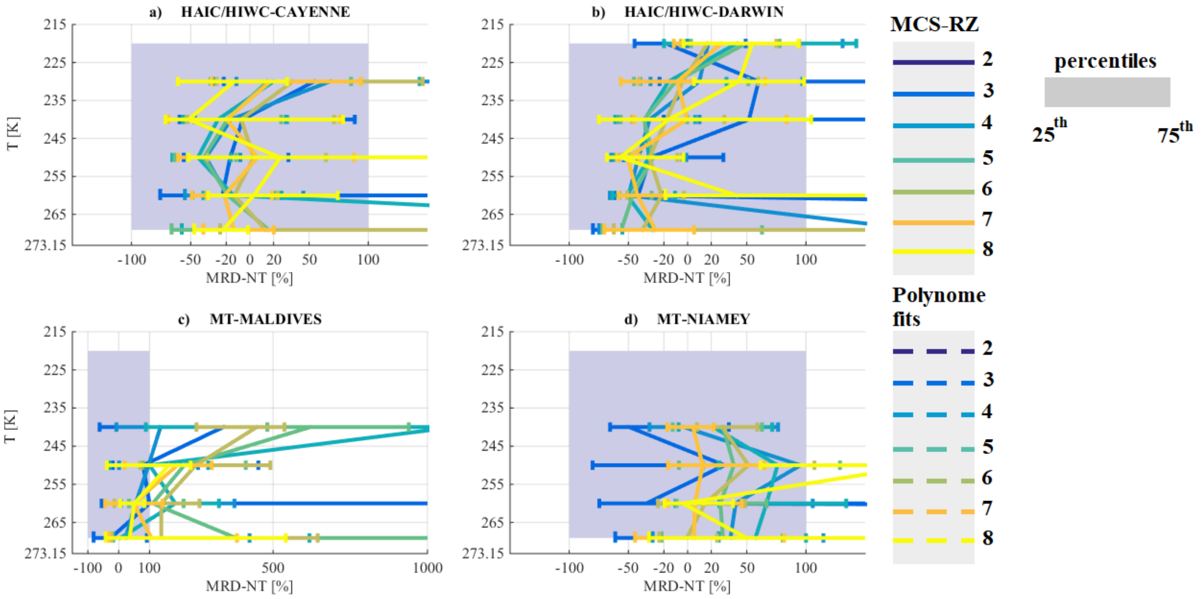

**Figure A2: Same as Figure 6, but for MRD-NT.**

## Appendices B: impact of updraft and downdraft on Median relative errors

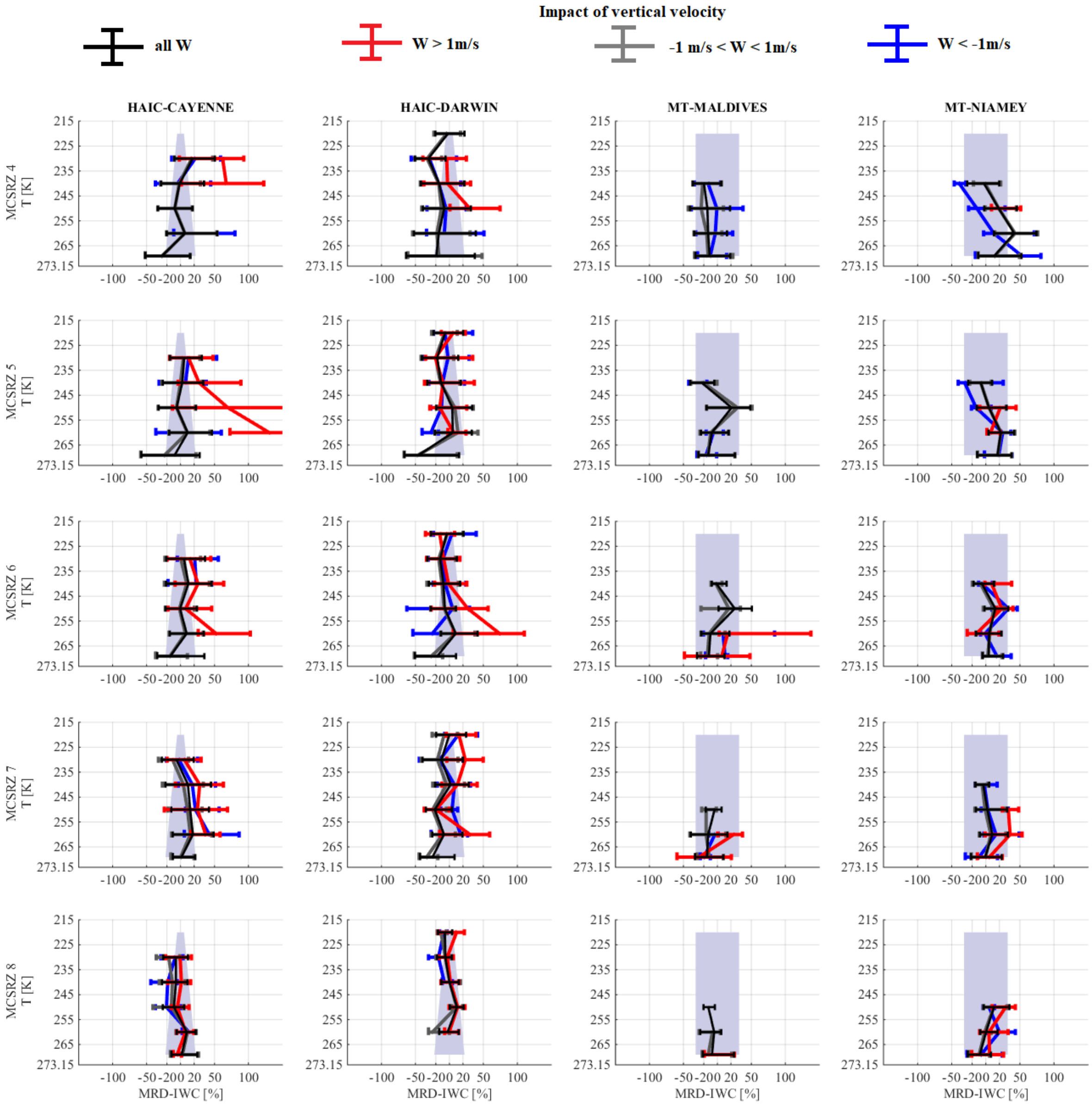

**Figure B 1: Median relative difference of IWC (MRD-IWC) with regards to median IWC calculated for the merged dataset in each MCS reflectivity zone (Figure 5). Results are sorted as function of MCSRZ 4 (top line) to MCSRZ 8 bottom line. Blue lines represent MRD-IWC for vertical velocity smaller than -1m s$^{-1}$. Grey lines represent MRD-IWC for vertical velocity larger than -1m s$^{-1}$ and smaller than 1m s$^{-1}$. Red lines represent MRD-IWC for vertical velocity larger 1m s$^{-1}$. The black lines represent MRD-IWC when there is no distinction as function of vertical velocity (same as in Figure 6-a, b, c, d).**

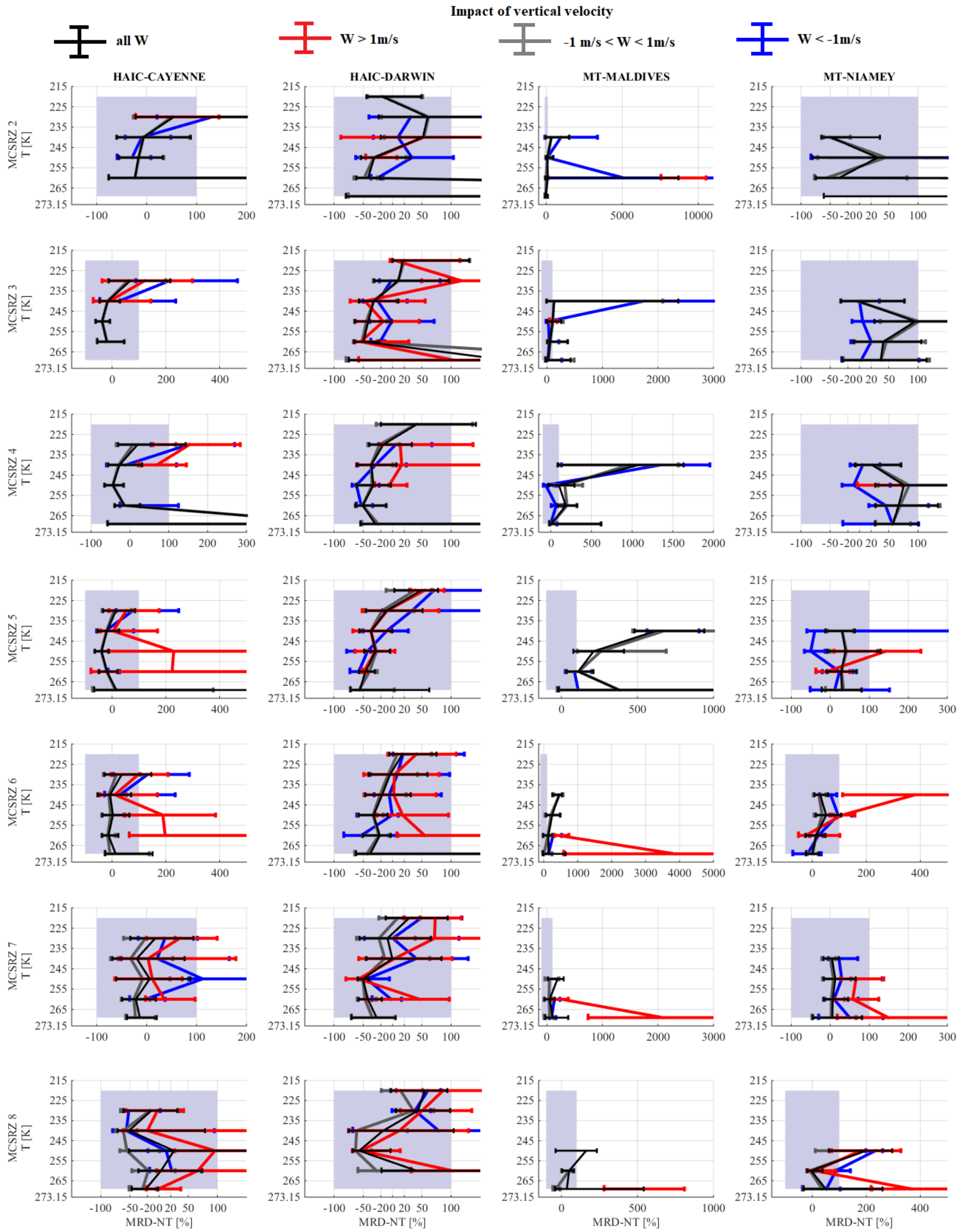

5 **Figure B2: Median relative difference of total concentration of hydrometeors (MRD-NT) with regards to median total concentrations calculated for the merged dataset in each MCS reflectivity zone (Figure A1). Results are sorted as function of MCSRZ 2 (top line) to MCSRZ 8 bottom line. Blue lines represent MRD-NT for vertical velocity smaller than -1m s$^{-1}$. Grey lines represent MRD-NT for vertical velocity larger than -1m s$^{-1}$ and smaller than 1m s$^{-1}$. Red lines represent MRD-NT for vertical velocity larger 1m s$^{-1}$. The black lines represent MRD-NT when there is no distinction as function of vertical velocity (same as in Figure A2-a, b, c, d).**

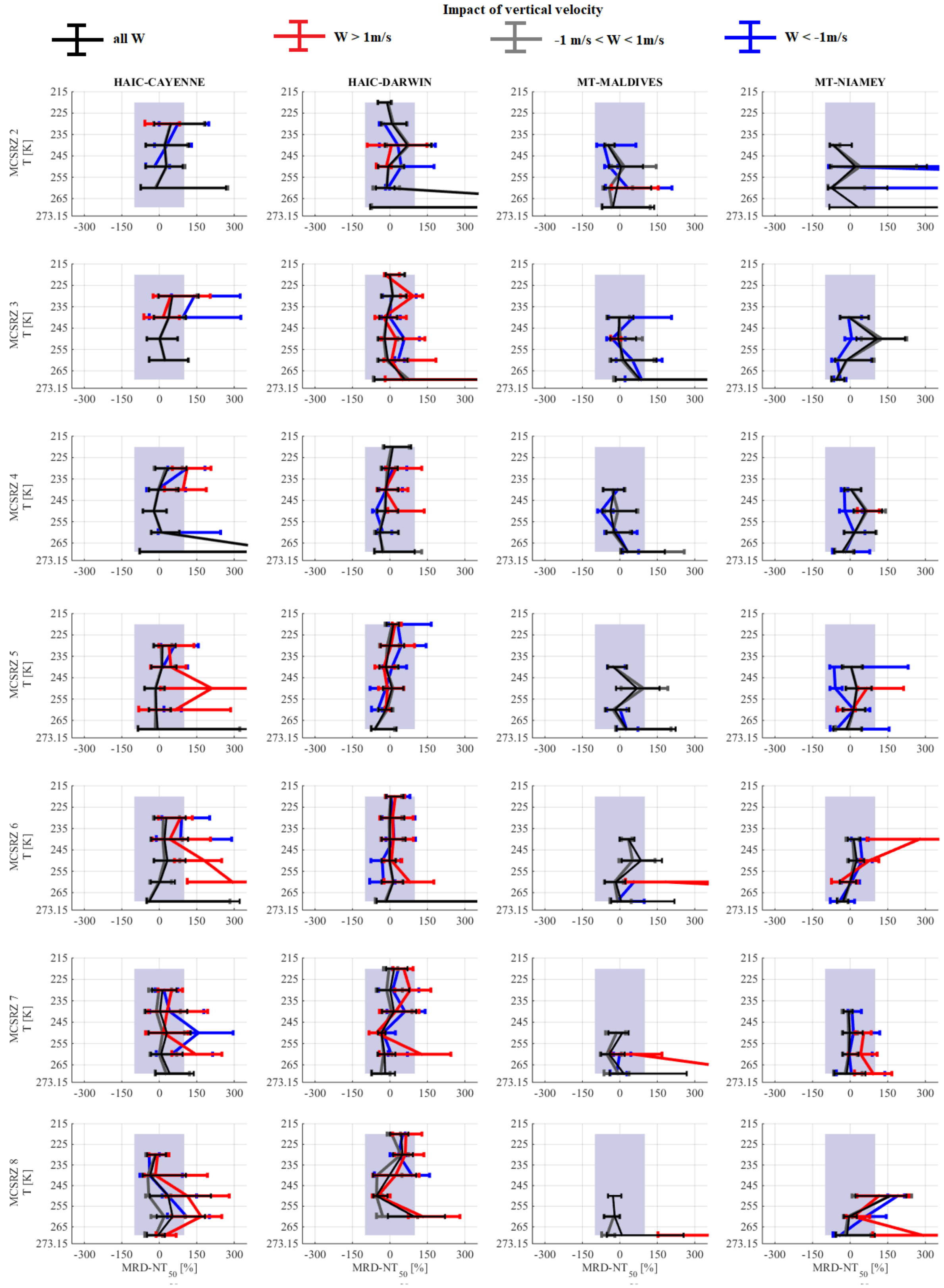

Figure B3: Median relative difference of concentration of hydrometeors summed over Dmax for Dmax larger than 50µm (MRD-$NT_{50}$) with regards to median total concentrations calculated for the merged dataset in each MCS reflectivity zone (Figure 9). Results are sorted as function of MCSRZ 2 (top line) to MCSRZ 8 bottom line. Blue lines represent MRD-$NT_{50}$ for vertical velocity smaller 5 than -1 m $s^{-1}$. Grey lines represent MRD-$NT_{50}$ for vertical velocity larger than -1 m $s^{-1}$ and smaller than 1 m $s^{-1}$. Red lines represent MRD-$NT_{50}$ for vertical velocity larger 1 m $s^{-1}$. The black lines represent MRD-$NT_{50}$ when there is no distinction as function of vertical velocity (same as in Figure 10-a, b, c, d).

## Appendices C: Tables.

**Table C 1: Percentile of Radar reflectivity factors (Z) in [dBZ], shown in solid line in Figure 1.**

| T [K] | 1rst [dBZ] | 10th [dBZ] | 30th [dBZ] | 50th [dBZ] | 70th [dBZ] | 90th [dBZ] | 99th [dBZ] |
|---|---|---|---|---|---|---|---|
| **172.5** | -7.00 | -3.45 | -0.96 | 0.90 | 2.83 | 5.32 | 11.70 |
| **177.5** | -8.33 | -5.14 | -1.96 | 0.43 | 2.81 | 5.49 | 8.69 |
| **182.5** | -9.44 | -5.96 | -3.01 | -0.56 | 2.39 | 5.51 | 8.92 |
| **187.5** | -9.93 | -6.66 | -4.07 | -1.67 | 1.08 | 5.33 | 8.53 |
| **192.5** | -10.15 | -6.79 | -4.14 | -1.85 | 0.63 | 4.97 | 8.78 |
| **197.5** | -11.08 | -6.95 | -3.80 | -1.06 | 1.48 | 5.18 | 9.24 |
| **202.5** | -12.08 | -7.53 | -3.87 | -0.74 | 2.13 | 5.37 | 9.82 |
| **207.5** | -13.25 | -8.06 | -4.00 | -0.53 | 2.69 | 5.75 | 10.22 |
| **212.5** | -16.88 | -8.65 | -4.11 | -0.44 | 3.05 | 6.28 | 10.66 |
| **217.5** | -26.79 | -10.67 | -4.54 | -0.44 | 3.37 | 6.93 | 11.27 |
| **222.5** | -30.13 | -12.58 | -5.21 | -0.30 | 3.88 | 7.71 | 12.01 |
| **227.5** | -28.30 | -13.55 | -5.17 | 0.06 | 4.61 | 8.60 | 12.94 |
| **232.5** | -26.65 | -13.08 | -4.49 | 0.75 | 5.54 | 9.70 | 14.15 |
| **237.5** | -26.54 | -11.80 | -3.26 | 2.11 | 6.76 | 10.92 | 15.08 |
| **242.5** | -24.53 | -10.27 | -1.76 | 3.62 | 7.96 | 11.76 | 15.76 |
| **247.5** | -23.78 | -8.58 | -0.20 | 5.16 | 9.13 | 12.51 | 15.98 |
| **252.5** | -22.15 | -6.76 | 1.64 | 6.58 | 10.14 | 13.17 | 16.37 |
| **257.5** | -22.05 | -5.97 | 3.18 | 7.89 | 11.09 | 13.78 | 16.86 |
| **262.5** | -21.30 | -5.83 | 4.01 | 8.59 | 11.44 | 14.11 | 17.43 |
| **267.5** | -21.90 | -5.65 | 3.89 | 8.26 | 11.03 | 13.72 | 17.34 |
| **272.5** | -20.68 | -5.77 | 2.88 | 6.86 | 9.57 | 12.60 | 16.66 |
| **277.5** | -17.52 | -4.84 | 2.73 | 6.25 | 8.90 | 12.07 | 16.42 |
| **282.5** | -15.52 | -6.62 | -1.12 | 2.30 | 5.03 | 8.33 | 15.06 |
| **287.5** | -14.40 | -7.55 | -2.90 | 0.40 | 3.18 | 7.88 | 38.13 |
| **292.5** | -13.67 | -7.94 | -4.07 | -1.37 | 1.04 | 4.55 | 10.49 |
| **297.5** | -12.95 | -7.52 | -4.00 | -1.18 | 2.90 | 27.11 | 42.87 |
| **302.5** | -10.98 | -4.72 | 0.81 | 8.39 | 14.21 | 29.74 | 44.98 |

**Table C 2: Ice water content (IWC) in [g m$^{-3}$] (Figure 5)**

| MCS RZ | | T [215;225[ | T ∈ [225;235[ | T∈ [235,245[ | T∈ [245;255[ | T∈ [255;265[ | T ∈ [265;273,15[ |
|---|---|---|---|---|---|---|---|
| 2 | 25th | 0.016 | 0.017 | 0.016 | 0.016 | 0.016 | 0.016 |
| | 50th | **0.024** | **0.024** | **0.025** | **0.023** | **0.025** | **0.026** |
| | 75th | 0.029 | 0.034 | 0.042 | 0.033 | 0.041 | 0.063 |
| 3 | 25th | 0.042 | 0.032 | 0.031 | 0.040 | 0.043 | 0.052 |
| | 50th | **0.053** | **0.052** | **0.054** | **0.062** | **0.070** | **0.098** |
| | 75th | 0.062 | 0.076 | 0.084 | 0.093 | 0.111 | 0.148 |
| 4 | 25th | 0.081 | 0.082 | 0.090 | 0.112 | 0.149 | 0.136 |
| | 50th | **0.110** | **0.119** | **0.130** | **0.160** | **0.212** | **0.198** |
| | 75th | 0.138 | 0.163 | 0.180 | 0.216 | 0.298 | 0.284 |
| 5 | 25th | 0.176 | 0.199 | 0.221 | 0.272 | 0.316 | 0.246 |
| | 50th | **0.220** | **0.261** | **0.295** | **0.351** | **0.413** | **0.342** |
| | 75th | 0.276 | 0.340 | 0.395 | 0.454 | 0.508 | 0.476 |

| | | | | | | | |
|---|---|---|---|---|---|---|---|
| 6 | 25th | 0.402 | 0.430 | 0.476 | 0.561 | 0.556 | 0.479 |
| | 50th | **0.538** | **0.572** | **0.628** | **0.690** | **0.701** | **0.624** |
| | 75th | 0.662 | 0.742 | 0.822 | 0.818 | 0.863 | 0.762 |
| 7 | 25th | 0.869 | 0.767 | 0.994 | 1.057 | 1.102 | 0.928 |
| | 50th | **1.083** | **1.069** | **1.294** | **1.295** | **1.402** | **1.204** |
| | 75th | 1.365 | 1.424 | 1.640 | 1.704 | 1.797 | 1.526 |
| 8 | 25th | 1.604 | 1.644 | 1.951 | 2.116 | 2.009 | 1.443 |
| | 50th | **1.810** | **2.051** | **2.306** | **2.515** | **2.268** | **1.827** |
| | 75th | 1.998 | 2.352 | 2.690 | 2.907 | 2.555 | 2.282 |

**Table C 3: visible extinction ($\sigma$) in [m$^{-1}$] (Figure 7).**

| **MCS RZ** | | **T ∈[215;225[** | **T∈ [225;235[** | **T∈ [235,245[** | **T ∈ [245;255[** | **T∈ [255;265[** | **T [265;273,15[** |
|---|---|---|---|---|---|---|---|
| 2 | 25th | 0.00047 | 0.00071 | 0.00044 | 0.00045 | 0.00031 | 0.00013 |
| | **50th** | **0.00097** | **0.00112** | **0.00102** | **0.00088** | **0.00078** | **0.00060** |
| | 75th | 0.00125 | 0.00172 | 0.00169 | 0.00128 | 0.00184 | 0.00413 |
| 3 | 25th | 0.00253 | 0.00188 | 0.00166 | 0.00140 | 0.00135 | 0.00118 |
| | **50th** | **0.00321** | **0.00262** | **0.00225** | **0.00205** | **0.00226** | **0.00217** |
| | 75th | 0.00363 | 0.00352 | 0.00316 | 0.00310 | 0.00337 | 0.00453 |
| 4 | 25th | 0.00521 | 0.00400 | 0.00342 | 0.00355 | 0.00400 | 0.00284 |
| | **50th** | **0.00616** | **0.00529** | **0.00466** | **0.00500** | **0.00542** | **0.00410** |
| | 75th | 0.00803 | 0.00697 | 0.00640 | 0.00685 | 0.00769 | 0.00762 |
| 5 | 25th | 0.00978 | 0.00855 | 0.00785 | 0.00765 | 0.00749 | 0.00457 |
| | **50th** | **0.01237** | **0.01101** | **0.01042** | **0.01030** | **0.00997** | **0.00693** |
| | 75th | 0.01484 | 0.01413 | 0.01348 | 0.01292 | 0.01281 | 0.01223 |
| 6 | 25th | 0.01972 | 0.01674 | 0.01550 | 0.01512 | 0.01169 | 0.00900 |
| | **50th** | **0.02478** | **0.02256** | **0.02088** | **0.01969** | **0.01596** | **0.01173** |
| | 75th | 0.03040 | 0.02904 | 0.02745 | 0.02387 | 0.01995 | 0.01515 |
| 7 | 25th | 0.03969 | 0.02892 | 0.03133 | 0.02726 | 0.02393 | 0.01722 |
| | **50th** | **0.04893** | **0.04083** | **0.04149** | **0.03386** | **0.03103** | **0.02404** |
| | 75th | 0.06096 | 0.05435 | 0.05773 | 0.04571 | 0.04127 | 0.03271 |
| 8 | 25th | 0.06965 | 0.05976 | 0.05243 | 0.05033 | 0.04139 | 0.01991 |
| | **50th** | **0.07865** | **0.07116** | **0.06944** | **0.06461** | **0.05125** | **0.03443** |
| | 75th | 0.08871 | 0.08247 | 0.08206 | 0.07942 | 0.06088 | 0.04287 |

**Table C 4: Total concentration beyond 15µm ($N_T$) in [L$^{-1}$] (Figure A1).**

| **MCS RZ** | | **T ∈[215;225[** | **T∈ [225;235[** | **T∈ [235,245[** | **T∈ [245;255[** | **T∈ [255;265[** | **T [265;273,15[** |
|---|---|---|---|---|---|---|---|
| 2 | 25th | 3.65E+01 | 7.73E+01 | 3.12E+01 | 2.51E+01 | 1.25E+01 | 6.01E+00 |
| | **50th** | **7.41E+01** | **1.53E+02** | **8.32E+01** | **5.03E+01** | **3.11E+01** | **4.26E+01** |
| | 75th | 1.58E+02 | 3.62E+02 | 1.73E+02 | 1.20E+02 | 6.54E+02 | 2.14E+03 |
| 3 | 25th | 1.67E+02 | 1.11E+02 | 5.11E+01 | 3.99E+01 | 3.24E+01 | 3.58E+01 |
| | **50th** | **1.91E+02** | **1.92E+02** | **8.26E+01** | **7.46E+01** | **5.95E+01** | **7.92E+01** |
| | 75th | 3.79E+02 | 4.22E+02 | 1.42E+02 | 1.36E+02 | 1.10E+02 | 7.41E+02 |
| 4 | 25th | 2.20E+02 | 1.56E+02 | 7.86E+01 | 6.92E+01 | 7.37E+01 | 6.47E+01 |

|  |  |  |  |  |  |  |  |
|---|---|---|---|---|---|---|---|
|  | **50th** | **4.65E+02** | **2.42E+02** | **1.34E+02** | **1.22E+02** | **1.23E+02** | **1.06E+02** |
|  | 75th | 7.04E+02 | 5.41E+02 | 2.33E+02 | 2.27E+02 | 2.22E+02 | 4.02E+02 |
| 5 | 25th | 6.63E+02 | 3.07E+02 | 1.70E+02 | 1.44E+02 | 1.19E+02 | 8.88E+01 |
|  | **50th** | **9.67E+02** | **5.45E+02** | **2.72E+02** | **2.10E+02** | **1.87E+02** | **2.14E+02** |
|  | 75th | 1.17E+03 | 9.25E+02 | 4.39E+02 | 3.14E+02 | 3.11E+02 | 1.37E+03 |
| 6 | 25th | 1.13E+03 | 5.70E+02 | 3.32E+02 | 2.73E+02 | 1.71E+02 | 1.38E+02 |
|  | **50th** | **1.40E+03** | **9.66E+02** | **5.64E+02** | **4.74E+02** | **2.51E+02** | **2.15E+02** |
|  | 75th | 2.10E+03 | 1.77E+03 | 9.09E+02 | 7.59E+02 | 3.93E+02 | 6.93E+02 |
| 7 | 25th | 2.28E+03 | 9.57E+02 | 7.26E+02 | 6.30E+02 | 3.37E+02 | 2.70E+02 |
|  | **50th** | **3.40E+03** | **1.91E+03** | **1.35E+03** | **9.98E+02** | **5.37E+02** | **5.58E+02** |
|  | 75th | 5.05E+03 | 3.35E+03 | 2.45E+03 | 1.53E+03 | 8.78E+02 | 1.10E+03 |
| 8 | 25th | 6.26E+03 | 3.08E+03 | 7.64E+02 | 7.81E+02 | 7.63E+02 | 4.61E+02 |
|  | **50th** | **9.55E+03** | **5.13E+03** | **1.68E+03** | **1.96E+03** | **1.13E+03** | **8.05E+02** |
|  | 75th | 1.28E+04 | 7.37E+03 | 6.09E+03 | 5.20E+03 | 1.82E+03 | 1.99E+03 |

**Table C 5: Total concentration since 50µm ($N_{T\,50}$) in [L$^{-1}$] (Figure 9).**

| MCS RZ |  | T ∈[215;225[ | T∈ [225;235[ | T∈ [235,245[ | T∈ [245;255[ | T∈ [255;265[ | T [265;273,15[ |
|---|---|---|---|---|---|---|---|
| 2 | 25th | 8.65E+00 | 1.72E+01 | 5.24E+00 | 3.98E+00 | 1.18E+00 | 7.57E-01 |
|  | **50th** | **2.13E+01** | **3.21E+01** | **1.68E+01** | **9.13E+00** | **4.49E+00** | **3.32E+00** |
|  | 75th | 3.99E+01 | 5.77E+01 | 3.26E+01 | 1.90E+01 | 1.21E+01 | 4.28E+01 |
| 3 | 25th | 4.16E+01 | 3.05E+01 | 1.35E+01 | 8.50E+00 | 4.42E+00 | 2.18E+00 |
|  | **50th** | **4.75E+01** | **4.70E+01** | **2.19E+01** | **1.39E+01** | **8.82E+00** | **4.79E+00** |
|  | 75th | 8.35E+01 | 7.79E+01 | 3.68E+01 | 2.60E+01 | 1.74E+01 | 2.07E+01 |
| 4 | 25th | 6.38E+01 | 4.66E+01 | 2.15E+01 | 1.47E+01 | 1.02E+01 | 7.28E+00 |
|  | **50th** | **1.05E+02** | **7.25E+01** | **3.56E+01** | **2.78E+01** | **1.72E+01** | **1.38E+01** |
|  | 75th | 1.64E+02 | 1.23E+02 | 6.21E+01 | 4.49E+01 | 3.03E+01 | 2.46E+01 |
| 5 | 25th | 1.57E+02 | 9.14E+01 | 4.70E+01 | 3.33E+01 | 1.83E+01 | 1.11E+01 |
|  | **50th** | **2.06E+02** | **1.39E+02** | **7.26E+01** | **5.66E+01** | **3.03E+01** | **2.30E+01** |
|  | 75th | 2.49E+02 | 2.10E+02 | 1.14E+02 | 8.17E+01 | 4.78E+01 | 4.39E+01 |
| 6 | 25th | 2.68E+02 | 1.55E+02 | 9.50E+01 | 7.22E+01 | 3.00E+01 | 1.78E+01 |
|  | **50th** | **3.28E+02** | **2.47E+02** | **1.50E+02** | **1.06E+02** | **4.91E+01** | **2.86E+01** |
|  | 75th | 4.84E+02 | 4.12E+02 | 2.34E+02 | 1.45E+02 | 7.25E+01 | 6.47E+01 |
| 7 | 25th | 5.65E+02 | 2.49E+02 | 2.07E+02 | 1.36E+02 | 7.20E+01 | 3.35E+01 |
|  | **50th** | **7.83E+02** | **4.92E+02** | **3.41E+02** | **1.90E+02** | **1.13E+02** | **9.02E+01** |
|  | 75th | 1.12E+03 | 8.00E+02 | 6.20E+02 | 3.08E+02 | 1.84E+02 | 1.74E+02 |
| 8 | 25th | 1.34E+03 | 7.26E+02 | 2.06E+02 | 1.90E+02 | 1.82E+02 | 7.29E+01 |
|  | **50th** | **1.82E+03** | **1.09E+03** | **3.86E+02** | **4.01E+02** | **2.83E+02** | **1.57E+02** |
|  | 75th | 2.30E+03 | 1.51E+03 | 1.31E+03 | 9.29E+02 | 4.95E+02 | 3.10E+02 |

**Table C 6: Total concentration since 500µm ($N_{T\,500}$) in [L$^{-1}$] (Figure 11).**

| MCS RZ |  | T ∈[215;225[ | T∈ [225;235[ | T∈ [235,245[ | T∈ [245;255[ | T∈ [255;265[ | T∈ [265;273,15[ |
|---|---|---|---|---|---|---|---|

| | | | | | | | |
|---|---|---|---|---|---|---|---|
| 2 | 25th | 0.00E+00 | 1.96E-02 | 4.08E-02 | 1.33E-01 | 8.31E-02 | 1.68E-02 |
| | **50th** | **5.20E-02** | **7.23E-02** | **1.73E-01** | **3.41E-01** | **2.86E-01** | **8.60E-02** |
| | 75th | 2.05E-01 | 1.88E-01 | 4.13E-01 | 7.27E-01 | 6.52E-01 | 3.37E-01 |
| 3 | 25th | 1.12E+00 | 4.23E-01 | 8.37E-01 | 1.09E+00 | 8.64E-01 | 3.57E-01 |
| | **50th** | **1.57E+00** | **8.68E-01** | **1.33E+00** | **1.61E+00** | **1.40E+00** | **6.67E-01** |
| | 75th | 2.03E+00 | 1.43E+00 | 1.91E+00 | 2.22E+00 | 2.07E+00 | 1.29E+00 |
| 4 | 25th | 2.77E+00 | 1.92E+00 | 2.26E+00 | 2.96E+00 | 2.73E+00 | 1.67E+00 |
| | **50th** | **3.77E+00** | **2.73E+00** | **3.15E+00** | **3.95E+00** | **3.91E+00** | **2.40E+00** |
| | 75th | 4.54E+00 | 3.84E+00 | 4.40E+00 | 5.06E+00 | 5.51E+00 | 3.52E+00 |
| 5 | 25th | 5.61E+00 | 5.55E+00 | 5.71E+00 | 5.83E+00 | 5.29E+00 | 2.82E+00 |
| | **50th** | **7.78E+00** | **7.26E+00** | **7.68E+00** | **7.78E+00** | **7.19E+00** | **4.15E+00** |
| | 75th | 9.34E+00 | 9.48E+00 | 1.01E+01 | 1.02E+01 | 8.98E+00 | 6.60E+00 |
| 6 | 25th | 1.25E+01 | 1.27E+01 | 1.19E+01 | 1.21E+01 | 9.61E+00 | 3.83E+00 |
| | **50th** | **1.55E+01** | **1.60E+01** | **1.56E+01** | **1.45E+01** | **1.24E+01** | **6.07E+00** |
| | 75th | 1.97E+01 | 2.02E+01 | 2.06E+01 | 1.74E+01 | 1.53E+01 | 9.17E+00 |
| 7 | 25th | 2.26E+01 | 2.00E+01 | 2.41E+01 | 2.01E+01 | 1.83E+01 | 8.29E+00 |
| | **50th** | **2.83E+01** | **2.65E+01** | **3.08E+01** | **2.52E+01** | **2.42E+01** | **1.54E+01** |
| | 75th | 3.34E+01 | 3.35E+01 | 3.96E+01 | 3.44E+01 | 3.35E+01 | 2.40E+01 |
| 8 | 25th | 1.95E+01 | 2.69E+01 | 3.35E+01 | 3.71E+01 | 2.67E+01 | 1.06E+01 |
| | **50th** | **2.38E+01** | **3.75E+01** | **4.89E+01** | **4.99E+01** | **3.73E+01** | **2.43E+01** |
| | 75th | 2.85E+01 | 5.23E+01 | 7.29E+01 | 6.87E+01 | 4.86E+01 | 3.80E+01 |

**Table C 7: pre-factor $\alpha$ of mass size relationship in [g cm$^{-\beta}$] (Figure 15).**

| **MCS RZ** | | **T ∈[215;225[** | **T∈ [225;235[** | **T∈ [235,245[** | **T∈ [245;255[** | **T∈ [255;265[** | **T [265;273,15[** |
|---|---|---|---|---|---|---|---|
| 2 | 25th | 0.00095 | 0.00042 | 0.00053 | 0.00086 | 0.00152 | 0.00114 |
| | **50th** | **0.00269** | **0.00099** | **0.00128** | **0.00172** | **0.00341** | **0.00322** |
| | 75th | 0.00574 | 0.00276 | 0.00320 | 0.00312 | 0.00876 | 0.00809 |
| 3 | 25th | 0.00092 | 0.00059 | 0.00099 | 0.00149 | 0.00190 | 0.00319 |
| | **50th** | **0.00126** | **0.00115** | **0.00181** | **0.00241** | **0.00341** | **0.00687** |
| | 75th | 0.00154 | 0.00197 | 0.00299 | 0.00379 | 0.00630 | 0.01077 |
| 4 | 25th | 0.00142 | 0.00126 | 0.00184 | 0.00250 | 0.00343 | 0.00385 |
| | **50th** | **0.00180** | **0.00198** | **0.00274** | **0.00340** | **0.00505** | **0.00592** |
| | 75th | 0.00235 | 0.00282 | 0.00404 | 0.00470 | 0.00711 | 0.00826 |
| 5 | 25th | 0.00195 | 0.00188 | 0.00267 | 0.00333 | 0.00422 | 0.00481 |
| | **50th** | **0.00241** | **0.00258** | **0.00351** | **0.00414** | **0.00562** | **0.00658** |
| | 75th | 0.00300 | 0.00336 | 0.00455 | 0.00529 | 0.00742 | 0.00950 |
| 6 | 25th | 0.00189 | 0.00210 | 0.00324 | 0.00419 | 0.00486 | 0.00595 |
| | **50th** | **0.00271** | **0.00285** | **0.00403** | **0.00513** | **0.00625** | **0.00782** |
| | 75th | 0.00334 | 0.00380 | 0.00492 | 0.00638 | 0.00793 | 0.01014 |
| 7 | 25th | 0.00163 | 0.00253 | 0.00325 | 0.00466 | 0.00527 | 0.00594 |
| | **50th** | **0.00245** | **0.00351** | **0.00415** | **0.00560** | **0.00637** | **0.00774** |
| | 75th | 0.00326 | 0.00447 | 0.00517 | 0.00668 | 0.00776 | 0.01077 |
| 8 | 25th | 0.00214 | 0.00302 | 0.00363 | 0.00405 | 0.00538 | 0.00637 |
| | **50th** | **0.00418** | **0.00485** | **0.00496** | **0.00558** | **0.00712** | **0.00953** |
| | 75th | 0.00748 | 0.00750 | 0.00679 | 0.00819 | 0.01173 | 0.01886 |

**Table C 8: exponent of mass-size relationship $\beta$ [no dimension] (Figure 13).**

| MCS RZ | | T ∈[215;225[ | T∈ [225;235[ | T∈ [235,245[ | T∈ [245;255[ | T∈ [255;265[ | T [265;273,15[ |
|---|---|---|---|---|---|---|---|
| 2 | 25th | 1.67 | 1.54 | 1.58 | 1.66 | 1.74 | 1.66 |
| | **50th** | **1.86** | **1.76** | **1.78** | **1.85** | **1.95** | **1.93** |
| | 75th | 2.07 | 1.96 | 1.99 | 2.02 | 2.21 | 2.08 |
| 3 | 25th | 1.80 | 1.65 | 1.75 | 1.79 | 1.86 | 1.86 |
| | **50th** | **1.88** | **1.82** | **1.91** | **1.92** | **2.00** | **2.08** |
| | 75th | 1.95 | 1.96 | 2.04 | 2.05 | 2.17 | 2.35 |
| 4 | 25th | 1.90 | 1.82 | 1.87 | 1.91 | 1.96 | 1.94 |
| | **50th** | **1.98** | **1.94** | **1.99** | **2.02** | **2.10** | **2.10** |
| | 75th | 2.03 | 2.04 | 2.10 | 2.12 | 2.22 | 2.26 |
| 5 | 25th | 1.99 | 1.91 | 1.96 | 1.97 | 2.02 | 2.05 |
| | **50th** | **2.07** | **2.00** | **2.06** | **2.05** | **2.11** | **2.16** |
| | 75th | 2.12 | 2.08 | 2.14 | 2.14 | 2.21 | 2.29 |
| 6 | 25th | 1.91 | 1.92 | 2.01 | 2.04 | 2.03 | 2.04 |
| | **50th** | **2.06** | **2.01** | **2.09** | **2.11** | **2.11** | **2.16** |
| | 75th | 2.14 | 2.11 | 2.16 | 2.19 | 2.20 | 2.26 |
| 7 | 25th | 1.86 | 1.97 | 1.99 | 2.06 | 2.06 | 2.07 |
| | **50th** | **2.00** | **2.08** | **2.08** | **2.13** | **2.13** | **2.15** |
| | 75th | 2.10 | 2.17 | 2.16 | 2.19 | 2.19 | 2.26 |
| 8 | 25th | 1.93 | 1.98 | 1.97 | 2.01 | 2.07 | 2.10 |
| | **50th** | **2.11** | **2.13** | **2.08** | **2.13** | **2.16** | **2.21** |
| | 75th | 2.27 | 2.25 | 2.19 | 2.22 | 2.29 | 2.34 |

**Table C 9: $max(D_{max})$ in [cm] (Figure 17).**

| MCS RZ | | T ∈[215;225[ | T∈ [225;235[ | T∈ [235,245[ | T∈ [245;255[ | T∈ [255;265[ | T [265;273,15[ |
|---|---|---|---|---|---|---|---|
| 2 | 25th | 0.048 | 0.061 | 0.090 | 0.105 | 0.125 | 0.105 |
| | **50th** | **0.090** | **0.095** | **0.110** | **0.140** | **0.195** | **0.165** |
| | 75th | 0.120 | 0.115 | 0.140 | 0.195 | 0.361 | 0.255 |
| 3 | 25th | 0.155 | 0.120 | 0.145 | 0.155 | 0.205 | 0.245 |
| | **50th** | **0.175** | **0.145** | **0.190** | **0.205** | **0.310** | **0.435** |
| | 75th | 0.195 | 0.180 | 0.265 | 0.295 | 0.620 | 0.762 |
| 4 | 25th | 0.205 | 0.170 | 0.195 | 0.215 | 0.280 | 0.332 |
| | **50th** | **0.235** | **0.212** | **0.260** | **0.347** | **0.525** | **0.445** |
| | 75th | 0.265 | 0.270 | 0.380 | 0.615 | 0.790 | 0.775 |
| 5 | 25th | 0.235 | 0.225 | 0.265 | 0.280 | 0.350 | 0.415 |
| | **50th** | **0.280** | **0.280** | **0.375** | **0.405** | **0.625** | **0.615** |
| | 75th | 0.340 | 0.355 | 0.575 | 0.685 | 0.820 | 0.795 |
| 6 | 25th | 0.245 | 0.245 | 0.310 | 0.335 | 0.385 | 0.475 |
| | **50th** | **0.315** | **0.310** | **0.460** | **0.665** | **0.625** | **0.735** |
| | 75th | 0.395 | 0.435 | 0.680 | 0.880 | 0.810 | 0.838 |
| 7 | 25th | 0.225 | 0.270 | 0.325 | 0.445 | 0.480 | 0.557 |
| | **50th** | **0.285** | **0.397** | **0.452** | **0.675** | **0.675** | **0.745** |

| | | | | | | | |
|---|---|---|---|---|---|---|---|
| | 75th | 0.375 | 0.595 | 0.645 | 0.846 | 0.810 | 0.825 |
| 8 | 25th | 0.335 | 0.315 | 0.395 | 0.445 | 0.445 | 0.455 |
| | **50th** | **0.455** | **0.480** | **0.555** | **0.632** | **0.595** | **0.635** |
| | 75th | 0.665 | 0.730 | 0.790 | 0.825 | 0.740 | 0.745 |

**Table C 10: Second Moment of PSD (*M*$_2$) [m$^{-1}$] (Figure 21).**

| **MCS RZ** | | **T∈ [215;225[** | **T∈ [225;235[** | **T∈ [235,245[** | **T∈ [245;255[** | **T∈ [255;265[** | **T ∈ [265;273,15[** |
|---|---|---|---|---|---|---|---|
| 2 | 25th | 4.33E-04 | 5.99E-04 | 3.90E-04 | 4.41E-04 | 3.03E-04 | 1.22E-04 |
| | **50th** | **8.04E-04** | **9.32E-04** | **8.67E-04** | **8.18E-04** | **7.10E-04** | **5.50E-04** |
| | 75th | 9.78E-04 | 1.37E-03 | 1.42E-03 | 1.20E-03 | 1.57E-03 | 2.62E-03 |
| 3 | 25th | 2.26E-03 | 1.71E-03 | 1.50E-03 | 1.36E-03 | 1.26E-03 | 1.01E-03 |
| | **50th** | **2.85E-03** | **2.32E-03** | **2.03E-03** | **1.98E-03** | **2.07E-03** | **1.83E-03** |
| | 75th | 3.21E-03 | 3.08E-03 | 2.80E-03 | 2.80E-03 | 3.01E-03 | 3.50E-03 |
| 4 | 25th | 4.59E-03 | 3.60E-03 | 3.10E-03 | 3.30E-03 | 3.70E-03 | 2.71E-03 |
| | **50th** | **5.43E-03** | **4.73E-03** | **4.17E-03** | **4.60E-03** | **4.99E-03** | **3.72E-03** |
| | 75th | 6.99E-03 | 6.10E-03 | 5.69E-03 | 6.38E-03 | 6.91E-03 | 6.39E-03 |
| 5 | 25th | 8.78E-03 | 7.82E-03 | 7.20E-03 | 7.11E-03 | 7.07E-03 | 4.43E-03 |
| | **50th** | **1.13E-02** | **9.99E-03** | **9.56E-03** | **9.55E-03** | **9.19E-03** | **6.49E-03** |
| | 75th | 1.34E-02 | 1.27E-02 | 1.23E-02 | 1.21E-02 | 1.17E-02 | 1.07E-02 |
| 6 | 25th | 1.79E-02 | 1.60E-02 | 1.42E-02 | 1.40E-02 | 1.10E-02 | 8.29E-03 |
| | **50th** | **2.28E-02** | **2.09E-02** | **1.95E-02** | **1.83E-02** | **1.48E-02** | **1.06E-02** |
| | 75th | 2.77E-02 | 2.66E-02 | 2.53E-02 | 2.25E-02 | 1.85E-02 | 1.38E-02 |
| 7 | 25th | 3.57E-02 | 2.75E-02 | 2.93E-02 | 2.57E-02 | 2.27E-02 | 1.53E-02 |
| | **50th** | **4.41E-02** | **3.79E-02** | **3.86E-02** | **3.22E-02** | **2.96E-02** | **2.21E-02** |
| | 75th | 5.39E-02 | 4.94E-02 | 5.29E-02 | 4.31E-02 | 3.95E-02 | 3.11E-02 |
| 8 | 25th | 6.02E-02 | 5.30E-02 | 4.92E-02 | 4.77E-02 | 3.96E-02 | 1.85E-02 |
| | **50th** | **6.73E-02** | **6.39E-02** | **6.39E-02** | **6.21E-02** | **4.95E-02** | **3.23E-02** |
| | 75th | 7.41E-02 | 7.30E-02 | 7.36E-02 | 7.53E-02 | 5.84E-02 | 4.27E-02 |

**Table C 11: Third moment of PSD (*M*$_3$) in [1] (Figure 23).**

| **MCS RZ** | | **T ∈[215;225[** | **T∈ [225;235[** | **T∈ [235,245[** | **T∈ [245;255[** | **T∈ [255;265[** | **T ∈ [265;273,15[** |
|---|---|---|---|---|---|---|---|
| 2 | 25th | 1.29E-07 | 1.30E-07 | 1.07E-07 | 1.43E-07 | 1.68E-07 | 5.16E-08 |
| | **50th** | **1.78E-07** | **2.09E-07** | **2.29E-07** | **2.98E-07** | **3.83E-07** | **1.92E-07** |
| | 75th | 2.12E-07 | 2.98E-07 | 4.00E-07 | 5.38E-07 | 6.36E-07 | 5.66E-07 |
| 3 | 25th | 7.85E-07 | 5.40E-07 | 6.75E-07 | 7.36E-07 | 8.89E-07 | 7.74E-07 |
| | **50th** | **1.06E-06** | **8.08E-07** | **9.69E-07** | **1.11E-06** | **1.56E-06** | **1.92E-06** |
| | 75th | 1.27E-06 | 1.08E-06 | 1.43E-06 | 1.67E-06 | 3.59E-06 | 5.23E-06 |
| 4 | 25th | 1.85E-06 | 1.47E-06 | 1.75E-06 | 2.15E-06 | 3.08E-06 | 2.52E-06 |
| | **50th** | **2.44E-06** | **1.99E-06** | **2.43E-06** | **3.57E-06** | **5.71E-06** | **3.98E-06** |
| | 75th | 3.08E-06 | 2.80E-06 | 3.61E-06 | 5.99E-06 | 1.13E-05 | 1.12E-05 |
| 5 | 25th | 4.13E-06 | 3.92E-06 | 4.59E-06 | 4.80E-06 | 5.95E-06 | 5.13E-06 |
| | **50th** | **5.55E-06** | **5.20E-06** | **6.64E-06** | **7.83E-06** | **1.08E-05** | **8.69E-06** |
| | 75th | 7.08E-06 | 6.84E-06 | 9.57E-06 | 1.13E-05 | 1.93E-05 | 1.93E-05 |

| | | | | | | | |
|---|---|---|---|---|---|---|---|
| 6 | 25th | 9.42E-06 | 8.92E-06 | 9.88E-06 | 9.93E-06 | 9.93E-06 | 8.90E-06 |
| | **50th** | **1.19E-05** | **1.17E-05** | **1.45E-05** | **1.77E-05** | **1.66E-05** | **1.75E-05** |
| | 75th | 1.43E-05 | 1.51E-05 | 1.93E-05 | 2.50E-05 | 2.54E-05 | 2.62E-05 |
| 7 | 25th | 1.66E-05 | 1.75E-05 | 1.98E-05 | 2.51E-05 | 2.37E-05 | 1.91E-05 |
| | **50th** | **2.02E-05** | **2.16E-05** | **2.63E-05** | **3.05E-05** | **3.35E-05** | **3.28E-05** |
| | 75th | 2.36E-05 | 2.71E-05 | 3.20E-05 | 3.82E-05 | 4.24E-05 | 4.25E-05 |
| 8 | 25th | 2.07E-05 | 2.20E-05 | 2.80E-05 | 3.13E-05 | 2.74E-05 | 1.54E-05 |
| | **50th** | **2.27E-05** | **2.69E-05** | **3.29E-05** | **4.16E-05** | **3.89E-05** | **2.84E-05** |
| | 75th | 2.45E-05 | 3.21E-05 | 4.30E-05 | 5.76E-05 | 5.22E-05 | 4.57E-05 |

**Table C 12: coefficient *A* in [kg m$^{-2}$] (Figure 25).**

| **MCS RZ** | | **T ∈[215;225[** | **T∈ [225;235[** | **T∈ [235,245[** | **T∈ [245;255[** | **T∈ [255;265[** | **T ∈ [265;273,15[** |
|---|---|---|---|---|---|---|---|
| 2 | 25th | 0.021 | 0.018 | 0.018 | 0.019 | 0.017 | 0.019 |
| | **50th** | **0.031** | **0.025** | **0.032** | **0.031** | **0.041** | **0.048** |
| | 75th | 0.042 | 0.038 | 0.064 | 0.054 | 0.085 | 0.163 |
| 3 | 25th | 0.017 | 0.016 | 0.018 | 0.024 | 0.025 | 0.029 |
| | **50th** | **0.018** | **0.023** | **0.026** | **0.032** | **0.037** | **0.052** |
| | 75th | 0.020 | 0.030 | 0.036 | 0.041 | 0.051 | 0.071 |
| 4 | 25th | 0.017 | 0.019 | 0.023 | 0.027 | 0.034 | 0.037 |
| | **50th** | **0.020** | **0.025** | **0.029** | **0.034** | **0.042** | **0.048** |
| | 75th | 0.021 | 0.031 | 0.038 | 0.043 | 0.051 | 0.061 |
| 5 | 25th | 0.018 | 0.022 | 0.026 | 0.031 | 0.038 | 0.038 |
| | **50th** | **0.020** | **0.026** | **0.031** | **0.037** | **0.045** | **0.047** |
| | 75th | 0.023 | 0.030 | 0.037 | 0.045 | 0.053 | 0.061 |
| 6 | 25th | 0.021 | 0.024 | 0.028 | 0.033 | 0.042 | 0.047 |
| | **50th** | **0.023** | **0.027** | **0.032** | **0.037** | **0.048** | **0.057** |
| | 75th | 0.026 | 0.031 | 0.038 | 0.045 | 0.057 | 0.069 |
| 7 | 25th | 0.023 | 0.025 | 0.028 | 0.036 | 0.041 | 0.047 |
| | **50th** | **0.024** | **0.028** | **0.032** | **0.040** | **0.046** | **0.054** |
| | 75th | 0.027 | 0.031 | 0.038 | 0.044 | 0.053 | 0.064 |
| 8 | 25th | 0.025 | 0.029 | 0.032 | 0.035 | 0.041 | 0.048 |
| | **50th** | **0.027** | **0.032** | **0.038** | **0.039** | **0.045** | **0.060** |
| | 75th | 0.030 | 0.035 | 0.045 | 0.047 | 0.053 | 0.080 |

## Appendices D: summary of inter-comparison of ice microphysical properties in MCS.

Table D1 summarizes qualitatively the findings for IWC, visible extinction ($\sigma$), total concentrations ($N_{T,50}$ for $D_{max}$>50µm; $N_{T,500}$ for $D_{max}$>500µm), 2nd moment ($M_2$) and 3rd moment ($M_3$) of hydrometeor PSD, and largest hydrometeors sizes ($max(D_{max})$). It highlights the main tendencies of microphysical parameters in each types of MCS with regards to the median calculation performed for the merged dataset, such: ≅ for similar values, + for larger values and – for smaller values than merged dataset. Also, it points out the exceptions noting their location as function of the temperature range and the MCS reflectivity zones.

**Table D1: Evaluation of parameter X (X for IWC, $\sigma$, $N_{T,55}$, $N_{T,500}$, , $M_2$, $M_3$ and $max(D_{max})$) , for each type of tropical MCS (Darwin, Cayenne, Maldives Islands, Niamey) with respect to the global tropical dataset thereby comparing median values in corresponding MCS reflectivity zones. Two sub-columns for each type of MCS: The first column gives an evaluation of the main trend: ≅ if MRD-X is comparable to the uncertainty range, + if MRD-X is larger than the uncertainty range, - for smaller values. In the second sub-column are reported the number of exceptions with respect to the main trend (first column) with: Z(Y)≅ or Z(Y)+ or Z(Y)-. Z number stands for a particular MCS reflectivity zone (with Z= 2, 3, 4, 5, 6, 7, 8) , Y number represents a particular T range (with Y=1 for T ∊ [265K; 273.15K[, Y=2 for T ∊ [255K, 265K[, Y=3 for T ∊ [245K; 255K[, Y=4 for T ∊ [235K; 245K[, Y=5 for T ∊ [225K; 235K[, and Y=6 for T ∊ [215K; 225K[).**

| With respect to median of | MCS over Darwin | | MCS over Cayenne | | Maldives Islands MCS | | Niamey's MCS | |
|---|---|---|---|---|---|---|---|---|
| IWC | ≅ | 4(6)+, 5(1)- | ≅ | 4(1,5)-, 5(5)- | ≅ | | ≅ | 4(2)+ |
| $\sigma$ | ≅ | 5(1)+ | ≅ | 8(1)- | ≅ | | ≅ | 2(4)- |
| $N_{T,55}$ | ≅ | 4(1)+ | ≅ | 3(1)+ | ≅ | | ≅ | 8(3)+, 3(3)+ |
| $N_{T,500}$ | ≅ | 8(1)+, 7(1)+ | ≅ | 8(3)+, 8(1)- | ≅ | 7(4)+, 3(1)+ | ≅ | 8(1)- |
| $M_2$ | ≅ | 4(1)+, 5(1)+ | ≅ | 8(1)-, 2(1)+ | ≅ | | ≅ | 4(6), 2(6)+ |
| $M_3$ | ≅ | 8(1)+ | ≅ | 8(1)+, 2(1)+ | ≅ | | ≅ | 2(1)+, 3(1,2,3)+<br>4(1,2)+<br>5(1)+ |
| $max(D_{max})$ | ≅ | 2(2)+, 7(3,4)- | ≅ | 6(3)-, 8(2)-, 8(3)+ | - | 8≅ | + | 6(1,2) ≅, 7 ≅, 8 ≅ |

## Appendices E: rescaled PSD parameterization for spherical equivalent diameter

Models for NWP usually use the assumption that ice hydrometeors are spherical. However, our study presents results using maximum diameter ($D_{max}$). There is a possibility that the last definition might not be adapted for NWP. We propose to explore the impact on the proposed parameterizations of PSD calculated in the main text when assuming the volume of spherical hydrometeors. First, we need to compute the volume of the hydrometeors from the in-situ measurement. For that we assume that hydrometeors are oblate spheroids. It is possible from the images recorded by the OAP to deduced $D_{max}$ and the width (width: length perpendicular to $D_{max}$). With this assumptions it is possible to calculate the volume of such oblate spheroids ($V(D_{max}) = 0.25*\pi*width(D_{max})*D_{max}^2$). Then, we calculate the equivalent spherical diameter for the volume computed for this spheroid ($D_{sp}(D_{max}) = (6*V(D_{max})/\pi)^{1/3}$). For each bin of $D_{max}$ there is a calculation of the mean width from all its particles and for every 5 seconds period, hence a $D_{sp}(D_{max})$. Then, second and third moment ($M_{2Dsp}$ and $M_{3Dsp}$, respectively) of PSD can be calculated replacing $D_{max}$ in Eq. (9) with $D_{sp}$ (Eq. E1).

$$M_n = \sum_{D_{max}=55\mu m}^{D_{max}=1,2cm} N(D_{sp}) \cdot D_{sp}^{n} \cdot \Delta D_{sp} \qquad [m^{n-3}] \qquad (E1)$$

Because, it is calculated on measured PSD, $N(D_{sp}) = N(D_{max})$ and $\Delta D_{sp} = \Delta D_{max}$. The results for second moment of PSD are presented in Figure E1 and Figure E2, respectively. Where Figure E1 shows $M_{2Dsp}$ and Figure E2 shows MRD-$M_{2Dsp}$ both as function of MCS reflectivity zones and temperature. Same for $M_{3Dsp}$ and MRD-$M_{3Dsp}$ presented in Figure E3 and Figure E4 respectively. For the second moment of PSD as function of Dsp results are similar than for second moment for PSD as function of $D_{max}$, except that for a given MCS reflectivity zones $M_{2Dsp}$ are about 30% smaller than $M_2$ from $D_{max}$. We obtain the same conclusion for the third moment, but $M_{3Dsp}$ are about 40% to 50% smaller than $M_3$ from $D_{max}$. However, MRD-$M_{2Dsp}$ and MRD-$M_{3Dsp}$ are similar to MRD-$M_2$ and MRD-$M_3$ from $D_{max}$.

As second and third moment from PSD as function of Dsp are smaller than second moment from PSD as function of $D_{max}$, Eq. (12) and Eq. (18) need to be updated such (Figure E5 and Figure E6):

$$A(T) = 1.656 \cdot 10^{-5} \cdot T^2 - 0.0070224 \cdot T + 0.7780590 \qquad [kg\, m^{-2}] \qquad (E2)$$

Hence, Eq. (E2) is used in Eq. (17) to calculate the second moment of PSD as functions of $D_{sp}$. Then, Eq. (E3) is used instead of Eq. (18) to calculated third moment of PSD as function of $D_{sp}$.

$$\begin{aligned} M_3 = {} & [-3.066 - 0.6124 \cdot log(IWC) + 0.004251 \cdot T - 0.02495 \cdot log(IWC)^2 + 0.0002413 \cdot log(IWC) \cdot T] \cdot M_2^{F(3)} \\ & \cdot D(3) \cdot exp(E(3) \cdot T_c) \end{aligned} \qquad (E3)$$

Figure E7 shows efficiency of the updated parameterization for second and third of PSD as function of $D_{sp}$. Figure E7 and Figure 27 are similar, demonstrating that the parameterization for PSD as function of $D_{sp}$ is as accurate as the one for PSD as function of $D_{max}$. Moreover, Figure E8 shows that the function $\Phi_{2,3}(x)$ (Eq. 19, Eq. 20 and Eq. 24) is also valid to describe PSD as function of equivalent spherical diameter.

This appendices explores the consequences of using PSD as function of equivalent spherical diameter (as PSD are usually described in NWP) on the parameterization of ice hydrometeors size distribution in MCS developed in the main part of this study. On the four equations that describe this parameterization, only two equations need to be updated with new coefficients: Eq. (12) becomes Eq. (E2) and Eq. (18) becomes Eq. (E3). While Eq. (17) and Eq. (24) are applicable to both types of PSD whether PSD are as function of $D_{max}$ or as function of $D_{sp}$.

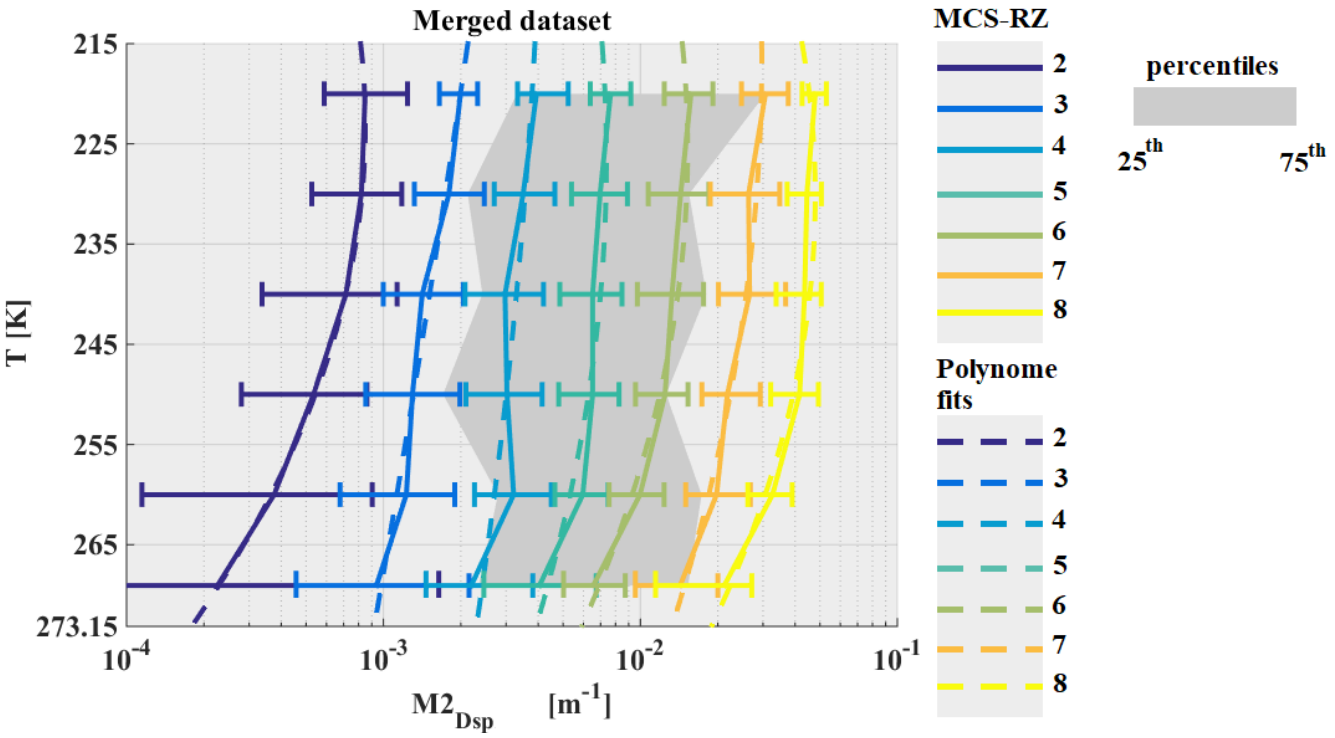

**Figure E 1: Same as Figure 5, but for $M_2$ per meter, where PSD are used as function of equivalent spherical diameter**

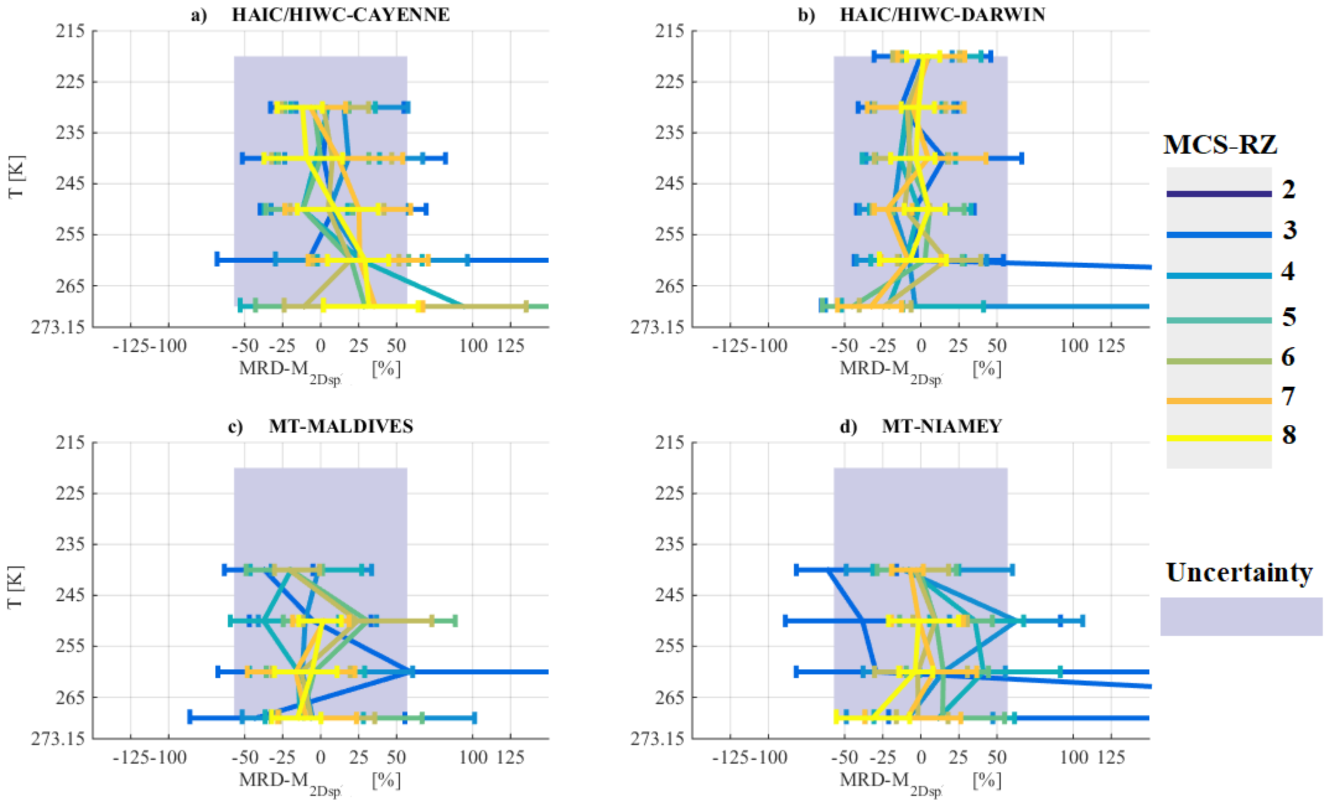

**Figure E 2: Same as Figure 6, but for MRD-$M_2$, where PSD are used as function of equivalent spherical diameter.**

5

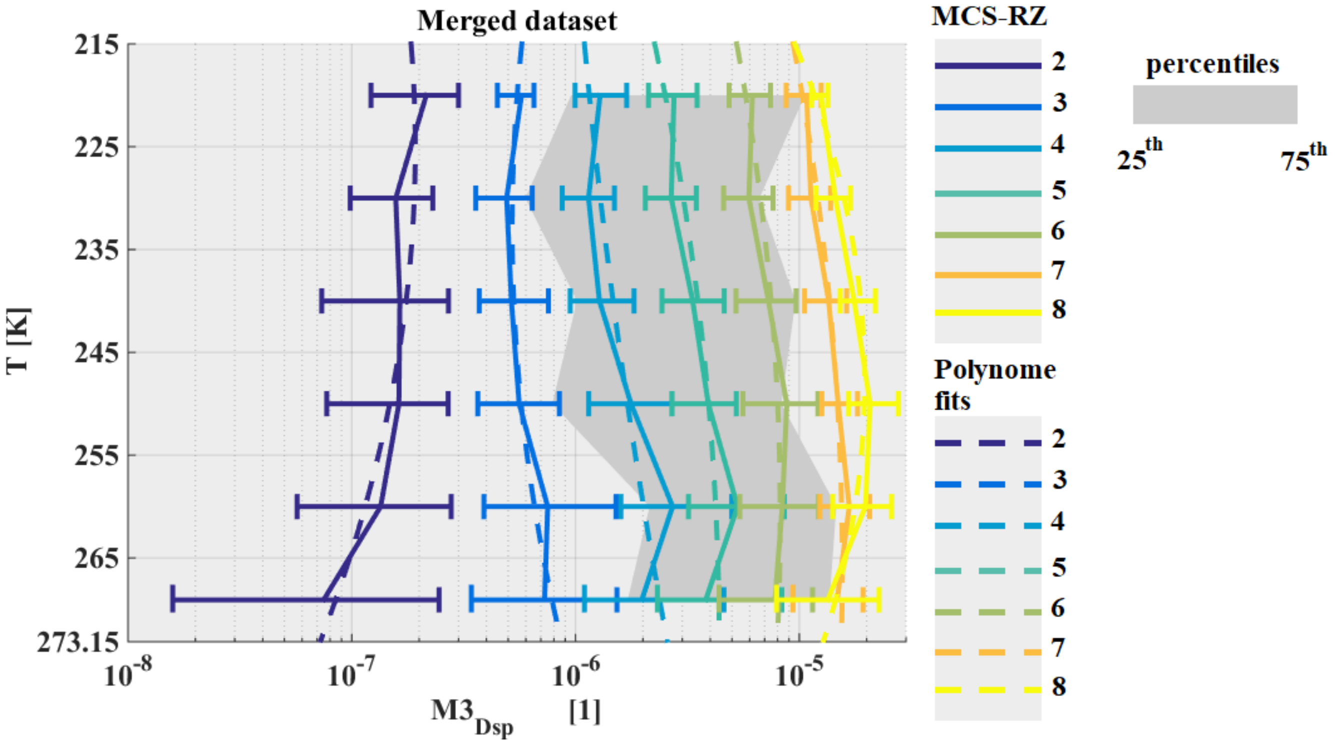

Figure E 3: Same as Figure 5, but for $M_3$ per meter, where PSD are used as function of equivalent spherical diameter.

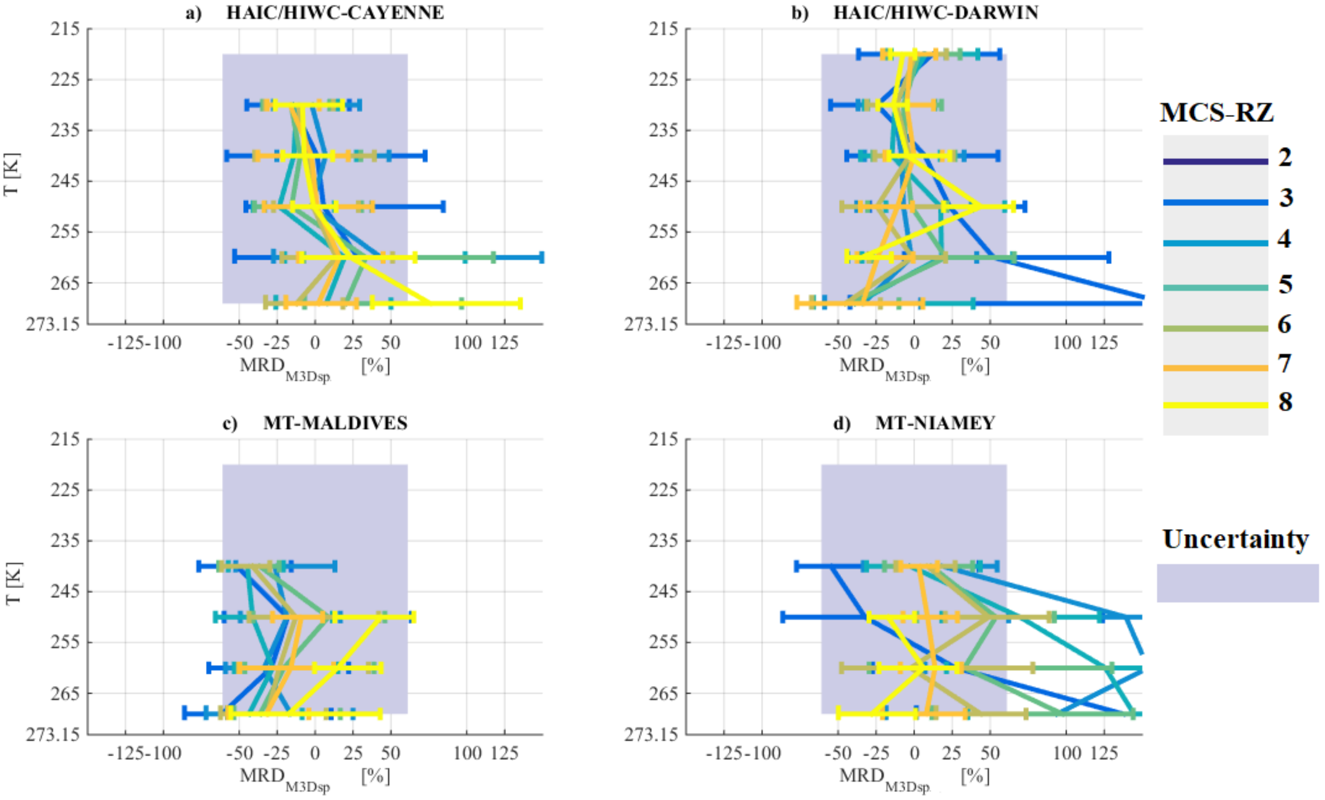

Figure E 4: Same as Figure 6, but for MRD-$M_3$, where PSD are used as function of equivalent spherical diameter.

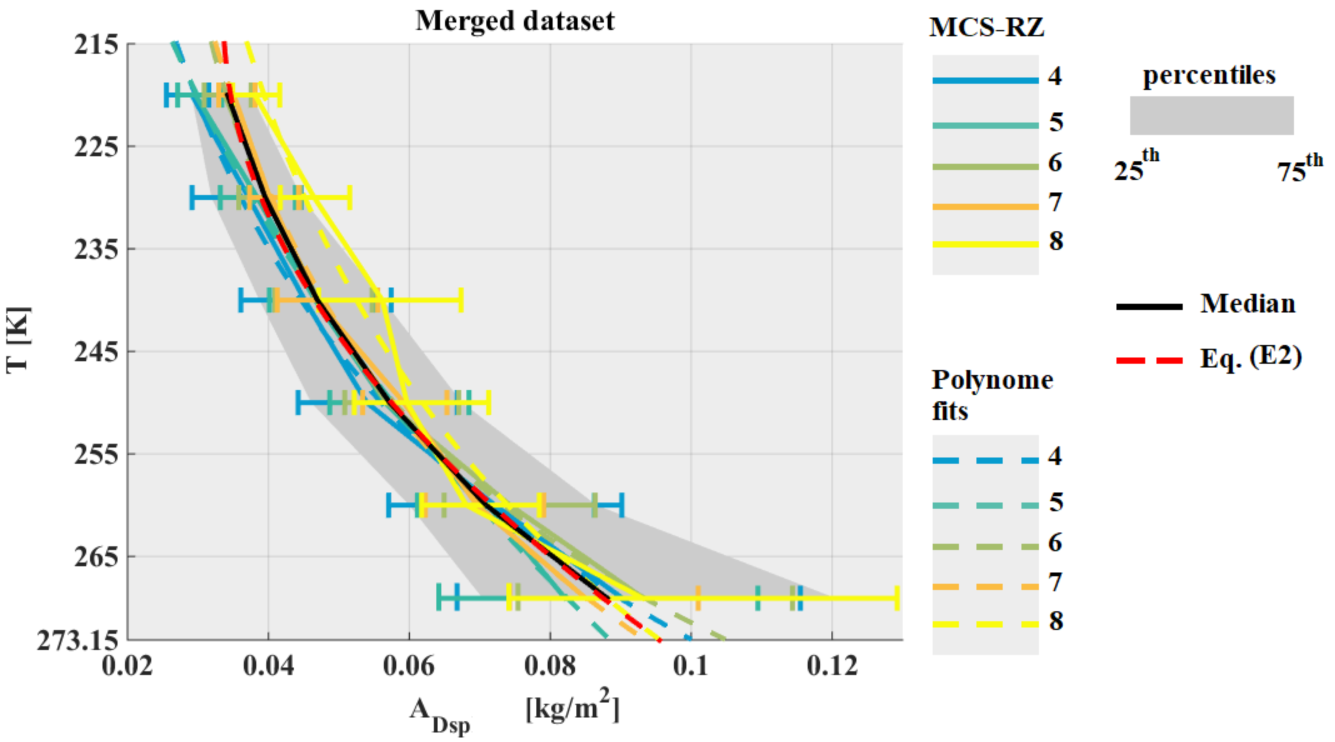

**Figure E 5: Same as Figure 5, but for the ratio A= IWC/$M_2$ in [kg m$^{-2}$], where PSD are used as function of equivalent spherical diameter.**

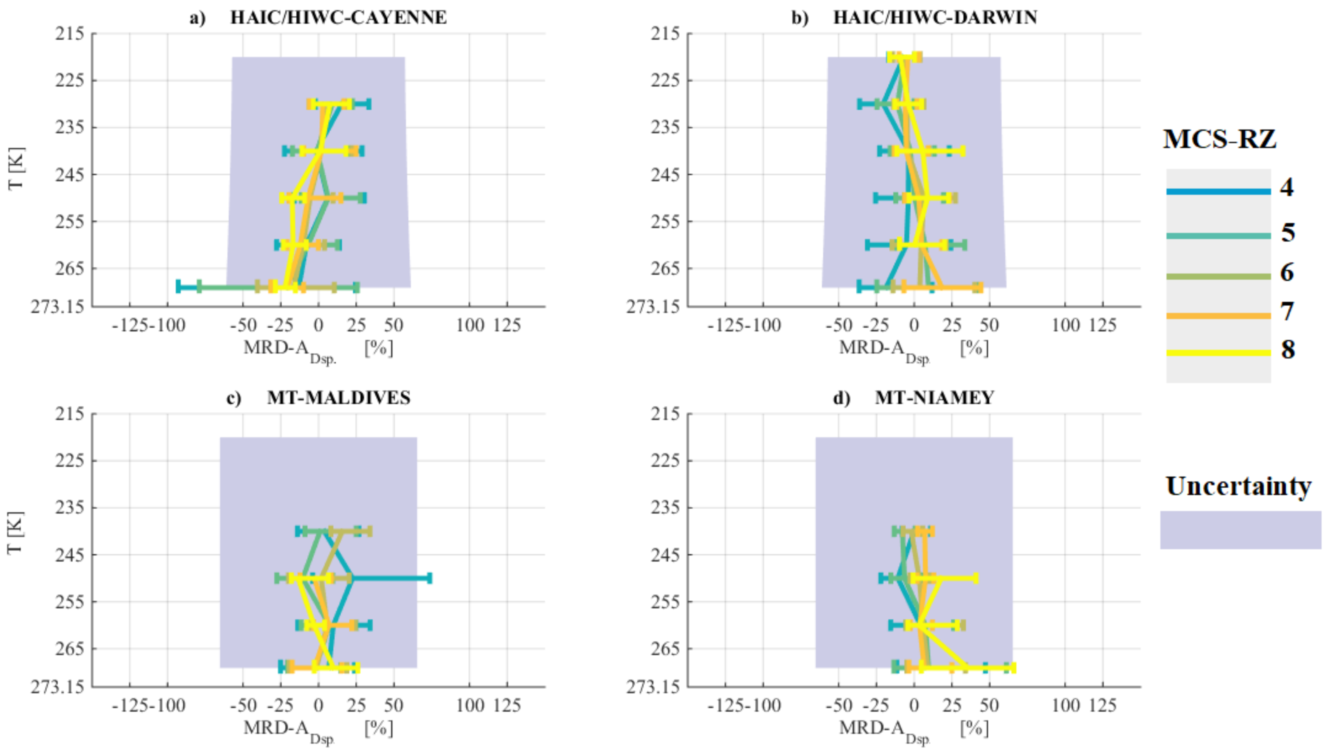

**Figure E 6: Same as Figure 6, but for the ratio MRD-A, where PSD are used as function of equivalent spherical diameter.**

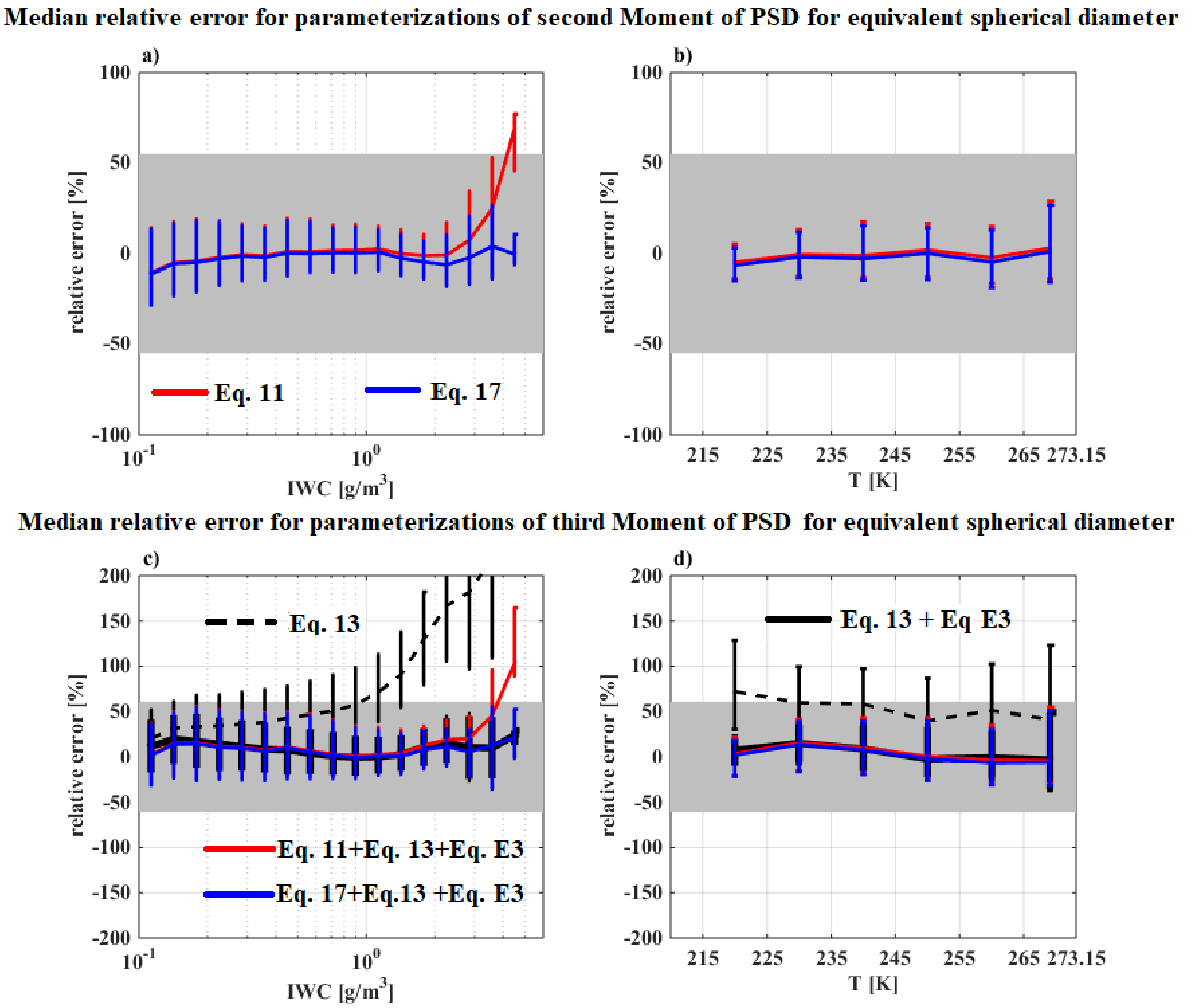

**Figure E 7: Relative error of parametrized $M_2$ and $M_3$ for merged dataset as a function of IWC in a) and c), and as a function of T in b) and d). Solid lines give median relative error and whiskers denote 25th and 75th percentiles of relative error. Grey bands shows measurement uncertainties for $M_2$ (55%; a) and b)) and $M_3$ (61%; c) and d)), respectively. For PSD as function of equivalent spherical diameter.**

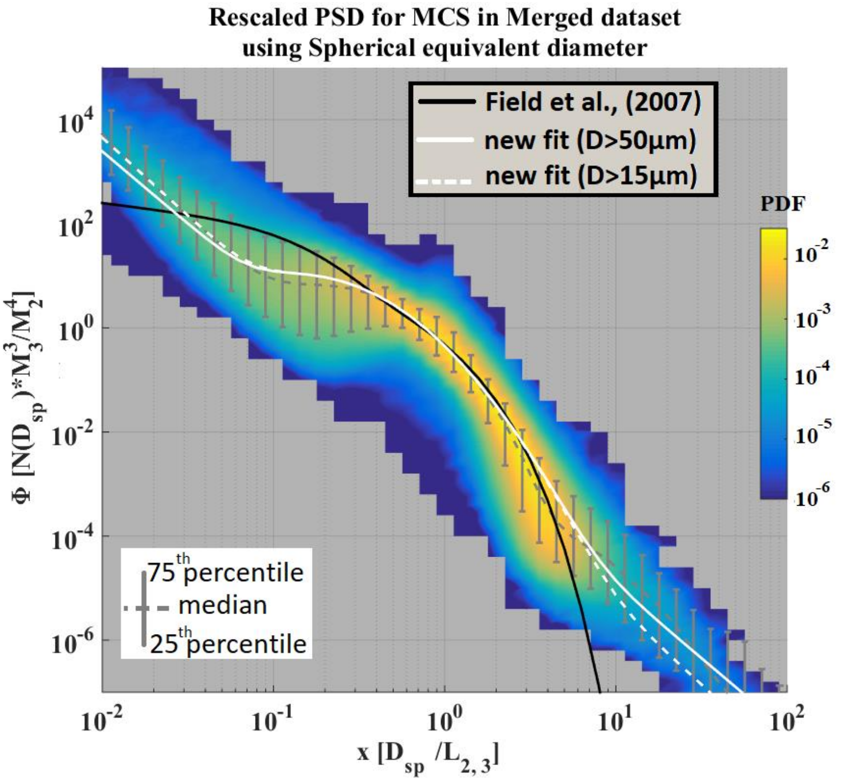

**Figure E 8: Probability distribution function of rescaled PSD ($\Phi_{2,3}$) on y axis as a function of hydrometeor characteristics size (x) on x axis, for the merged datasets. Black lines show fitted functions from Field et al., (2007), grey dotted lines show median rescaled PSD with error bar from 25th and 75th percentiles of rescaled PSD. Solid white line presents the new fitted function for the merged dataset for PSD beyond 55µm and dashed white line shows fitted function for PSD beyond 15µm (Eq. 24). When PSD are calculated as function of equivalent spherical diameter.**